

Metal Injection Moulding of Titanium-Niobium Alloys for Biomedical Applications

Von der Fakultät Maschinenbau, Elektrotechnik und
Wirtschaftsingenieurwesen der Brandenburgischen Technischen Universität
Cottbus-Senftenberg zur Erlangung des akademischen Grades eines Doktors
der Ingenieurwissenschaften genehmigte Dissertation

vorgelegt von

Dapeng Zhao

geboren am 03. Juni 1987 in Hebei, China

Vorsitzender: Prof. Dr. Bernd Viehweger

Gutachter: Prof. Dr. Florian Pyczak

Gutachter: Prof. Dr. Regine Willumeit

Tag der mündlichen Prüfung: 01.04.2014

Abstract

The main subject of this work was the investigation of sintering behavior, microstructure, mechanical properties and biocompatibility of metal injection moulded (MIM) Ti-Nb alloys for biomedical applications. Commercially pure titanium (CP-Ti) samples were also fabricated by MIM as a reference.

The sintering behavior of MIM Ti-Nb alloys was studied at first, in order to roughly determine the sintering parameters in the following investigations. Dilatometry was applied to investigate the linear shrinkage of MIM Ti-Nb samples from room temperature to 1500 °C at a heating rate of 3 °C/min under argon atmosphere. Various sintering parameters and Nb contents were used to investigate their influences on microstructure and mechanical properties of MIM Ti-Nb alloys by means of density measurements, optical microscopy (OM), X-ray diffraction (XRD), scanning electron microscopy (SEM) and mechanical testing. Transmission electron microscopy (TEM) and high energy X-ray diffraction (HEXRD) measurement were applied to investigate the nature and precipitation of the unexpected titanium carbide precipitates in MIM Ti-Nb alloys. Initial cell adhesion and cell proliferation assays of human umbilical cord perivascular cells (HUCPV) on MIM Ti-Nb alloys were performed for biocompatibility characterization.

The results of this work show that MIM Ti-Nb and MIM CP-Ti samples have been successfully fabricated and the as-sintered samples show good shape retention without distortion compared to the green sample. The sintering process of MIM Ti-Nb alloys consists of three main steps – Ti-diffusion step, Ti-Nb-diffusion step and Matrix-diffusion step. With increasing sintering temperatures and time, MIM Ti-Nb alloys exhibit lower porosity and higher Young's modulus. A higher Nb content in MIM Ti-Nb alloys leads to an increase of carbide area fraction and porosity. The three factors – Nb content, carbide area fraction and porosity – determine the mechanical properties of MIM Ti-Nb alloys. An increase of Nb content and amount of carbides as well as a lowered porosity lead to a higher tensile strength. A decrease of Young's modulus can be expected with higher Nb content and porosity. A high amount of titanium carbides can result in very poor ductility, but annealing and quenching process can significantly improve the elongation by dissolving the carbides. MIM Ti-Nb alloys exhibit good biocompatibility, indicating their potential for implant applications.

Zusammenfassung

Das Hauptthema dieser Arbeit war die Untersuchung von Sinterverhalten, Mikrostruktur, mechanischen Eigenschaften und Biokompatibilität von mittels Metallpulverspritzguss (MIM: Metal Injection Moulding) verarbeiteten Ti-Nb Legierungen für biomedizinische Anwendungen. Reintitan (CP-Ti) Proben wurden ebenfalls mittels MIM als Referenz hergestellt.

Zunächst wurde das Sinterverhalten der MIM Ti-Nb Legierungen untersucht, um die Sinterparameter für die folgenden Untersuchungen abzuschätzen. Dilatometrie wurde angewendet, um die lineare Schrumpfung von MIM Ti-Nb Proben beim Aufheizen von Raumtemperatur auf 1500 °C mit einer Rate von 3 °C/min unter Argon Atmosphäre zu untersuchen. Verschiedene Sinterparameter und Nb-Gehalte wurden verwendet, um deren Einflüsse auf die Mikrostruktur und die mechanischen Eigenschaften von MIM Ti-Nb Legierungen mit Hilfe von Dichtemessung, optischer Mikroskopie (OM), Röntgenbeugung (XRD), Rasterelektronenmikroskopie (REM) und mechanischer Prüfung zu bestimmen. Transmissionselektronenmikroskopie (TEM) und Hochenergie-Röntgenbeugung (HEXRD) wurden angewendet, um Art und Ausscheidungsprozess der unerwarteten Titankarbide in MIM Ti-Nb Legierungen zu untersuchen. Zur Charakterisierung der Biokompatibilität wurden Tests bezüglich anfänglicher Zelladhäsion und Zellproliferation von perivaskulären Zellen der menschlichen Nabelschnur (HUCPV) auf der Oberfläche von MIM Ti-Nb Legierungen durchgeführt.

Die Ergebnisse dieser Arbeit zeigen, dass MIM Ti-Nb und MIM CP-Ti Proben erfolgreich hergestellt werden können. Die gesinterten Proben zeigten eine gute Formbeständigkeit ohne Verzerrung gegenüber des Grünteils. Der Sintervorgang der MIM Ti-Nb Legierungen besteht aus drei Hauptschritten – Ti-Diffusionsschritt, Ti-Nb-Diffusionsschritt und Matrix-Diffusionsschritt. Mit zunehmender Sinter Temperatur und Zeit zeigen MIM Ti-Nb Legierungen eine abnehmende Porosität und eine Erhöhung des E-Moduls. Ein höherer Nb Gehalt führt zu einer Erhöhung der Flächenanteile von Karbiden und Poren. Die drei Faktoren – Nb Gehalt, Karbid-Flächenanteil und Porosität – kontrollieren die mechanischen Eigenschaften von MIM Ti-Nb Legierungen. Eine Erhöhung des Nb-Gehaltes und der Menge der Karbide sowie eine geringere Porosität führen zu einer höheren Zugfestigkeit. Eine zusätzliche Verringerung des E-Moduls findet mit höherem Nb-Gehalt und höherer Porosität statt. Eine große Menge an Titankarbiden führt zu einer niedrigen Duktilität, jedoch kann die Dehnung durch Glühen und Abschrecken zur Auflösung der Karbide deutlich verbessert werden. MIM Ti-Nb Legierungen weisen eine gute Biokompatibilität auf und zeigen dadurch ihr großes Potenzial für Implantat Anwendungen.

Eidesstattliche Erklärung

Hiermit erkläre ich an Eides statt, dass ich die vorliegende Dissertation ohne fremde Hilfe und ohne Benutzung anderer als der angegebenen Quellen und Hilfsmittel angefertigt und die den benutzten Quellen wörtlich oder inhaltlich entnommenen Stellen als solche kenntlich gemacht habe. Zudem wurde die Arbeit nicht in der gegenwärtigen oder einer ähnlichen Form an einer anderen Fakultät eingereicht. Auch habe ich weder in der Vergangenheit Promotionsanträge gestellt, noch ist dies aktuell an einer anderen Fakultät der Fall.

Die derzeit geltende Promotionsordnung der Fakultät für Maschinenbau, Elektrotechnik und Wirtschaftsingenieurwesen der Brandenburgischen Technischen Universität Cottbus ist mir bekannt.

Geesthacht, den 02.01.2014

1. Introduction.....	1
1.1 Scope of the work	3
2. State of the art	4
2.1 Ti and Ti alloys for biomedical applications.....	4
2.1.1 Ti-Nb alloys for biomedical applications.....	6
2.1.2 Biocompatibility of Ti alloys for biomedical applications	8
2.2 Metal injection moulding process.....	8
2.2.1 Powders.....	10
2.2.2 Binder and feedstock.....	11
2.2.3 Injection moulding and debinding	12
2.2.4 Sintering.....	13
2.2.6 Hot isostatic pressing	16
2.3 MIM Ti and Ti alloys for biomedical applications	17
2.4 Titanium carbide in Ti and Ti alloys	19
3. Experimental procedures	20
3.1 Materials	20
3.2 MIM process	20
3.2.1 Nb content.....	22
3.2.2 Sintering parameters	23
3.3 Hot isostatic pressing	25
3.4 Annealing and water quenching.....	26
3.5 Characterization of the samples	26
3.5.1 Dilatometry	26
3.5.2 Impurity levels, microstructural features and relative density.....	27
3.5.3 X-ray diffraction	28
3.5.4 Tensile test.....	29
3.5.5 In situ high energy X-ray diffraction measurements	29
3.5.6 Young’s modulus characterization	31
3.5.7 Surface topography and roughness characterization.....	32

3.5.8 Biocompatibility characterization.....	33
4. Results.....	36
4.1 Impurity levels	36
4.2 The pre-sintered samples and dilatometry results.....	37
4.2.1 XRD	38
4.2.2 Optical microscopy and SEM	38
4.2.3 Dilatometry	40
4.3 The as-sintered samples	42
4.3.1 Porosity	42
4.3.2 XRD	43
4.3.3 Optical microscopy and SEM	44
4.3.4 Young’s modulus.....	48
4.3.5 Tensile properties	48
4.4 The as-HIPed samples.....	52
4.4.1 XRD	52
4.4.2 Optical microscopy	53
4.4.3 Tensile properties and RUS measurements.....	53
4.5 TiC _x precipitates.....	56
4.5.1 Carbide area fractions	56
4.5.2 TEM and SAED analyses	57
4.5.3 In situ HEXRD analyses	59
4.6 The as-quenched samples	63
4.6.1 XRD	63
4.6.2 Optical microscopy and SEM	64
4.6.3 Tensile properties	66
4.7 Cell biology assessments	67
4.7.1 Surface characterization.....	67
4.7.2 Initial cell adhesion.....	69
4.7.3 Proliferation assays	73

5. Discussion.....	75
5.1 The sintering and homogenization behavior of MIM Ti-Nb alloys.....	75
5.2 The influence of sintering parameters on porosity and Young’s modulus of MIM CP-Ti and Ti-Nb alloys.....	80
5.2.1 The influence of sintering parameters on porosity.....	80
5.2.2 The influence of porosity on elastic modulus of MIM CP-Ti and binary Ti-Nb alloys	81
5.3 The influence of Nb content on microstructure and mechanical properties of MIM CP-Ti and Ti-Nb alloys.....	84
5.3.1 The influence on α / β phase fraction.....	84
5.3.2 The influence on porosity	85
5.3.3 The influence on mechanical properties and fractography	86
5.4 The TiC_x precipitation in MIM Ti-Nb alloys	91
5.5 Biocompatibility of MIM Ti-Nb alloy	102
6. Conclusions.....	104
Appendix 1 – Abbreviations of various samples	107
Appendix 2 – Properties of different samples.....	108
References.....	109
Acknowledgements.....	122

1. Introduction

Nowadays, it has been estimated that about 90 % of the population over the age of 40 suffers from different kinds of degenerative diseases on the bones [1]. The application of artificial biomaterial is one of the best solutions for these problems. At present, about 70-80 % of implants are made of metallic biomaterials [2]. Amongst the metallic materials available for implant applications, Titanium (Ti) and its alloys are the most attractive choice for the medical applications because of their unique combination of properties including high strength, low density (high specific strength), good corrosion resistance and outstanding biocompatibility [3]. The first attempt to use Ti as implant material dates back to late 1930s [2]. Until recently, the mainstream approach taken for the introduction of implant materials are commercially pure Ti (CP-Ti) and Ti-6Al-4V alloy with extra-low interstitials (Ti-6Al-4V ELI), which have been used for the manufacture of surgical implants for over 40 years [4]. However, there are a few drawbacks of the Ti-based biomaterials that have been widely used, i.e., CP-Ti and Ti-6Al-4V.

Firstly, the applications of CP-Ti and Ti-6Al-4V alloys are limited by the traditional processing techniques. Biomaterials are used in different parts of the human body as artificial valves in the heart, stents in blood vessels, replacement implants in knees, hips, shoulders and ears. All of the above-mentioned artificial parts should exhibit complex shapes with subtle details to conform to the human tissues. However, the traditional producing processes are limited in manufacturing Ti and Ti alloys as implant material due to the rather high costs of the raw material, the complex fabrication process, and the associated geometry design constraints. Metal injection moulding (MIM) could be an attractive choice to overcome these problems [5]. One reason is that MIM can reduce costs due to its net-shape fabrication advantages, if high numbers of components are produced. On the other hand, MIM offers unique design flexibility that is not readily achievable with other fabrication processes [6-13].

During recent years, there have been several attempts regarding the MIM of Ti and Ti alloys. The standards ASTM F2989-13 and ASTM F2885-11 have been developed for MIM CP-Ti [14] and MIM Ti-6Al-4V [15], respectively. CP-Ti components which had biocompatible properties were also produced via MIM process. The tensile strength, elongation and oxygen levels of the components met the requirements for ASTM Grade 2 Ti [16]. Ti-6Al-7Nb alloy fabricated by MIM exhibited properties similar to those of the wrought materials [17]. Sidambe et al. [18] produced Ti-6Al-4V specimens by MIM using a water soluble binder. Ferri et al. [19] and Obasi et al. [20] investigated the influence of microstructures and processing parameters on mechanical properties of a Ti-6Al-4V alloy processed by MIM.

Secondly, Ti-6Al-4V and CP-Ti are reported to have either cytotoxicity or biomechanical incompatibility as implant materials [3, 21]. The vanadium and aluminium in the Ti-6Al-4V alloy are found to be basically cytotoxic to cells and might be associated with long-term health problems, including neurological disorder and poor osseointegration [22]. In addition, long-term studies have revealed that the CP-Ti (pure α) and Ti-6Al-4V ($\alpha+\beta$) alloys prevent the sufficient load being transferred to adjacent bone, because they have much higher Young's modulus (100~120 GPa) than bones (4~30 GPa) [23, 24]. Such a biomechanical incompatibility is called "stress shielding effect". It usually results in bone resorption and eventual implant loosening [25]. As for Ti alloys, the β -phase exhibits about 60~80 GPa of Young's modulus, which is much lower than that of the α -phase (100~120 GPa) [26]. Therefore, the β or near- β Ti alloys, such as titanium-molybdenum (Ti-Mo) alloys [27], titanium-tantalum (Ti-Ta) alloys [28] and titanium-hafnium (Ti-Hf) alloys [29] have been developed recently. Niobium (Nb) is not only an important β -phase stabilizer, but also highly biocompatible [30]. Some studies have reported that Ti-Nb alloys can exhibit a elastic modulus of about 50~60 GPa, which is much closer to that of human bones when compared to other binary Ti-based alloys [31-33]. They have thus attracted increasing attention as promising

implant materials.

As a consequence, an investigation about Ti alloys without cytotoxic element additions fabricated by MIM is required. In this framework the identification of the microstructure, mechanical properties and biocompatibility of the MIM parts is necessary.

1.1 Scope of the work

In the present work, the microstructure, mechanical behavior and biocompatibility of CP-Ti and a series of Ti-Nb alloys fabricated by MIM are investigated, where the MIM CP-Ti samples were produced as a reference. Experiments were performed to determine the sintering behavior of the MIM Ti-Nb alloys, as well as the effect of sintering parameters and Nb content on the microstructure and mechanical behavior of the MIM CP-Ti and Ti-Nb alloys. Additionally, the titanium carbide precipitation in the MIM Ti-Nb alloys has been observed for the first time. In order to identify the formation mechanism and the nature of the titanium carbides, detailed investigations about the composition, microstructure and relevant phase diagrams were performed. The biocompatibility of MIM CP-Ti and Ti-Nb alloys was also investigated by *in vitro* cell adhesion and proliferation tests.

2. State of the art

2.1 Ti and Ti alloys for biomedical applications

The first paper about Ti written by a 30-year-old English clergyman and mineralogist named William Gregor dates back to 1791. In 1795, a German chemist called Martin Heinrich Klaproth borrowed the name from “the Titans”, the first sons of the earth, and named the element as “Titanium” [34]. The industrial production of titanium started from the 1940s [34]. Alloy development progressed rapidly from about 1950s stimulated by the recognition of the strengthening effect of aluminum (Al) additions. A major breakthrough was the appearance of the Ti-6Al-4V, which is still the most important Ti alloy at present [35].

Ti is a transition metal (atomic number 22) with an atomic structure $1s^2, 2s^2, 2p^6, 3s^2, 3p^6, 3d^2, 4s^2$. The $3d^2$ and $4s^2$ electrons are highly reactive, so Ti can rapidly form a tenacious oxide layer on the surface under air. The remaining electrons are relatively stable and tightly bound. Such a property contributes to the metal’s excellent biocompatibility. In its elemental form, Ti exists as a hexagonal close-packed (HCP) structure (α -phase) up to the β transus temperature (882 °C), and transforms to a body centered cubic (BCC) structure (β -phase) above this temperature [35]. Therefore, Ti alloys are classified as either α , near- α , $\alpha+\beta$, near- β or β depending on their room temperature phase constitution. The β transus temperature of Ti can be influenced by the addition of alloying elements. The elements, which are termed as α -stabilizers (such as O, N and Al), can stabilize the α -phase. The addition of these alloying elements results in a higher β transus temperature. In contrast, the alloying elements which stabilize β -phase, including Nb, Ta, V and Mo, are known as β -stabilizers, because the addition of them into Ti leads to a decrease of the β transus temperature. Zr and Sn do not have significant influence on the stability of either α -phase or β -phase, but can form solid solutions in Ti. Thus, such elements are called neutral

elements. α and near- α Ti alloys exhibit excellent corrosion resistance, but they show much higher stiffness than the human bones. $\alpha+\beta$ Ti alloys show high strength due to the presence of both α -phase or β -phase. While, near- β or β Ti alloys exhibit a combination of relatively high strength and low Young's modulus [36], moreover, β Ti alloys properties can be adopted / tailored by proper heat treatment.

The implant materials must fulfill the following requirements: corrosion resistance, biocompatibility, osseointegration, Young's modulus similar to that of bones, high strength, good processability and availability [35]. Compared with various groups of candidates for biomedical applications, such as stainless steels, commercially pure Nb (CP-Nb), commercially pure Ta (CP-Ta) and CoCr-based alloys, Ti and its alloys show a better combination of all the properties above. Zitter and Plenk [37] pointed out that the most corrosion resistant materials are Ti and its alloys, CP-Nb, and CP-Ta, followed by wrought CoCr-based alloys and stainless steel under normal conditions in human body fluid. Ti and its alloys can form protective nonconductive oxide layers on the surface, so the permanent Ti-based implants are highly biocompatible in human body [38]. Ti and Ti alloys usually have a Young's modulus of 80~120 GPa, which is among all permanent metallic biomaterials the closest to that of bone (10~30 GPa) [39]. In tensile and fatigue strength, Ti and its alloys are equal or even higher than others [40]. At present, all current processing methods are possible to fabricate Ti and its alloys as biomedical materials. Concerning the costs of the products, Ti and its alloys belong to the same group as stainless steel, whereas, CoCr-based alloys, CP-Nb and CP-Ta are more expensive [36]. Owing to these properties, the use of Ti and its alloys in the biomedical field has become a well established area.

Three types of Ti-based materials, i.e., CP-Ti, $\alpha+\beta$ alloys and β alloys, have been used for biomedical parts. The first successful clinical application of CP-Ti as plates and screws for the fixation of bone fractures goes back to 1951 [41]. In the early 1970s, the standard alloy Ti-6Al-4V was introduced into implant application, owing to its

high strength. In the middle of 1970s, the extra-low interstitial (ELI) quality was introduced to the Ti-6Al-4V alloy. From the 1980s, a number of Ti alloys as biomaterials have been developed. Table 2.1-1 presents some of these Ti alloys developed for implant applications with different standards [4, 14, 42, 43].

Table 2.1-1 Ti alloys for biomedical applications

Composition	Condition	Standard
Pure Ti (Grade 1, 2, 3, 4)	Wrought	ASTM F67 / ISO 5832-2
Ti-6Al-4V	Wrought	ISO 5832-3
Ti-6Al-4V ELI	Wrought	ASTM F136
Ti-6Al-4V ELI	Forged	ASTM F620
Ti-6Al-4V ELI	Metal injection moulded	ASTM F2885-11
CP-Ti	Metal injection moulded	ASTM F2989-13
Ti-6Al-7Nb	Wrought	ASTM F1295
Ti-5Al-2.5Fe	Wrought	ISO/DIS 5832-10

2.1.1 Ti-Nb alloys for biomedical applications

CP-Ti and Ti-6Al-4V are still used in most biomedical applications today. However, the mismatch in elastic modulus between the two materials (100~120 GPa) and the bone (4~30 GPa) prevent the stress transfer to adjacent bone. This usually leads to the “stress shielding effect”, i.e., death of the bone cells around the implant and thus to bone resorption and implant loosening [1, 23, 24]. For Ti alloys, the Young’s modulus of β -phase (60~80 GPa) is much lower than that of α -phase (100~120 GPa) [26, 42]. In addition, although some alloying elements such as V, Ni and Al are used to strengthen the Ti alloys, they can exhibit cytotoxicity to cells and cause long-term health problems [22, 44]. As a consequence, β or near- β Ti alloys without cytotoxic element additions have been developed to overcome the limitations [45-49].

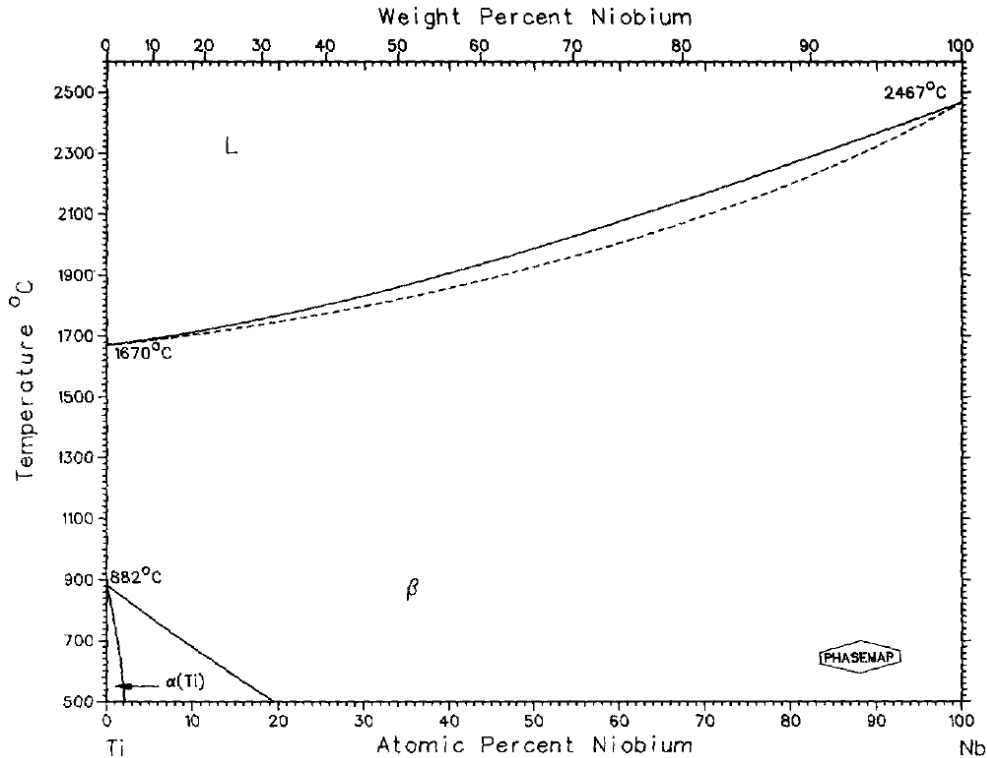


Fig. 2.1-1. The Ti-Nb phase diagram [50].

Nb has good biocompatibility and osteoconductivity [21]. The addition of Nb in Ti alloys also does not show toxic effect on the cells [51, 52]. Nb is not only highly biocompatible, but also acts as an important β -phase stabilizer in Ti alloys. Fig. 2.1-1 presents the Ti-Nb binary phase diagram [50]. A significant β -stabilizing effect can be observed. For instance, with 22 wt. % addition of Nb into Ti, the β transus temperature decreases from 882 °C to 721.5 °C. Thus, Nb is promising to decrease the Young's modulus of Ti alloys. It is reported that the Nb addition in Ti alloys is more efficient than other β -stabilizing elements in reducing the elastic modulus [31, 32]. Handa et al. [53] investigated the dependence of Young's modulus on Nb content in Ti-Nb alloys. A minimum of the Young's modulus has been found when the Nb content is around 16 wt.%. Besides the influence of Nb on Young's modulus of Ti alloys, a strength-improvement has also been observed with Nb addition [54]. Consequently, increasing attention has been paid to the Ti-Nb alloys as promising implant materials. For instance, a biomedical Ti-24Nb-4Zr-8Sn alloy has been developed [55]. It exhibits a tensile strength of around 660 MPa, Young's modulus of

53 GPa and over 10 % Elongation.

2.1.2 Biocompatibility of Ti alloys for biomedical applications

The biocompatibility of Ti and its alloys, e.g., CP-Ti and Ti-6Al-4V alloys, has been extensively investigated [56, 57]. *In vitro* tests are necessary before any *in vivo* implantation, to determine biocompatibility-related parameters, such as cell adhesion and cell proliferation on implant materials.

Cell adhesion experiments reveal the union of cells to the surface of implant materials in an early stage. The early adhesion of cells is essential for further cell proliferation and cell differentiation [58]. The chemical composition of the implant should be non-cytotoxic, otherwise the cells will die. For example, different cytotoxicity behaviors were observed in a series of Ti alloys with varying alloying elements [59]. The presence of Cu in Ti alloys caused cytotoxic effects, while, the Ti alloys with addition of the elements, such as Nb, Ta and Zr, showed good cell adhesion. Open porosity and interconnection dimensions are considered to be beneficial to cell ingrowth and bone osteointegration [60]. The pore sizes between 100 and 400 μm in porous implant materials were found to be necessary for blood and nutrient supply within the grafts [61]. Besides, material surfaces play an essential role in determining the cell recruitment, cell adhesion, cell proliferation and cell differentiation. For instance, improved adhesion and proliferation behaviors of human bone marrow stromal cells on Ti-6Al-4V samples with rougher surface were observed [62].

2.2 Metal injection moulding process

The attempts to use the shaping advantages of injection moulding in producing metal or ceramic parts date back to the 1920s. However, until 1979, major attention had not been given to the process, which is known as powder injection moulding (PIM) at

present. From the 1980s, PIM has been regarded as a leading net-shape technique. It successfully combines the advantages of the powder metallurgy technique with the injection moulding process. There are five key factors for the suitability of PIM for any application – high final properties, tight tolerances, materials flexibility, low production costs and shape complexity. As for the ceramics production, the process is termed “ceramic injection moulding” (CIM); if metals are used, the process is named as “metal injection moulding” (MIM) [6]. The MIM process requires four steps – formation of the feedstock, injection moulding, debinding process, and sintering. Initially, selected metal powders are mixed with binders to obtain the feedstock. The polymeric binders are used in shaping the powders and holding them in place until bonding during sintering process. The feedstock is then granulated and injection moulded into the desired shape. The heated binders impart viscous flow of the feedstock to aid forming, die filling, and uniformity of packing. Usually, one component of the binder is removed in the following chemical debinding process. The final step is thermal debinding and sintering in a single furnace run. Fig. 2.2-1 displays the principle of the MIM process performed at HZG.

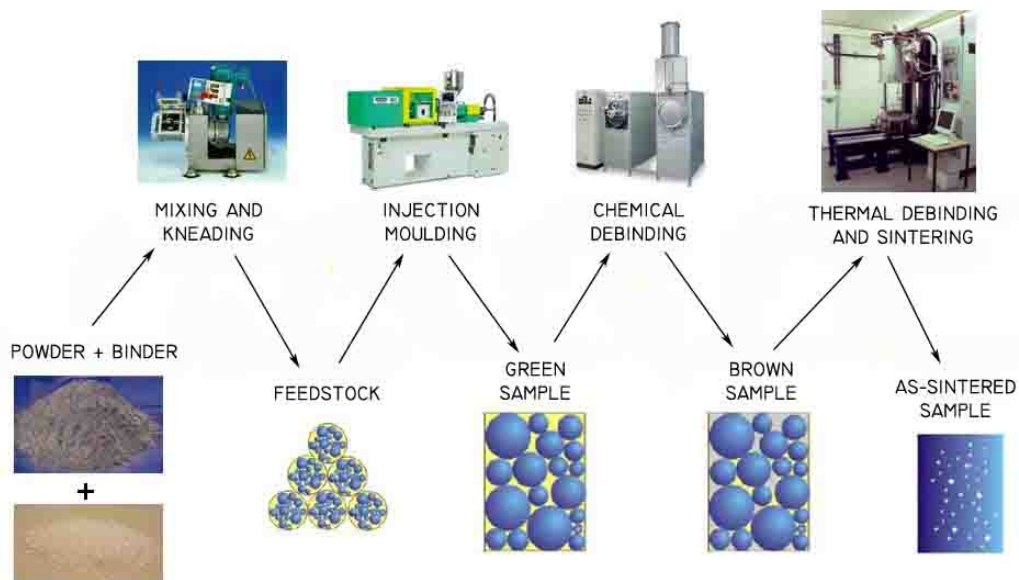


Fig. 2.2-1. A schematic diagram of the MIM processing steps at HZG.

Nowadays, a lot of metals and alloys such as copper, gold, bronze and tungsten are

available to be manufactured by the MIM process. MIM of ferrous materials including stainless steel and Fe-Ni steel is a well established fabrication technique. The consumption of stainless steel powders covers over 50% of the total amount of metal powders used for MIM. However, albeit the MIM process has been applied to Ti in various forms since the late 1980s, the production of Ti and Ti alloys by MIM is still a speciality in the field of MIM processing [8], owing to the principal difficulties in the MIM processing of Ti. For example, the availability of suitable Ti powders and feedstock is still poor. In addition, MIM parts manufacturers encounter further challenges connected to the high sensitivity of Ti to O, which can lead to highly brittle products [15]. Fortunately, there are two ASTM standards with acceptable chemical composition levels and minimal tensile property values for the most common Ti-6Al-4V alloy (ASTM F2885-11) and unalloyed Ti components for surgical implant applications (ASTM F2989-13).

2.2.1 Powders

In MIM technology, a particle is defined as the smallest unit of a powder that cannot be subdivided by simple mechanical methods. The particle morphology is very important for successfully controlling of the MIM process. There are three parameters in terms of particles that dominate the features of final products: particle size, particle shape and packing density [6]. Finer particles lead to faster sintering and smaller moulding defects, but slower debinding. The irregular particles show better shape retention of moulded parts during debinding than the spherical particles, but the densification is more difficult. A wide particle size distribution increases the packing density, but may lead to an inhomogeneous microstructure. Besides the geometry parameters, the chemical composition of particles is another important concern, because the particles with high impurity levels can be fatal to the mechanical properties, especially the ductility, of final products. Consequently, the characteristics of an idealized MIM powder can be summarized as follows [63]:

- a) tailored particle size distribution;
- b) small mean particle size for rapid sintering;
- c) dense but no agglomeration;
- d) low impurity levels, especially O, C and N contents;
- e) predominantly spherical or equiaxed particle shape.

Presently, there are three types of Ti-based powders which are widely used: sponge fines, hydride-dehydride (HDH) and gas-atomized (GA) powder [7]. The GA powders are more expensive than the other two kinds. However, the GA powders which are spherical exhibit better packing density and lower impurity levels compared to the sponge fine and HDH powders. As a consequence, a typical choice for Ti MIM powder is -325 mesh (below 45 μm) gas-atomized spherical powder with an oxygen level below 0.20 wt.% and a carbon level below 0.05 wt.% [10].

2.2.2 Binder and feedstock

The binder plays a dominant role in obtaining a desired shape with homogeneously packed powders and keeping the shape until the beginning of sintering. Moreover, the binder composition and debinding techniques are the focus of many patents for MIM processes [64]. The binder usually consists of three components: a backbone phase providing strength, a filler polymer which can be easily removed in the first step of debinding, and a surfactant, which is also a lubricant, to bridge between the binder and powder. The binders for MIM production are generally categorized into five types – thermoplastic compounds, thermosetting compounds, water-based systems, gelation systems and inorganics [65, 66].

The feedstock used in MIM is a pelletized mixture of metal powder and binder [67]. Accordingly, the attributes of the feedstock are dictated by powder characteristics, binder composition, powder/binder ratio, granulation or pelletization method, and

mixing technique. The key features of an ideal feedstock include a low viscosity, no voids or pores, a high elasticity and high mixture homogeneity [68].

2.2.3 Injection moulding and debinding

During the injection moulding step, temperature and pressure are varied to deliver the feedstock, which has been melted in the heated barrel of the moulding machine, to the mould. A reciprocating screw is usually applied to homogenize, pressurize and pack the feedstock. The molten feedstock can be injected into the mould with a forward thrust of the screw in the barrel. The rheological behavior of the molten feedstock plays a significant role in controlling the properties of the final products [69]. The viscosity of the feedstock is dependent on shear rate, temperature, powder loading, powder characteristics and the binder system [70]. In order to compensate for the higher viscosity associated with cooling, one of the effective options is heating the mould. Moreover, the filling times are usually minimized to prevent the feedstock cooling. After filling the mould, heat is extracted from the feedstock through the mould, leading to a hardened component. An injection moulding cycle is usually shorter than one minute. Fig. 2.2-2 presents a schematic graph of metal injection moulding operation. The moulding parameters are contingent on particle characteristics, feedstock viscosity, mould design, binder system, and machine operation conditions. In order to produce defect-free components, it is desirable to use uniform particle packing in a properly designed mould with well controlled temperature and injection velocity [71, 72].

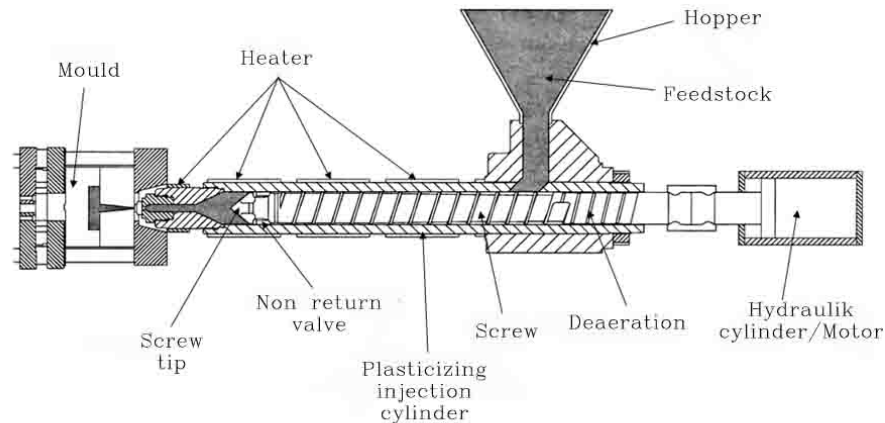


Fig. 2.2-2. A sketch of the basic metal injection moulding operation.

After injection moulding, the binder system should be removed by a series of physical and chemical processes, usually including chemical and thermal debinding, in order to keep the components from distortion, cracking and contamination [73]. The chemical debinding involves immersing the compact into a solvent so as to dissolve and remove at least one component of the binder system, leading to a structure with open pores. Such a highly porous structure is crucial for the subsequent thermal debinding. The key aim of thermal debinding is to remove the residual binder under protective atmosphere, e.g., argon. During thermal debinding, the evaporated or decomposed binder phases are transported to the surface through the open pores. In both chemical and thermal debinding processes, higher debinding rates are achievable at higher temperatures, however, potential defects, such as internal cracks, distortion and solvent trapping, tend to occur at high temperatures [74]. In order to fabricate components with good mechanical properties, such defects should be avoided or at least minimized by changing the debinding parameters.

2.2.4 Sintering

In MIM processing, sintering is a necessary thermal treatment after debinding to bond the particles into a coherent, solid mass [75]. On a micro scale, pores are eliminated during sintering. The cohesion takes place as necks between particles grow where

they are in contact. On a macro scale, the component shrinks to a smaller dimension. Typically, the sintering is the process where particles bond together at temperatures below the melting point.

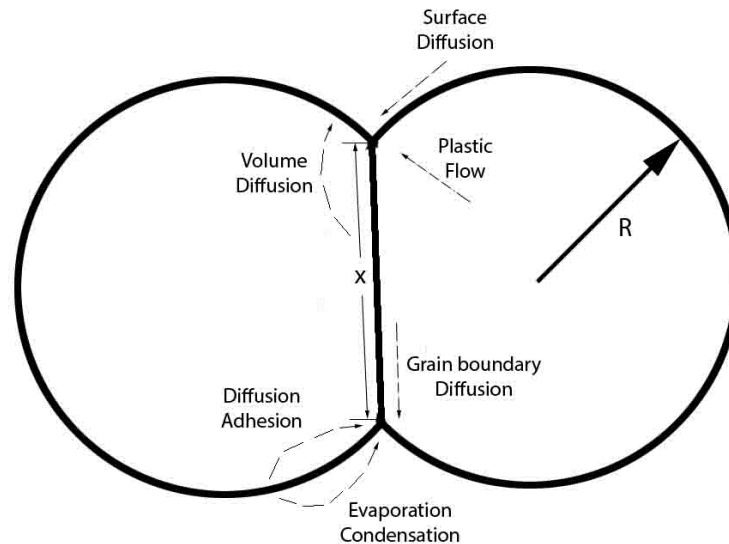


Fig. 2.2-3. The mass transport mechanisms around the neck region between two particles during sintering. X and R are the neck diameter and particle radius, respectively.

The basic mechanism of the sintering process has been studied to a large degree [76-80]. The driving force for the sintering process is a reduction in the system free energy, which is manifested by a decrease of surface curvatures and an elimination of surface area. Fig. 2.2-3 shows the mass flow paths around the neck between particles. During the shrinkage of pores between particles, mass flows along grain boundaries by grain boundary diffusion, along particle surfaces by surface diffusion, across pore spaces by evaporation condensation, and through the lattice interior by viscous flow or volume diffusion. As stated by German [6], in general, the mass transport during sintering can be divided in two categories for polycrystalline materials: surface transport and bulk transport. The surface transport mechanism consists of evaporation condensation, surface diffusion and diffusion adhesion. The surface transport mechanism contributes to surface smoothing, neck growth and pore rounding, but do not lead to densification since mass flow originates and terminates at the particle

surface. In contrast, the bulk transport mechanism controls the sintering shrinkage and the material densification. It includes lattice diffusion, grain boundary diffusion and plastic flow. The most useful densification process for MIM products is usually grain boundary diffusion [63]. Mass flows along grain boundaries between the near-perfect crystal regions and into the pores, so that mass is preserved but pore space is not. Since the densification of materials during sintering mainly depends on mass diffusion, the parameters which determine the diffusion process inevitably have significant influences on densification. According to Fick's law of diffusion, the quantity of mass flow N is proportional to diffusion time t and the absolute value of diffusion flux $|J|$. One of the most important factors influencing the diffusion flux J is the diffusion coefficient D , which is given as:

$$D = D_0 \exp\left(\frac{-Q}{kT}\right) \quad (2.2-1)$$

where D_0 is the pre-exponential frequency factor, Q is the activation energy, k is Boltzman's constant, and T is the absolute temperature. Consequently, both temperature and time play important roles in the densification during sintering.

Sintering is not a single mechanism process. It is usually composed of three stages [81, 82]:

- Initial stage: During this stage, the neck size ratio ($X / 2R$) is less than 0.3. The pore structure is open and fully interconnected, and the pore shape is not very smooth. The driving force for the initial sintering stage is the curvature gradient at the neck.
- Intermediate stage: The intermediate sintering stage is an important stage for densification, because the predominant improvement of compact properties occurs during this stage. The driving force is the interfacial energy, including both surface and grain boundary energy. The pores in this stage exhibit an interconnected, cylindrical structure. The porosity is normally in the range of 8 % to 30 %.

- Final stage: When the porosity decreases to approximate 8 %, the cylindrical structure of pores becomes unstable and collapse into isolated, spherical pores, indicating the beginning of the final stage. In this stage, the densification kinetics is very slow. Further shrinkage of samples is limited, due to the high vacancy diffusion energy through the lattice. In addition, a coarsened microstructure is usually observed in the final sintering stage. The grain boundary areas are high in energy, so the grain size increases rapidly at high temperature.

The production of MIM samples may be accomplished by conventional powder processing of pre-alloyed powders or by the processing of blended powders with different compositions. The latter method necessarily requires the insertion of a homogenization step in the processing sequence. Many works concerning the production of alloys from powder blends have been described in literature [83-85]. Brand and Schatt [86] and Levin et al. [87] investigated the homogenization during sintering in a system with unlimited and limited solubility of components, respectively. The homogenization of the binary powder mixtures can be classified as three groups – single-phase systems (e.g. Cu-Ni), two-phase systems (e.g. Cu-Fe) and three-phase systems (e.g. Mo-Ni), according to the phase diagrams [88]. The homogenization behavior of the W-5Re (wt.%) alloy produced by blending W and Re powders was investigated [89]. No apparent Kirkendall porosity was observed in this system. However, in the Ti-Fe alloys fabricated by blending elemental powders, the formation of Kirkendall type pores due to the unbalanced diffusion was observed [90, 91]. Accordingly, the diffusion coefficients of the powders probably have a significant influence on the homogenization process.

2.2.6 Hot isostatic pressing

By means of a sintering process, it is difficult to obtain components with full density. During the final sintering stage, grain size grows significantly. The elimination of

grain boundary regions, especially near pores, greatly inhibits further densification [82, 92-94]. Therefore, after sintering, special techniques to remove the remaining porosity by pressure-assisted densification techniques such as hot isostatic pressing (HIP) are sometimes applied, so as to improve the properties of the MIM samples. The HIP process is currently most widely used to densify the components with porosity less than 5 % after sintering. Meanwhile, even a complex shape of the components can be maintained during HIP [95]. There are three parameters which play significant roles in the HIP process. The temperature for the HIP process should be between 70 % and 85 % of the absolute melting temperature. If the temperature is below at about one half of the melting temperature, the HIP process is no longer effective to achieve full densification. The effective stress, i.e., the stress at the interparticle contacts, is the second important factor during the HIP process. Pores act as stress concentrators, so the effective stress is different from the external stress. A low strain rate provides for more plastic deformation of the components and thus is usually favorable to limit fracture [96, 97].

2.3 MIM Ti and Ti alloys for biomedical applications

MIM has grown significantly during the last decades owing to its capability to economically produce complex near-net-shaped components in many engineering alloy systems [98]. MIM has been particularly successfully applied in the biomaterial fields, such as producing forceps, blades and jaws [99]. At present, the utilization of Ti and Ti alloys as implant materials is limited because of the rather high raw material costs, the complex fabrication process, and associated geometry design constraints [84]. In order to overcome these problems, there have been several attempts to apply MIM in the fabrication of Ti and Ti alloys as biomaterials in recent years. However, many early attempts regarding MIM Ti and Ti alloys mainly suffer from the unavailability of suitable powder, inadequate atmosphere during sintering at elevated temperatures and less than optimum binders for Ti-based components [13]. Nowadays,

suitable powders, binder systems and sintering furnaces are available, so that some Ti and Ti alloys have been successfully fabricated by MIM process. For instance, the processing of CP-Ti Grade 4 has been well established and numerous medical parts are produced worldwide [100]. A water soluble binder system comprised of a major fraction of PEG, a minor fraction of PMMA and small amounts of stearic acid was introduced into the MIM Ti-6Al-4V fabrication [101]. The tensile strength, elongation and oxygen levels of the final products could meet the requirements for ISO 5832-3 titanium. The Ti-6Al-7Nb alloys were manufactured by MIM using three types of mixed powders, consisting of Ti, Nb and Ti-Al powders [17]. The mechanical properties of the Ti-6Al-7Nb alloys were similar to that of wrought materials. Ferri et al. [19] investigated the influence of surface quality and porosity on the fatigue behaviour of Ti-6Al-4V components processed by MIM. A higher sintering temperature and better surface quality was considered to be favorable. However, albeit the mechanical properties of MIM Ti and Ti alloys have been widely discussed, very few investigations focused on the biocompatibility.

A few parameters dominate the mechanical properties of MIM Ti and Ti alloys as biomaterials – porosity, interstitial content and microstructure [8]. Porosity leads to a reduced strength and elongation, so the MIM parameters should be carefully adjusted. The sintering parameters have a significant effect on final porosity, thus the identification of a suitable sintering temperature and time is one of the first concerns. Besides, HIP process is often a common means to attain full density. Attention has been paid on the impurity levels of the MIM Ti-based components [7, 102]. For instance, yield strength $\sigma_{0.2}$ of the as-sintered MIM Ti alloys varied with the fractional density ρ and oxygen equivalent O_{eq} as follows:

$$\sigma_{0.2} = (420 + 970O_{eq})\rho \quad (2.3-1)$$

where the oxygen equivalent O_{eq} is given as:

$$O_{eq} = (wt.\%O) + 2(wt.\%N) + 0.5(wt.\%C) \quad (2.3-2)$$

Ebel et al. [5] reported that in the MIM Ti-6Al-4V alloys, there is a critical O_{eq} value at around 0.45 wt.%, above which the ductility decreases dramatically. Besides porosity and interstitial levels, microstructure parameters as grain grain size and phase constitution after sintering are also important factors, because a coarse microstructure may lead to low strength, while high amounts of α -phase always result in high Young's modulus.

2.4 Titanium carbide in Ti and Ti alloys

Titanium carbide (TiC_x) is often introduced into the Ti-based matrix as it can improve strength [103], wear resistance [104] and act as oxygen getter [105]. In a Ti-25V-15Cr-2Al alloy with carbon addition, TiC_x particles were observed and caused a significant improvement of the mechanical properties [106]. Chen et al. [105] also reported that the yield strength of Ti-15V-3Al alloy increased by about 20 % when carbon contents increased from 0 to 0.2 wt.%. TiC_x reinforced Ti-6Al-4V components exhibited higher hardness, higher elastic modulus, higher tensile strength and better wear resistance than wrought Ti-6Al-4V alloys, but were much less ductile at room temperature [107]. In the Ti-Mo-C and Ti-V-C system, the volume fraction of the TiC_x precipitates was found to be the main factor for increasing strength at elevated temperatures [108]. However, the TiC_x particles can be detrimental to the ductility. Kim et al. [107] found that the TiC_x particles act as sites for crack initiation and paths for crack propagation in TiC_x reinforced Ti-6Al-4V.

3. Experimental procedures

3.1 Materials

The materials for MIM production used in this work are gas-atomized (GA) spherical Ti powder (Grade 1 ASTM) with particle diameter $< 45 \mu\text{m}$, supplied by TLS Technik GmbH, Germany, and Hydride/Dehydride (HDH) Nb powder with particle diameter $< 110 \mu\text{m}$, supplied by MHC Industrial Corporation, China. Fig. 3.1-1 shows the morphology of the Ti and Nb powders. The impurity levels including carbon, oxygen and nitrogen contents of the powders were determined using a conventional LECO melt extraction system. Table 3.1-1 shows the impurity levels of the powders.

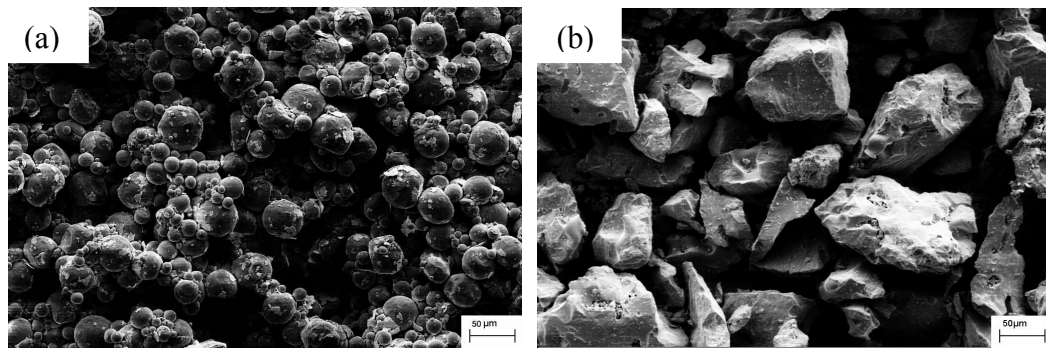


Fig. 3.1-1. Scanning electron micrograph of (a) GA Ti powder; (b) HDH Nb powder.

Table 3.1-1 Impurity levels of the powders (wt.%).

	O	C	N
Ti powder	0.0744	0.00469	0.0375
Nb powder	0.221	0.0152	0.0890

3.2 MIM process

All samples made from CP-Ti and Ti-Nb binary alloys were produced by a MIM process. The alloys were produced by blending elemental Ti powder and Nb powder. The powders were mixed with a polymer binder that consists of 5 wt.% stearic acid, 35 wt.% polyethylene vinyl acetate and 60 wt.% paraffin wax in a Z-blade mixer at

120 °C for 2 h under argon (Ar) atmosphere to form a batch of feedstock materials. In this study, all feedstock materials prepared had the same binder fraction of 31 vol.%.

After granulation, an Arburg 320S machine was used for the injection moulding of the feedstocks. The feedstocks were injection moulded as standard “dog bone” shape tensile specimens as shown in Fig. 3.2-1a, or rectangular-bar specimens as presented in Fig. 3.2-1b. The “dog bone” and rectangular-bar specimens were analyzed for the microstructure and mechanical behavior investigations.

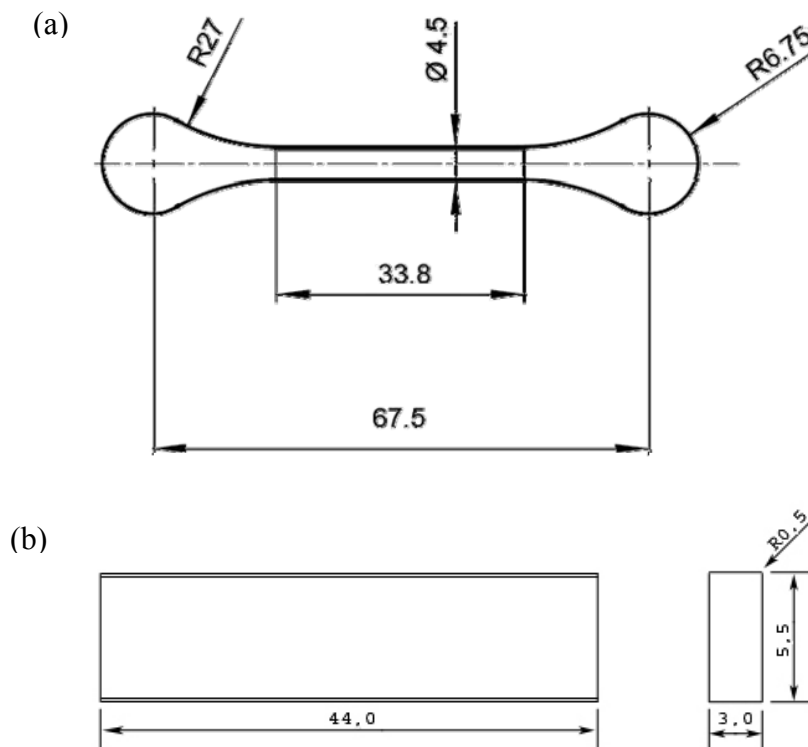


Fig. 3.2-1. Geometry of (a) “dog-bone” tensile specimen and (b) rectangular-bar specimen. Typical dimensions of the as-sintered part are measured in millimeters.

The samples for biocompatibility tests, i.e., the CP-Ti and Ti-22Nb (wt.%) samples with diameter of 10 mm, thickness of 2mm, were prepared using another injection moulding machine (MCP-INJECTION MOULDING 100KSA, supplied by HEK GmbH, Germany).

The green (after injection moulding) samples were subjected to solvent extraction by immersing them into hexane at 40 °C for 20 h in a LÖMI EBA 50 debinding device. Thermal debinding and the sintering of specimens were carried out in one cycle. Thermal debinding was under Ar flow (500 Pa), while, the sintering process was under vacuum (10^{-3} Pa). Sintering was conducted in a XERION XVAC 1600 furnace with tungsten heating elements and shield packs of molybdenum. The furnace cooling rate was controlled to be 10 °C/min.

Fig. 3.2-2 shows a green “dog-bone” sample and its as-sintered form. All the Ti-Nb alloys were made from elemental Ti powder and Nb powder. So it is more difficult to avoid distortion of the specimen shape compared to the use of pre-alloyed powder. However, the as-sintered sample showed good shape retention without distortion compared to the green sample.



Fig. 3.2-2. Injection moulded and as-sintered “dog-bone” tensile test specimens. Top: The green sample; Bottom: The as-sintered sample

3.2.1 Nb content

The selection of the compositions of samples was based on the research of Hanada et al. [53], in which the Young’s modulus of Ti-Nb alloys exhibits a minimum value when the Nb content is around 15~20 wt.%. Owing to the particular significance of Young’s modulus in Ti-based biomedical alloys, samples with four compositions –

CP-Ti, Ti-10Nb, Ti-16Nb and Ti-22Nb (all wt.%) – were fabricated by the MIM process described above in this work, where the CP-Ti samples were fabricated as a reference.

3.2.2 Sintering parameters

Various sintering parameters were used in this work, in order to investigate the sintering behavior of the MIM Ti-Nb alloys and the influence of sintering parameters on microstructure and mechanical properties of the MIM CP-Ti and Ti-Nb alloys.

Table 3.2-1 The sintering parameters used in various sintering cycles.

	Sintering temperature / °C	Sintering time / h	Abbreviations
	1500	4	1500/4
	1500	2	1500/2
Sintering processes	1400	4	1400/4
	1400	2	1400/2
	1300	4	1300/4
	1100	4	1100/4
	700	0.03	700/0.03

The sintering temperatures and times are presented in Table 3.2-1. The respective sintering cycles are plotted in Fig. 3.2-3. It is important to note that the thermal debinding cycle in each sintering process was always the same, and only sintering temperature and time were varied. In order to differentiate the samples sintered at different temperatures with different sintering time, the sintering parameters will always be referred to in the form “Sintering temperature/Sintering time”. The full list of samples as well as the respective processing parameters is shown in the “Appendix 1”. The sintering temperatures from 1300 °C to 1500 °C were selected according to previous investigations on Ti and Ti alloys [16, 19, 98, 101, 109-112].

EXPERIMENTAL PROCEDURES

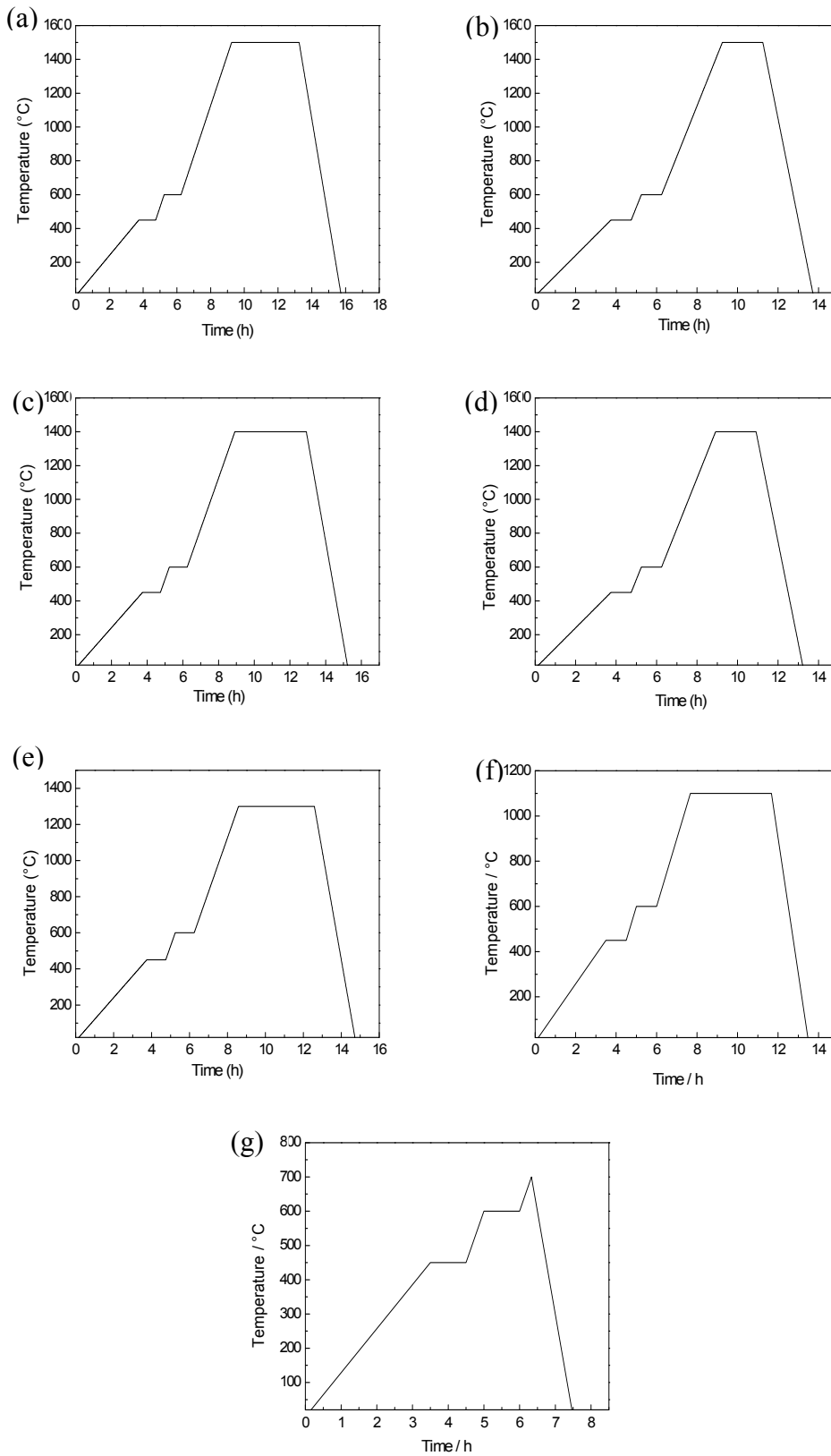


Fig. 3.2-3. Different sintering cycles.

(a) 1500/4; (b) 1500/2; (c) 1400/4; (d) 1400/2; (e) 1300/4; (f) 1100/4; (g) 700/0.03.

It is important to note that the sintering processes – 700/0.03 and 1100/4 – were only conducted on the MIM Ti-16Nb samples, for the sake of the investigation of the initial and intermediate sintering stage of MIM Ti-Nb alloys. Ti-16Nb (700/0.03) was heated up to 700 °C and held for 2 min, in order to obtain a relatively stable structure after the thermal debinding. 1100 °C is below the sintering temperatures of most Ti and Ti alloys, thus, a microstructure representing the situation at the intermediate sintering temperature could be expected in the Ti-16Nb (1100/4) sample. Therefore, the Ti-16Nb (700/0.03) and Ti-16Nb (1100/4) samples are classified as the pre-sintered Ti-16Nb alloys, and will be discussed individually in the following sections. In the following sections, when discussing “the as-sintered CP-Ti and Ti-Nb samples”, it means all the MIM CP-Ti and Ti-Nb samples sintered at 1300 °C, 1400 °C and 1500 °C.

Regarding the samples for biocompatibility tests, the sintering temperature was 1500 °C, and the sintering time was 4 h as shown in Fig. 3.2-3a. In order to differentiate these CP-Ti and Ti-22Nb samples from the ones for microstructure and mechanical properties analyses, they were named as CP-Ti (MIM-BIO) and Ti-22Nb (MIM-BIO), respectively.

3.3 Hot isostatic pressing

In order to obtain specimens produced by MIM process with no remaining pores, a HIP process was applied to densify components from CP-Ti (1500/4), Ti-10Nb (1500/4), Ti-16Nb (1500/4) and Ti-22Nb (1500/4) alloys. The HIP process was carried out in a shared titanium cycle running at Bodycote HIP N. V., Belgium. The HIP process cycle is presented in Fig. 3.3-1. In the following sections, the samples fabricated by MIM and exposed to the HIP process will be referred to as CP-Ti (HIP), Ti-10Nb (HIP), Ti-16Nb (HIP) and Ti-22Nb (HIP).

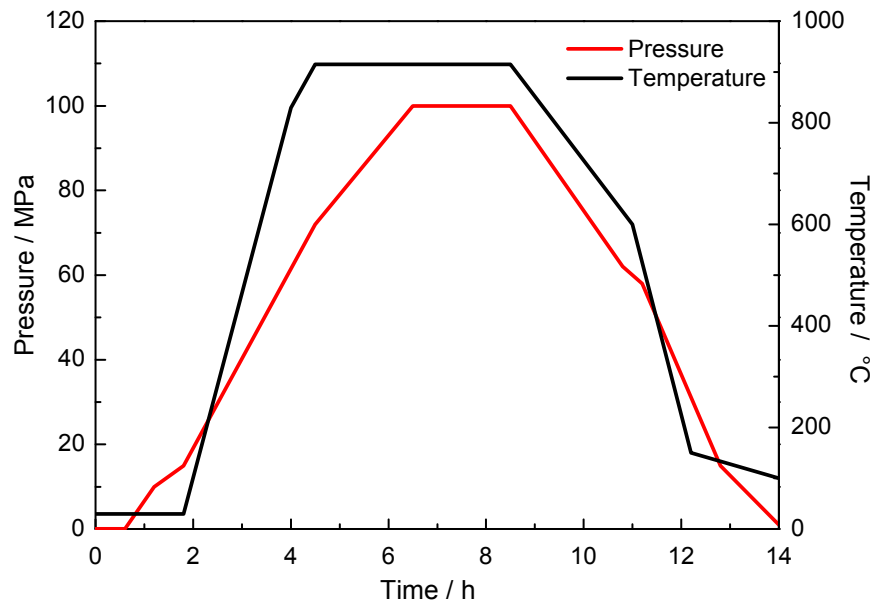


Fig. 3.3-1. HIP cycle process

3.4 Annealing and water quenching

Selected Ti-22Nb (1500/4) and Ti-22Nb (HIP) samples were encapsulated in sealed quartz tubes under vacuum (10^{-1} Pa). The parameters of the anneal process were determined by the calculated pseudo-binary phase diagram Ti-22Nb-C shown in Fig. 5.4-1, section 5.4.1. The anneal treatment was carried out at 641 °C (± 3 °C) for 120 h, followed by water quenching to room temperature with the quartz capsules broken open in water.

3.5 Characterization of the samples

3.5.1 Dilatometry

The sintering behaviour of the MIM Ti-16Nb alloy was investigated by dilatometry, where the MIM CP-Ti was also measured for comparison. The MIM samples made from CP-Ti and Ti-16Nb were chemically and thermally debound followed by pre-sintering at 700 °C for 1 h. The diameter of the samples was approximately 5

mm with a length of 10 mm. The dilatometer used was a vertical configuration dilatometer fabricated by LINSEIS (L70/2171). A heating rate of 3 °C/min and an isothermal holding at 1500 °C for two hours were used. The heating and cooling processes of the dilatometry experiments were conducted under Ar atmosphere. In the next sections, the two samples for dilatometry are named as CP-Ti (DIL) and Ti-16Nb (DIL), respectively.

3.5.2 Impurity levels, microstructural features and relative density

The impurity levels including carbon, oxygen and nitrogen concentrations of the specimens were determined using a conventional LECO melt extraction system. The CS-444 equipment was used to measure the carbon level. The TC-436AR was applied to analyse oxygen and nitrogen contents. At least three samples were examined for each configuration. Therefore, the impurity level values given here are averaged from these three samples.

Optical microscopy (Olympus PMG3), scanning electron microscopy (SEM) (Zeiss-DSM962 and Zeiss Ultra 55), energy-dispersive spectroscopy (EDS) (EDAX at LEO 1530) in the SEM and transmission electron microscopy (TEM) (FEI Tecnai F20, operated at 200 kV) were used for microstructural examination and compositional analysis. Samples for optical microscopy and SEM were mechanically polished with SiO₂ pastes, cleaned in successive ultrasonic baths of ethanol, and then dried. TEM samples were prepared using a precision ion polishing system (PIPS) at -50 °C. The grain size was determined using an imaging analysis system (Olympus Soft Image Solution, analysis pro) by the application of a linear intercept technique according to ASTM E112-96 as shown in Fig. 3.5-1.

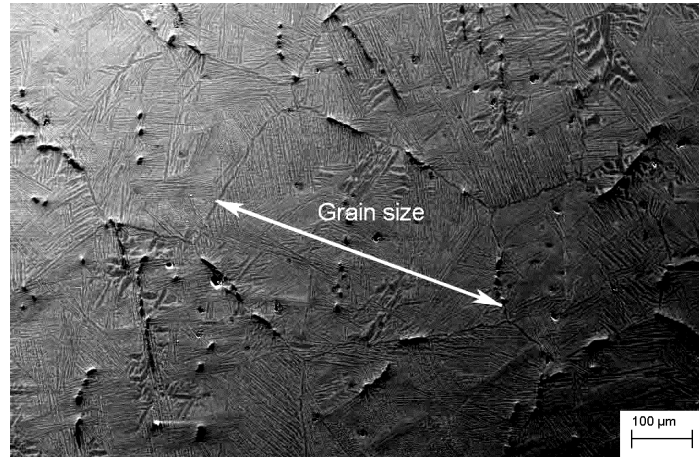


Fig. 3.5-1. Typical microstructure of MIM Ti-Nb alloys showing the grains.

The relative density of the as-sintered samples were determined by the immersion method (Archimedes's principle) outlined in ASTM B311. In order to determine the bulk density without pores, specimens exposed to an additional HIP process following the MIM production were measured as described in Section 3.3. The porosity P of the as-sintered samples could be calculated by using:

$$P = \left(1 - \frac{\rho_S}{\rho_H}\right) \times 100\% \quad (3.5-1)$$

where ρ_S is apparent density of the as-sintered samples and ρ_H is the apparent bulk density of the as-HIPed samples with the same composition.

3.5.3 X-ray diffraction

Constituent phases of the samples were characterized by X-ray diffraction (XRD), which was conducted on a Siemens D5000 diffractometer at 40 kV and 40 mA at room temperature. The wavelength of the X-rays is fixed to the wavelength of the copper wire inside used to generate the X-rays (1.5418 nm) and thus the diffractogram is in 2 dimensions (theta and intensity). Fig. 3.5-2 shows the XRD machine during operation. The database – PDF2002 of the International Centre for Diffraction Data (ICDD) was used for phase characterization.

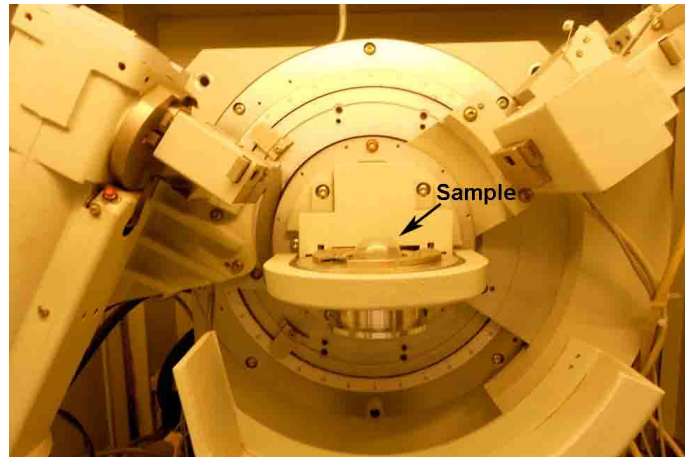


Fig. 3.5-2. The XRD machine in operation.

3.5.4 Tensile test

Fig. 3.2-1a shows the geometry of samples used for the tensile experiments. All samples were directly used in the tensile tests without any preparation. Tensile tests were performed on a servohydraulic test machine (RM-100, Schenk-Trebel, United States) modernized with a Zwick DUPS electronic testing system, and equipped with a 100 kN load cell using a strain rate of $1.2 \times 10^{-5} \text{ s}^{-1}$ to measure tensile strength, elongation and Young's modulus. The elongation was measured by a laser noncontact extensometer (WS-160, Fiedler Optoelectronik GmbH, Germany). At least three samples of each configuration were tested.

3.5.5 In situ high energy X-ray diffraction measurements

The in situ high energy X-ray diffraction (HEXRD) measurement were carried out at the High Energy Materials Science (HEMS) beamline of the Helmholtz-Zentrum Geesthacht at the Deutsches Elektronen-Synchrotron (DESY) in Hamburg, Germany. A specimen with a length of 10 mm for HEXRD was cut from the middle cylindrical part of a Ti-22Nb (1500/4) “dog-bone” sample. In order to penetrate the specimen, high energy X-rays with a photon energy of 100 keV, corresponding to a wavelength of $\lambda=0.124 \text{ \AA}$, with a beam cross-section of $0.5 \text{ mm} \times 0.5 \text{ mm}$. The resulting Debye-Scherrer diffraction rings were recorded on a PerkinElmer flat panel detector

with 2048×2048 pixels, pixel size of $200 \mu\text{m} \times 200 \mu\text{m}$ and exposure time of 0.5 s. Conventional diffraction patterns were achieved by an azimuthal integration of the Debye-Scherrer rings.

A dilatometer DIL 805A/D (Bähr-Thermoanalyse GmbH) that is especially modified for working at the beamline was used for heating and cooling (see Fig. 3.5-3). The sample was inductively heated under argon atmosphere during the measurement. Cooling was achieved by heat transfer through the Al_2O_3 rods, which hold the specimen, and the surrounding argon atmosphere under reduced induction powers. The temperature was controlled by a thermocouple directly spot-welded onto the specimen. In order to prevent oxidation of the sample surface, the experiments were performed under Ar atmosphere.

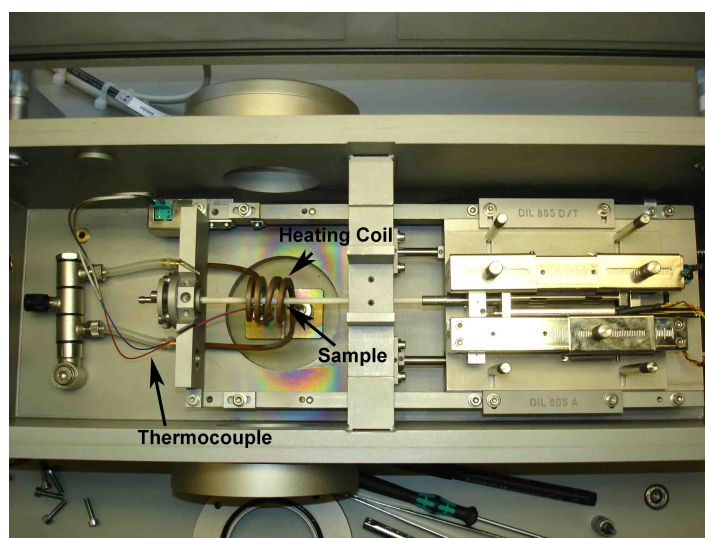


Fig. 3.5-3. The dilatometer used in the in situ HEXRD experiment.

During the heating and cooling cycle as represented in Fig. 3.5-4, diffraction patterns were recorded every 2 s. The 15 points – Point *A* to Point *O* – are indicated reflecting different time during the whole cycle.

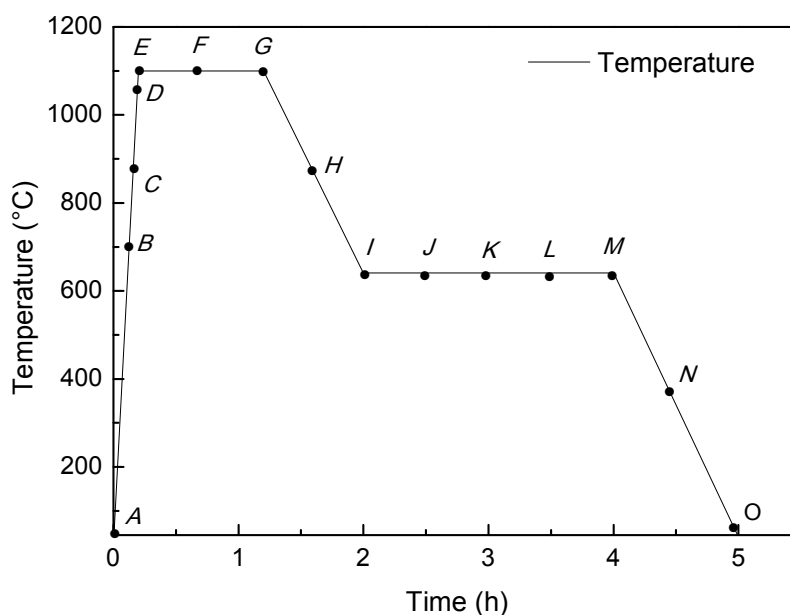


Fig. 3.5-4. The heating and cooling cycle used for the in situ HEXRD experiment. The 15 points indicated – Point *A* to Point *O* – reflect different times during the whole cycle.

3.5.6 Young's modulus characterization

The Young's modulus of “dog-bone” specimens was determined by calculating the slope of the stress-strain curve during elastic deformation in tensile tests. Furthermore, resonant ultrasound spectroscopy (RUS) technique was applied to measure the Young's modulus of rectangular-bar samples.

RUS method was employed because of the non-destructive nature of the measurement, simple operating procedures and simple specimen geometries. The RUS tests were performed using an IMCE resonant frequency damping analyzer (RFDA professional). A schematic diagram of the apparatus is shown in Fig. 3.5-5. In order to prevent any influence on the vibration by the supports, the rectangular-bar specimen was supported by two thin wires located at the fundamental nodes of the test specimen – a distance of $0.224 \times l$ from each end, where l is the length of the specimen. An

automatic impulser was applied to excite a mechanical vibration in the specimen by striking lightly at the center of the specimen. A non-contacting microphone placed above the specimen was used to detect the vibration. The RFDA was used to obtain frequency spectra and identify between 6 and 10 overtones for each specimen. The calculation of Young's modulus was performed according to ASTM E 1259.

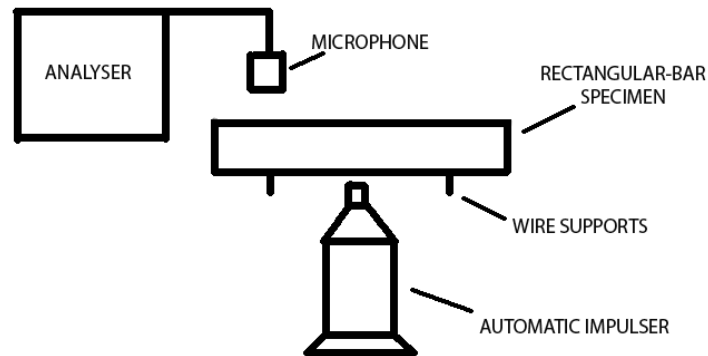


Fig. 3.5-5. Diagram of the RFDA professional test apparatus.

3.5.7 Surface topography and roughness characterization

The surface properties of implant materials are widely known to influence the local tissue response [113]. Therefore, extensive attention has been paid to the surface characterization. The confocal laser scanning microscope (CLSM) is a new microscopy technology used to observe morphology images without damaging the samples. It has many advantages, including simple sample preparation and a mode of operation that does not require vacuum conditions [114]. Thus in the present work, a non-contact measurement using a CLSM (VK-9700, Keyence, Japan) was employed to evaluate the surface roughness and obtain a 3-D surface topography of the BIO-samples. For each configuration, the surface roughness was calculated by VK Analyzer software (Keyence, Japan) according to the standard – JIS B 0601:2001 (ISO 4287:1997).

3.5.8 Biocompatibility characterization

Besides the CP-Ti (MIM-BIO) and Ti-22Nb (MIM-BIO) samples produced by MIM processes, Ti-22Nb samples fabricated by argon arc-melting in the furnace – Arc Melter AM, 2414000 (Edmund Bühler GmbH, Germany) were selected as reference in biological experiments. A Ti sponge with purity of 99.9 % (Timet Germany GmbH, Germany) and Nb pieces (Alfa Aesar, United States) were used to fabricate these specimens. Afterwards, the arc-melted Ti-22Nb samples were annealed at 1500 °C for 4 h, followed by cutting into disks with diameter of 10 mm, thickness of 2 mm. They were named as Ti-22Nb (AM-BIO). The surfaces of all Ti-22Nb (AM-BIO) samples were polished with SiO₂ pastes (0.05 µm; Gerd Sommer, Germany), cleaned in successive ultrasonic baths of ethanol (Merck KGaA, Germany), and then dried under normal atmosphere at room temperature. In order to differentiate the CP-Ti (MIM-BIO), Ti-22Nb (MIM-BIO) and Ti-22Nb (AM-BIO) samples from the ones for microstructure and mechanical properties characterization, they are termed the BIO-samples in the following.

All biological tests were performed with human umbilical cord perivascular cells (HUCPV), because HUCPV cells are excellent models to determine the biocompatibility of implant materials [115]. HUCPV isolations were approved by the local ethical committee and derived from Wharton's jelly of the umbilical cord were isolated by a modified isolation protocol from Sarugaser et al. [116]. The cords were cut into pieces of around 5 cm. The vessels from the cord pieces were isolated and tied together at the ends with sutures, resulting in a vessel loop. They were placed in T-175 cell culture flasks (Greiner Bio-One GmbH, Frickenhausen, Germany) and cultured for 10 days without changing medium, which consisted of α -MEM (Invitrogen Corporation, Karlsruhe, Germany) with 10 % fetal bovine serum (FBS; Calbiochem, Germany) for mesenchymal stem cells (Stem Cell Technologies, Vancouver, Canada). After observable outgrowth from the loops, the medium was

changed every 2 days. At about 60 % confluency the cells were harvested with a cell scraper and subcultivated in a density of 1,000 cells cm⁻². In the present experiments, cells of the third to fifth passage were used. The HUCPV cells were cultivated at 37 °C under 5 % CO₂ and 95 % humidity controlled atmosphere.

Initial cell adhesion and cell proliferation of HUCPV on the CP-Ti (MIM-BIO), Ti-22Nb (MIM-BIO) and Ti-22Nb (AM-BIO) samples were investigated. 50,000 HUCPV cells in 50 µL medium were seeded on each type of samples ($n = 4$; experiment was repeated 3 times) in 12-well plates (pre-coated with 1 % agarose; Carl Roth GmbH, Karlsruhe, Germany – to avoid unwanted adhesion artifact) and left to adhere for 30 min. Thereafter the samples were incubated in 3 mL medium for the remaining time (i.e., 10, 25, and 40 min). After the complete incubation time (i.e., 40, 55, and 70 min), the samples were transferred into new wells with Phosphate Buffered Saline (PBS). The cells were detached from the samples with 0.05% trypsin – EDTA (Merck, Germany), followed by counting cells using the cell counter system – CASY Model TT. A qualitative analysis was performed using SEM (AURIGA, Modular CrossBeam workstation, Carl Zeiss NTS GmbH, Germany) to observe cell morphology after the initial adhesion. After the incubation for 40, 55 and 70 min, the samples were fixed in 2.5 % glutaraldehyde solution (Fluka, United States), and stained with 1% Osmium Tetroxide (Fluka, United States). Afterwards, the specimens were dehydrated through a 2-propanol series, critical point dried by a critical point dryer (Leica EM CPD300, Leica Mikrosysteme GmbH, Vienna, Austria). Finally, the specimens were then viewed and photographed with the SEM.

For cell proliferation assays the methodology remains the same as the initial adhesion experiments, but the cultures were maintained for 3 or 5 days, followed by 3-(4,5-dimethylthiazol-2-yl)-2,5-diphenyl tetrazolium bromide (MTT; Sigma-Aldrich Chemie GmbH, Munich, Germany) tests. 150 µL (1:10) MTT solution (5 mg·mL⁻¹ MTT in PBS) was added to the cell supernatant in each well. After an incubation for 4

h in the incubator, the cells were lysed and the purple formazan crystals solubilized by adding 1.5 mL solubilization solution (10 % sodium dodecyl sulphate in 0.01 M HCl; Sigma-Aldrich Chemie GmbH, Munich, Germany) and overnight incubation at 37 °C under 5 % CO₂ and 95 % humidity controlled atmosphere. In order to photometrically quantify the solubilized formazan product, an enzyme-linked immunosorbent assay (ELISA) reader (Tecan Sunrise, TECAN Deutschland GmbH, Crailsheim, Germany) was applied at 570 nm with a reference wavelength of 655 nm.

Statistics were performed using the SigmaStat package (Systat software GmbH, Erkrath, Germany). Standard analysis comparing more than two treatments was done by using the one-way ANOVA (analysis of variance). Depending on the data distribution either a one-way ANOVA or an ANOVA on ranks was performed. Post-hoc tests were Holm-Sidak or Dunn's versus the control group, respectively. Statistical values are indicated at the relevant experiments.

4. Results

4.1 Impurity levels

Due to the influence of the impurity elements O, C and N on strength and ductility discussed in Section 2.3, the pre-sintered samples, as-sintered samples, as-HIPed samples and as-quenched samples described in the following sections were analyzed with respect to their content of these elements. Fig. 4.1-1 shows the dependence of impurity levels on the composition of all these samples. The deviation in these impurity levels from the average values was not significant, and all the compositions showed comparable values. In terms of oxygen and carbon contents, the values were in the range for CP-Ti Grade 2 according to ASTM F67. Since no data about O_{eq} of MIM Ti-Nb alloys are available from previous investigations, the results regarding MIM Ti-6Al-4V [112] are used for comparison. The oxygen equivalents of all these samples were in the range of 0.33~0.41 wt.%. They are lower than the critical value above which the ductility decreases dramatically [112]. These results indicate that the impurity levels might not be a significant concern when comparing the mechanical properties of the samples in the present investigation.

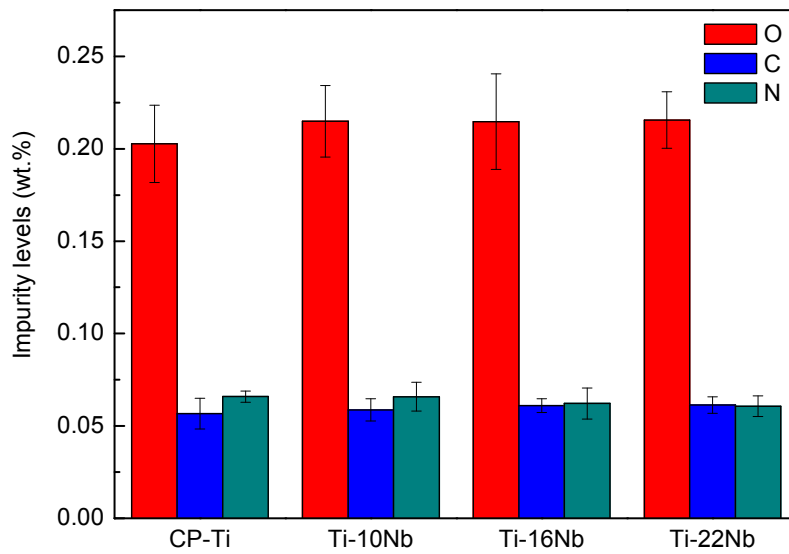


Fig. 4.1-1. Impurity levels of the pre-sintered, as-sintered, as-HIPed and as-quenched samples of the four compositions.

4.2 The pre-sintered samples and dilatometry results

Before conducting experiments on MIM Ti-Nb alloys, the sintering behavior of MIM Ti-Nb alloys was studied at first, so that the sintering parameters in the following investigations can be roughly determined. The MIM Ti-16Nb samples were selected to investigate the microstructure evolution and phase transition during the sintering process.

4.2.1 XRD

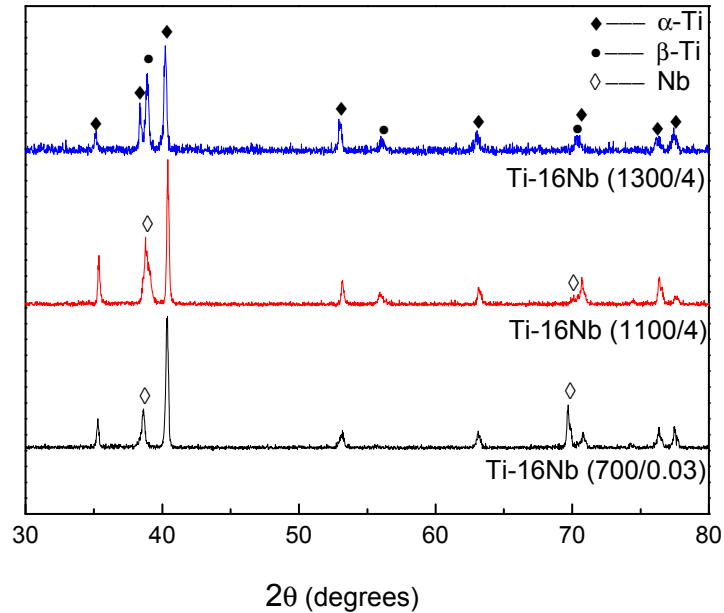


Fig. 4.2-1. XRD results for the Ti-16Nb (700/0.03), Ti-16Nb (1100/4) and Ti-16Nb (1300/4) samples.

The XRD spectra of the Ti-16Nb (700/0.03) and Ti-16Nb (1100/4) samples are displayed in Fig. 4.2-1. The Ti-16Nb (1300/4), which consists of both α -phase and β -phase, is also plotted for comparison. Ti-16Nb (700/0.03) was composed of α -Ti and Nb phase, whereas a trace amount of β -Ti was also found in the Ti-16Nb (1100/4) sample. The fraction of β -Ti showed an increase from Ti-16Nb (700/0.03) to Ti-16Nb (1300/4).

4.2.2 Optical microscopy and SEM

Fig. 4.2-2 presents the optical micrographs of the Ti-16Nb (700/0.03) and Ti-16Nb (1100/4) samples. The Ti-16Nb (700/0.03) sample showed a bimodal microstructure, consisting of spherical small particles ($<45\ \mu\text{m}$) and irregular large particles ($<110\ \mu\text{m}$), which exhibited similar sizes as GA Ti powder and HDH Nb powder particles, respectively. The microstructure of the Ti-16Nb (1100/4) sample was composed of

irregular large particles ($<110\ \mu\text{m}$) and a porous matrix. The porosity of the Ti-16Nb (1100/4) sample was measured as 11.0 %. It is important to note that no precipitates were observed in both samples.

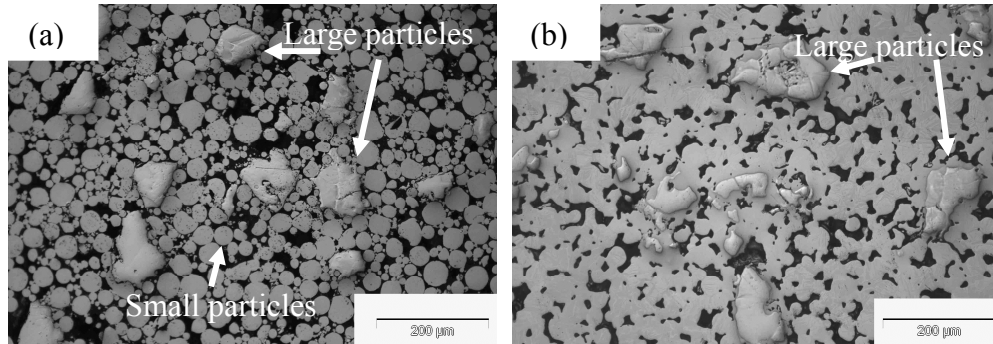


Fig. 4.2-2. Optical microscopy of (a) Ti-16Nb (700/0.03); (b) Ti-16Nb (1100/4).

Fig. 4.2-3 presents the back-scattered electron (BSE) SEM micrograph of the Ti-16Nb (1100/4) and that of the Ti-16Nb (1300/4) sample, which is displayed for comparison. In Fig. 4.2-3a, the irregular Nb particles (white spots) characterized by EDS as shown in Fig. 4.2-3b and the matrix composed of Ti particles (darker regions) were both visible. The neck growth between Ti particles was notable. Albeit some distinct residual pores (e.g. Point *A* in Fig. 4.2-3a) were found between the Ti and Nb particles, interdiffusion between the two kinds of particles was also observed as shown in Point *B* and Point *C* in Fig. 4.2-3a. Pores were also found in Nb particles near the interdiffusion areas (e.g. Point *D* in Fig. 4.2-3a). In contrast, as presented in Fig. 4.2-3c, Ti and Nb particles were not visible in the Ti-16Nb (1300/4) sample.

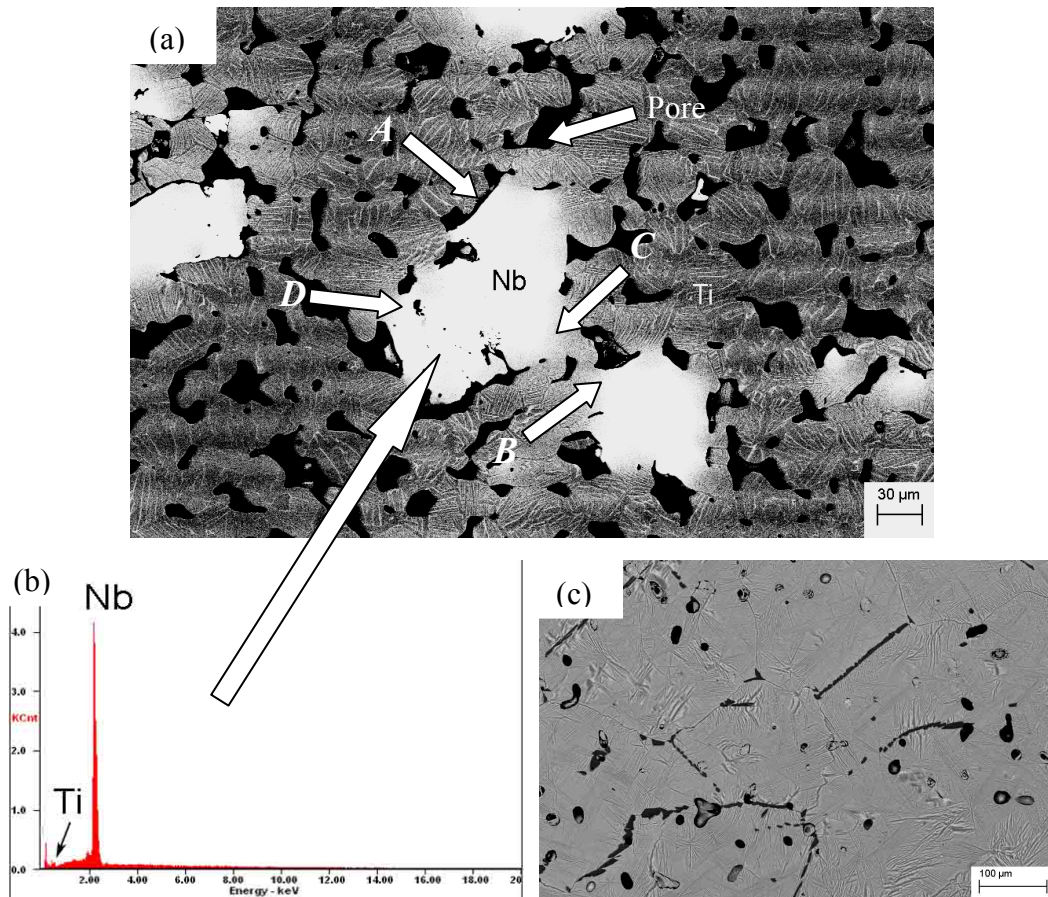


Fig. 4.2-3. BSE-SEM micrographs of (a) Ti-16Nb (1100/4) alloy, showing irregular large particles in the porous matrix; (b) EDS results of the irregular large particle; (c) Ti-16Nb (1300/4) alloy.

4.2.3 Dilatometry

The Ti-16Nb (700/0.03) and Ti-16Nb (1100/4) samples exhibit heterogeneous microstructures composed of Ti and Nb particles, but there are neither visible Ti particles nor Nb particles in the Ti-16Nb (1300/4) alloy. Thus, dilatometry experiments were performed on the Ti-16Nb (DIL) and CP-Ti (DIL) samples, in order to further understand the sintering behavior of the MIM Ti-Nb alloys.

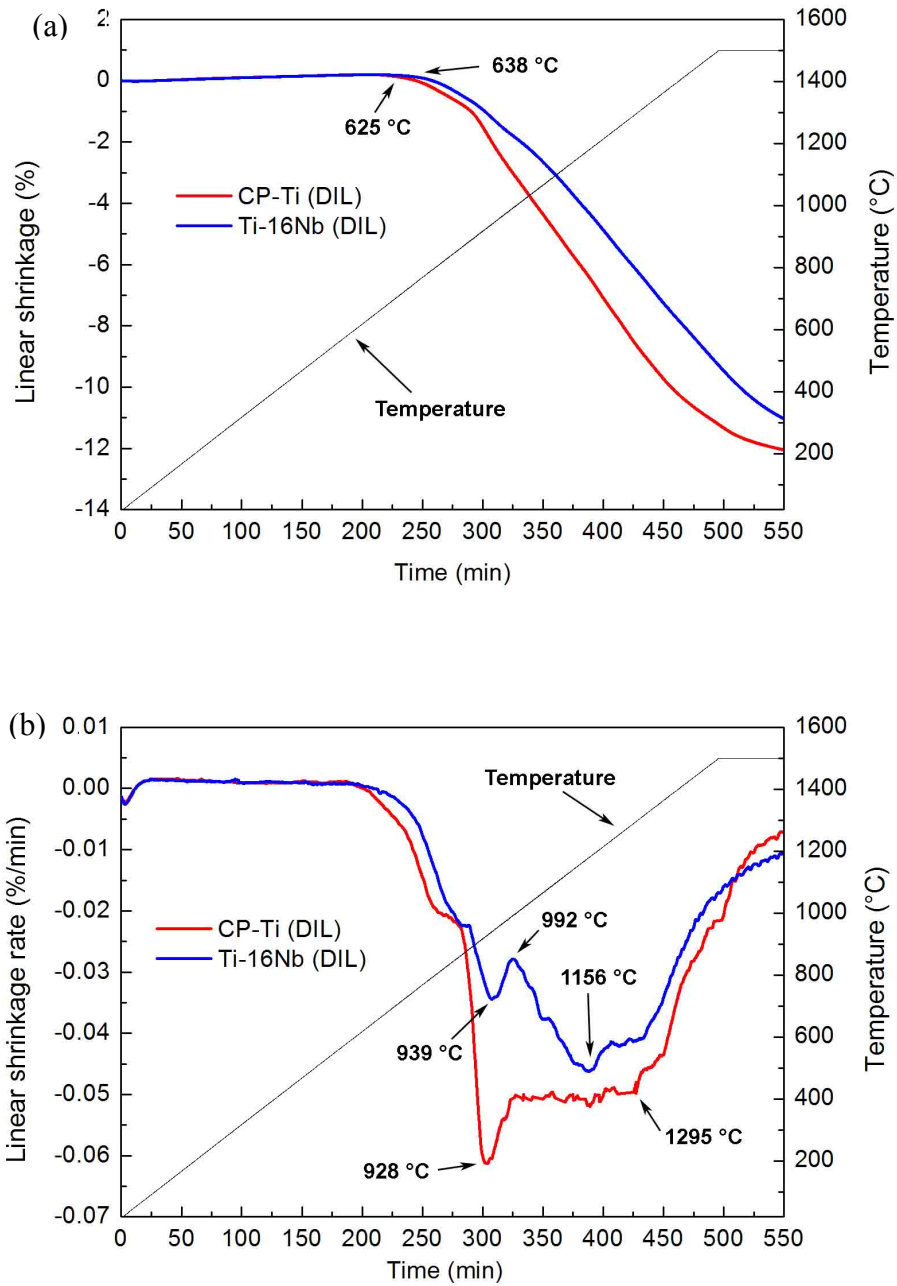


Fig. 4.2-4. Dilatometry of the CP-Ti (DIL) and Ti-16Nb (DIL) samples: a) linear shrinkage (S) and b) linear shrinkage rate (SR).

Figs. 4.2-4a and b present the linear shrinkage (S) and linear shrinkage rate (SR) of both CP-Ti (DIL) and Ti-16Nb (DIL), respectively, obtained by dilatometry experiments. As illustrated in Fig. 4.2-4a, the shrinkage of the CP-Ti (DIL) sample started at 625 °C, whereas that of Ti-16Nb (DIL) began at 638 °C. Fig. 4.2-4b shows

that the *SR* of both samples exhibited the first maximum values of -0.0613 %/min at 928 °C and -0.0344 %/min at 939 °C for CP-Ti (DIL) and Ti-16Nb (DIL), respectively. Afterwards, the *SR* of the CP-Ti (DIL) sample decreased to around -0.05 %/min with increasing temperature until 1295 °C, above which a significant decrease of *SR* was observed. On the other hand, after 939 °C the *SR* of the Ti-16Nb (DIL) sample decreased to -0.0279 %/min at 992 °C, followed by a modest increase, reaching the maximum of -0.0462 %/min at 1156 °C. As the temperature further increased, the *SR* of the Ti-16Nb (DIL) sample gradually decreased.

4.3 The as-sintered samples

Based on the results of Section 4.2, the sintering temperatures 1300 °C, 1400 °C and 1500 °C were used in the following experiments.

4.3.1 Porosity

Fig. 4.3-1 shows the porosity of the as-sintered CP-Ti and Ti-Nb binary alloys. For all compositions, porosity increased with decreasing sintering temperature and time. In addition, the porosity decreased with lower Nb content for samples sintered at the same temperature for the same time.

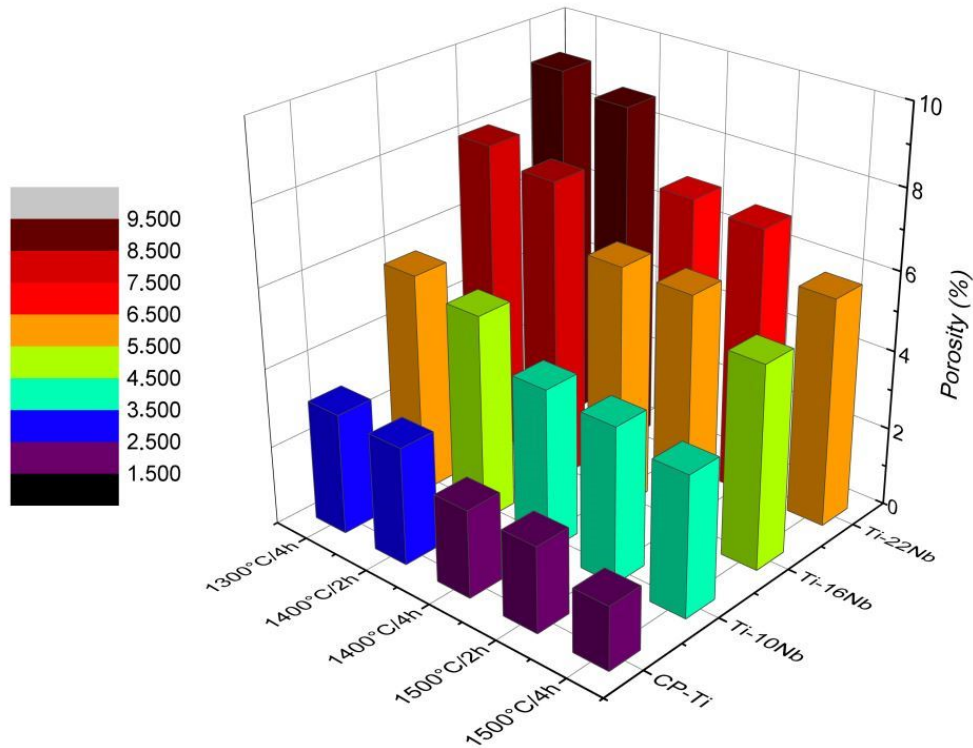


Fig. 4.3-1. Porosity of the as-sintered CP-Ti and Ti-Nb binary alloys.

4.3.2 XRD

The samples sintered at 1500 °C for 4 h exhibited a lower porosity compared with the samples sintered at other temperatures and times. Therefore it was assumed that these samples exhibited the best mechanical properties of all as-sintered samples as they were least affected by detrimental effects of porosity. Thus the major part of the following investigations was performed on this set of specimens sintered at 1500 °C for 4 h. The XRD spectra of CP-Ti (1500/4) and Ti-Nb (1500/4) alloys are presented as shown in Fig. 4.3-2. All the Ti-Nb (1500/4) alloys were composed of α -phase and β -phase, while, only α -phase was found in the CP-Ti (1500/4). It is important to note that for the Ti-Nb (1500/4) alloys, the peak intensities of β -phase gradually increased with higher Nb content.

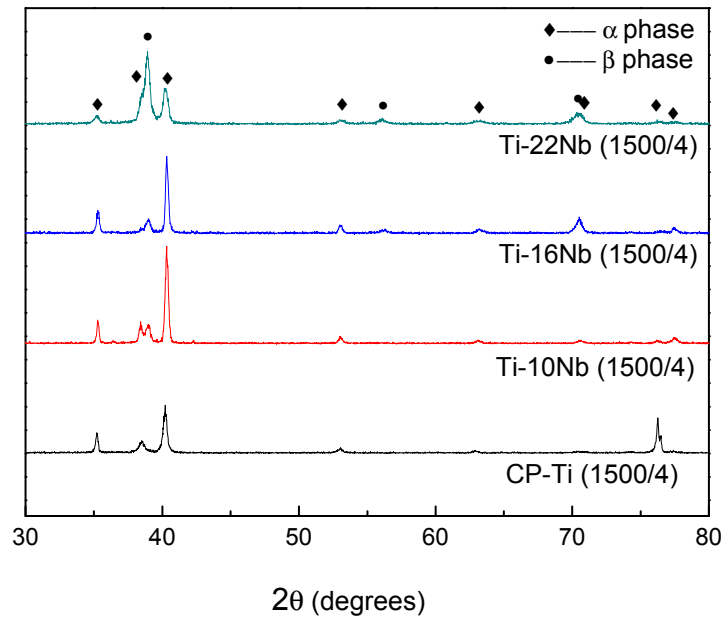
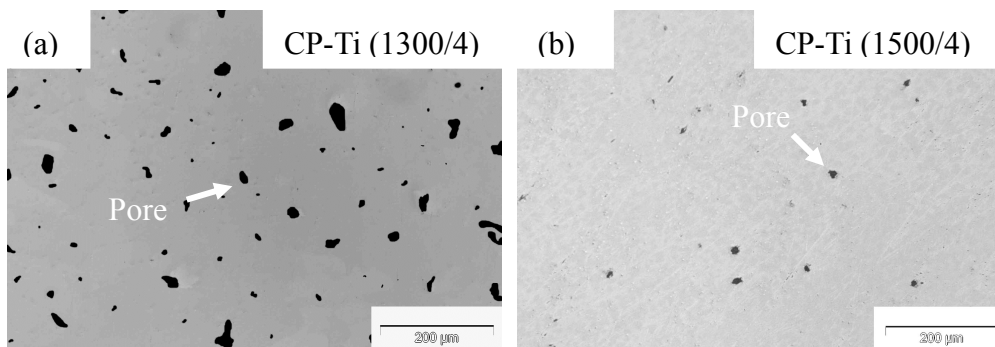


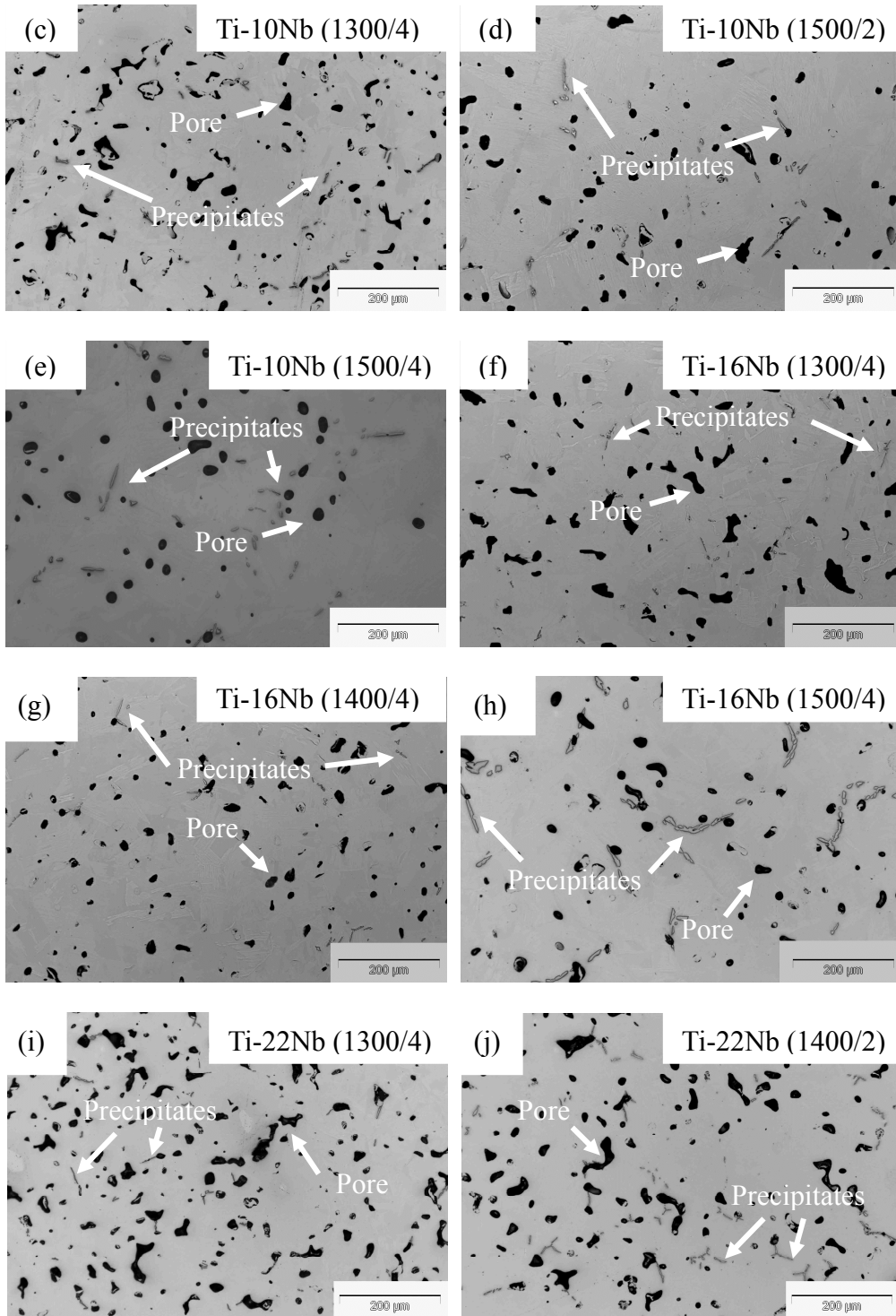
Fig. 4.3-2. XRD results for the CP-Ti (1500/4) and Ti-Nb (1500/4) alloys.

4.3.3 Optical microscopy and SEM

The optical micrographs of some as-sintered CP-Ti and Ti-Nb binary alloys are shown in Fig. 4.3-3. Pores with various sizes and shapes were observed in all samples. CP-Ti (1300/4) and CP-Ti (1500/4) showed round and unconnected pores, and the former shows higher porosity than the latter. No precipitates were found in the as-sintered CP-Ti. However, apart from the presence of irregular pores, fine acicular precipitates, which varied between 50 μm to 100 μm in size, were observed in the as-sintered Ti-Nb alloys.



RESULTS



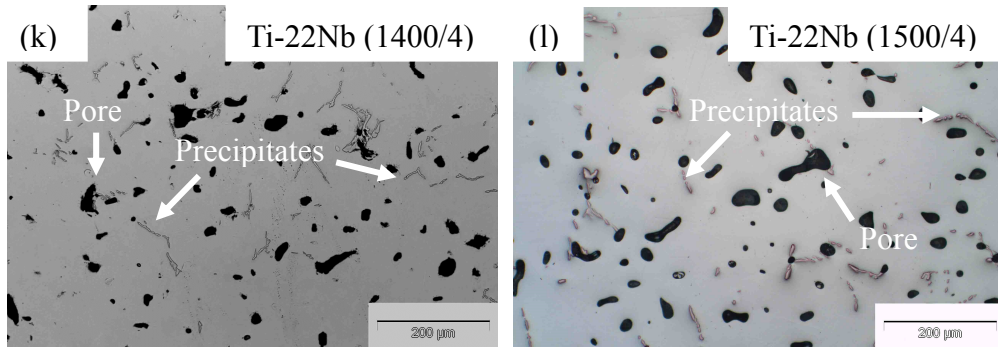
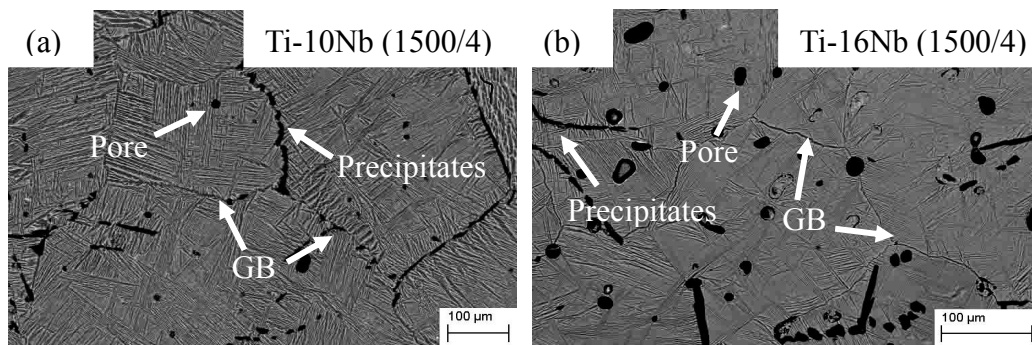


Fig. 4.3-3. Optical microscopy of some as-sintered samples.

Fig. 4.3-4 shows the back-scattered electron (BSE) and secondary electron (SE) SEM micrographs of Ti-10Nb (1500/4), Ti-16Nb (1500/4) and Ti-22Nb (1500/4) samples. As presented in Fig. 4.3-4a, b and c, the Ti-Nb (1500/4) alloys mainly consist of Widmanstätten structures (α -phase and β -phase) with similar grain sizes of about 100~300 μm . Table 4.3-1 presents the grain sizes of the Ti-Nb (1500/4) samples. The long strip shaped precipitates were observed in addition to the pores. Most precipitates were distributed along grain boundaries (GBs). Albeit the grain sizes of different samples were not significantly different, an increased Nb content resulted in more refined $\alpha+\beta$ lamellas, an effect especially pronounced in the Ti-22Nb alloy (take note of higher magnification of Fig. 4.3-4f compared to Fig. 4.3-4d and e). As revealed by the SE-SEM micrographs – Fig. 4.3-4d, e and f, the long strip precipitates were composed of single smaller parts varying from about 5 μm to 30 μm in size.



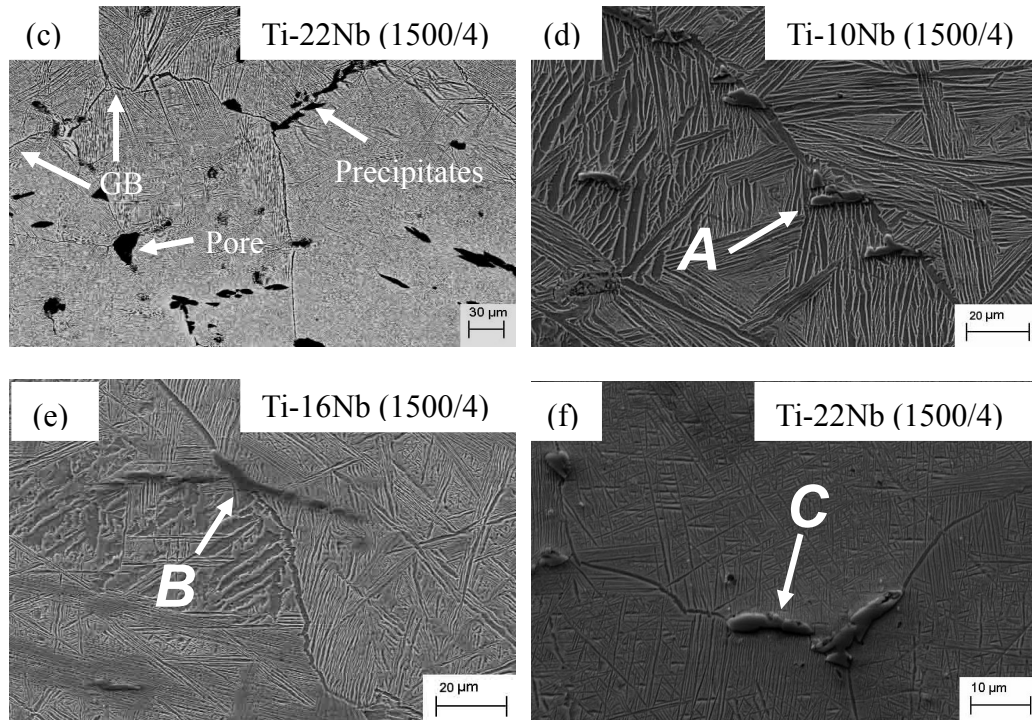


Fig. 4.3-4. SEM micrographs of the Ti-Nb (1500/4) alloys: (a) Ti-10Nb (1500/4) (BSE-SEM image), (b) Ti-16Nb (1500/4) (BSE-SEM image), (c) Ti-22Nb (1500/4) (BSE-SEM image), (d) Ti-10Nb (1500/4) (SE-SEM image), (e) Ti-16Nb (1500/4) (SE-SEM image) and (f) Ti-22Nb (1500/4) (SE-SEM image) (Point *A*, *B* and *C* are the precipitates)

Table 4.3-1 Grain size of the Ti-Nb (1500/4) samples (μm).

Sample	Grain size
Ti-10Nb (1500/4)	217 ± 161
Ti-16Nb (1500/4)	236 ± 122
Ti-22Nb (1500/4)	155 ± 84.3

Table 4.3-2 EDS analyses of the precipitates in Fig. 4.3-4 (at.%).

	C	Nb	Ti
Point <i>A</i> in Fig. 4.3-4d	43.37	2.22	55.60
Point <i>B</i> in Fig. 4.3-4e	40.90	1.99	57.10
Point <i>C</i> in Fig. 4.3-4f	43.04	1.80	55.16

Table 4.3-2 shows the EDS results of the precipitates marked in Fig. 4.3-4. The long strip shaped precipitates were identified to be titanium carbides (TiC_x). No

dependence of morphology and composition of the TiC_x particles on Nb content was found.

4.3.4 Young's modulus

RUS technique was used to measure the Young's modulus of the as-sintered CP-Ti and Ti-Nb binary alloys. As shown in Fig. 4.3-5, the Young's modulus decreased with decreasing sintering temperature and time for each composition. In contrast, the Young's modulus increased significantly with lower Nb content for each set of sintering conditions.

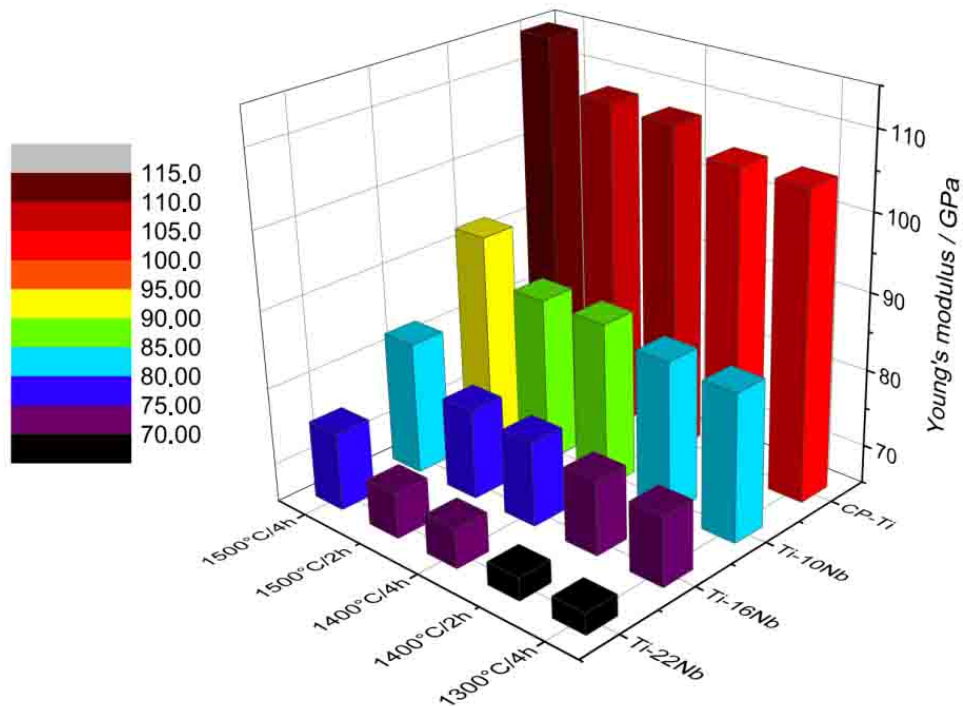


Fig. 4.3-5. Young's modulus of the as-sintered CP-Ti and Ti-Nb alloys determined by RUS method.

4.3.5 Tensile properties

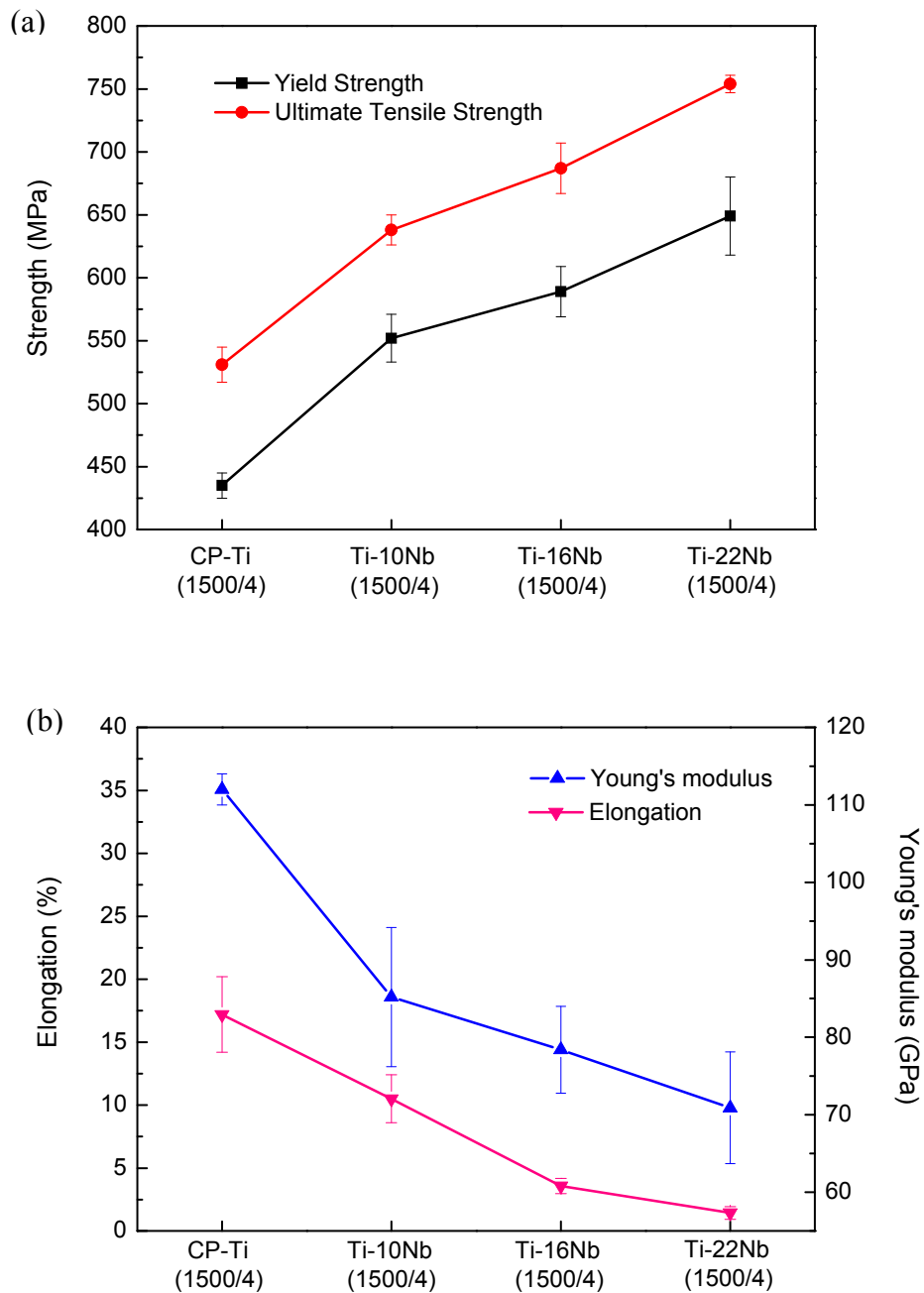


Fig. 4.3-6. Tensile properties of the CP-Ti (1500/4) and Ti-Nb (1500/4) alloys (a) Yield strength and ultimate tensile strength; (b) Elongation and Young's modulus.

Since only the samples sintered at 1500 °C for 4 h showed acceptable porosity, the tensile tests were only performed on the CP-Ti (1500/4) and Ti-Nb (1500/4) samples. The tensile properties these samples are plotted in Fig. 4.3-6. In general, the samples with a higher Nb content exhibited less elongation and lower Young's modulus but

higher yield strength (YS) and ultimate tensile strength (UTS). It is important to note that both Ti-16Nb (1500/4) and Ti-22Nb (1500/4) exhibited a rather poor ductility of 1~4 %. The Young's modulus of the CP-Ti (1500/4) and Ti-Nb (1500/4) samples determined from tensile tests was in the same range as that measured by the RUS methods shown in Fig. 4.3-5.

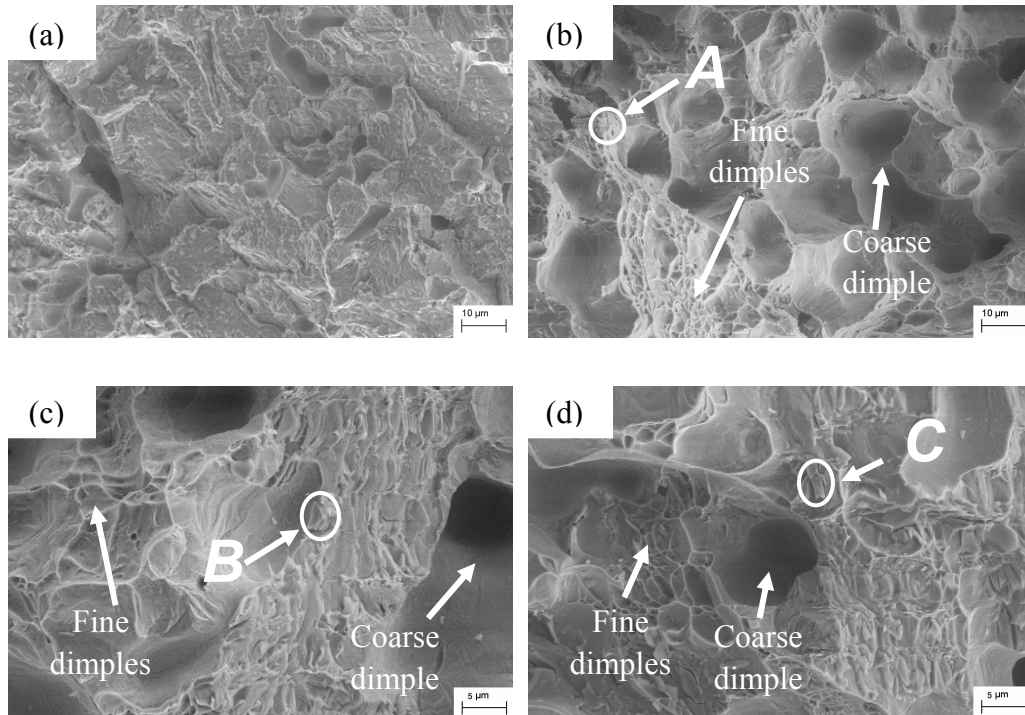


Fig. 4.3-7. The fracture surface of (a) CP-Ti (1500/4), (b) Ti-10Nb (1500/4), (c) Ti-16Nb (1500/4) and (d) Ti-22Nb (1500/4), showing particles and dimples in all Ti-Nb (1500/4) binary alloys.

Table 4.3-3 EDS analyses of the precipitates in Fig. 4.3-7 (at.%).

	C	Nb	Ti
Point <i>A</i> in Fig. 4.3-7b	38.16	2.10	59.64
Point <i>B</i> in Fig. 4.3-7c	31.68	2.27	66.05
Point <i>C</i> in Fig. 4.3-7d	37.49	2.52	59.98

To further understand the reasons for the differences in the mechanical properties of the CP-Ti (1500/4) and Ti-Nb (1500/4) alloys, the fracture surfaces of the failed tensile specimens were investigated (see Fig. 4.3-7). The fracture surface of the CP-Ti (1500/4) tensile specimen showed a honeycomb structure. All the Ti-Nb (1500/4)

alloys exhibited a bimodal dimple structure. The size of “coarse dimples” of the Ti-Nb (1500/4) binary alloys was similar to the pore size in the alloys. The “fine dimples” were also observed between the “coarse dimples”. In Fig. 4.3-7b, c and d, particles were observed on the fracture surface of the Ti-Nb (1500/4) alloys. EDS results (presented in Table 4.3-3) revealed that the particles were TiC_x .

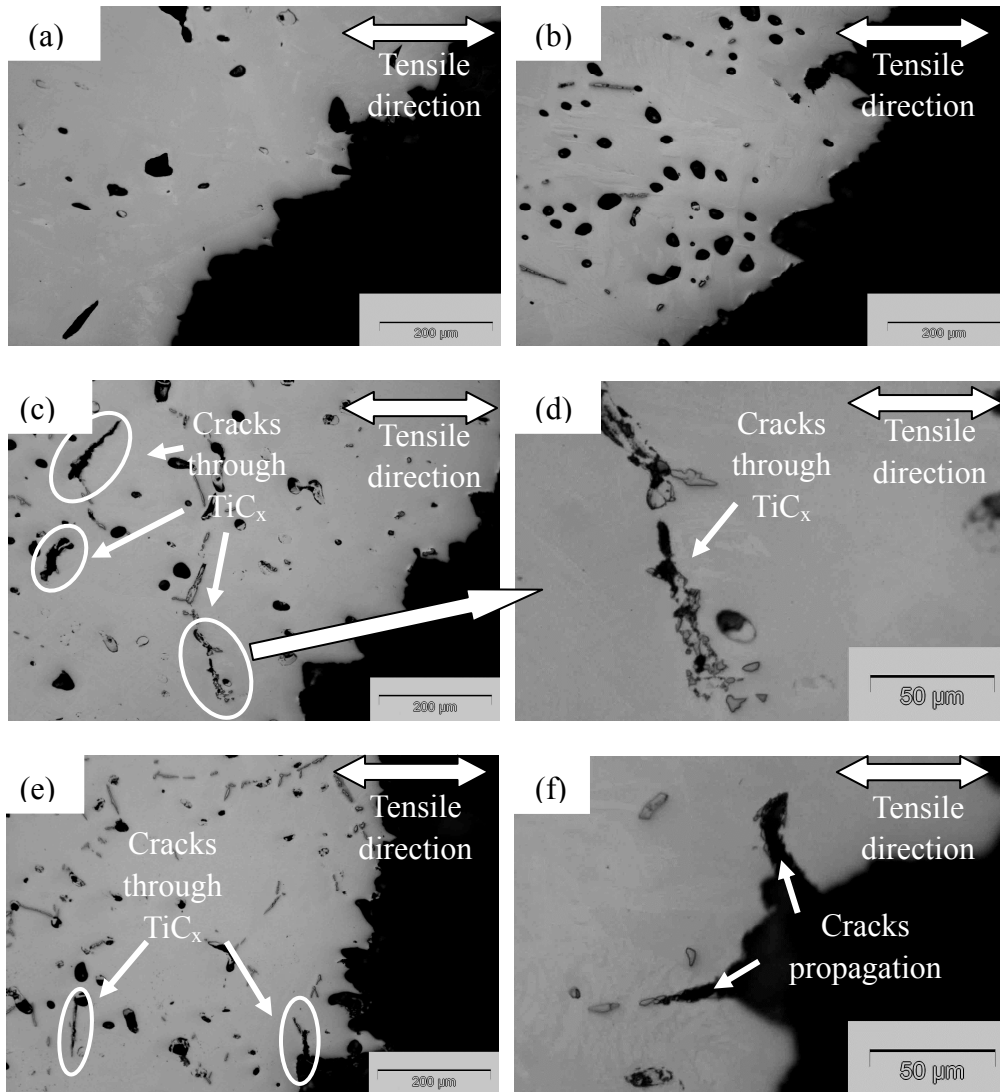


Fig. 4.3-8. Optical micrographs of cross-sections of (a) CP-Ti (1500/4); (b) Ti-10Nb (1500/4); (c, d) Ti-16Nb (1500/4); (e, f) Ti-22Nb (1500/4); the cracks through TiC_x particles are marked.

In order to analyze the fracture processes of the CP-Ti (1500/4) and Ti-Nb (1500/4) alloys, the longitudinal sections of the fractured tensile specimens were examined, as

shown in Fig. 4.3-8. No evidence of crack initiation or propagation were observed beneath the fracture surfaces in both CP-Ti (1500/4) and Ti-10Nb (1500/4) samples. However, in the Ti-16Nb (1500/4) and Ti-22Nb (1500/4) samples, cracks cutting through TiC_x particles were detected beneath the fracture surfaces in all three Ti-Nb (1500/4) samples. For instance, Fig. 4.3-8d presents such cracks in Ti-16Nb (1500/4). TiC_x particles were found lying along the fracture surfaces of the Ti-10Nb (1500/4) samples. Besides, crack propagation from the fracture surface through TiC_x particles was observed in Fig. 4.3-8f.

4.4 The as-HIPed samples

4.4.1 XRD

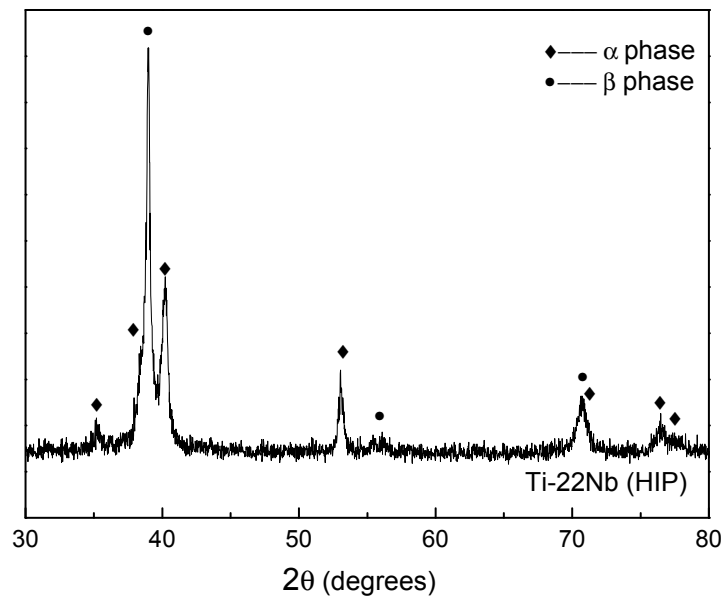


Fig. 4.4-1. XRD results for the Ti-22Nb (HIP) alloys.

Fig. 4.4-1 shows the XRD spectrum of the Ti-22Nb (HIP) alloys. The Ti-22Nb (HIP) alloy was composed of only α -phase and β -phase.

4.4.2 Optical microscopy

The HIP process was applied to obtain fully dense samples. Fig. 4.4-2 shows the optical micrographs of the CP-Ti (HIP) and Ti-Nb (HIP) samples. All samples exhibited pore-free structures. The acicular precipitates were also observed in the Ti-Nb (HIP) samples. The bulk density ρ_H of CP-Ti (HIP), Ti-10Nb (HIP), Ti-16Nb (HIP) and Ti-22Nb (HIP) were measured to be 4.501 g/cm³, 4.792 g/cm³, 4.924 g/cm³ and 5.080 g/cm³, respectively.

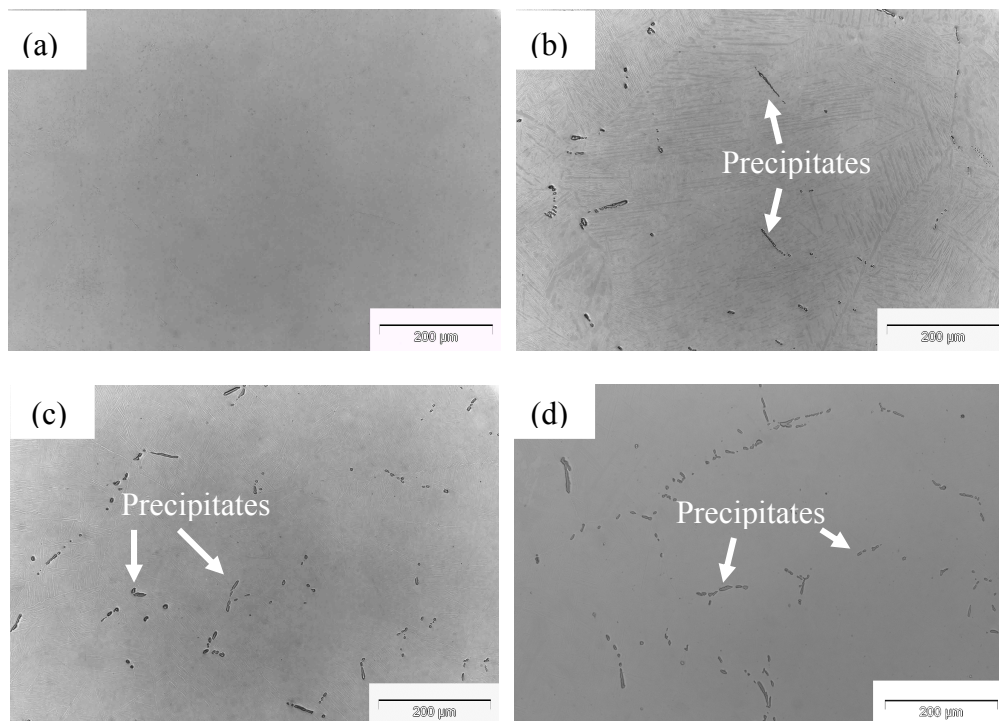


Fig. 4.4-2. Optical microscopy of (a) CP-Ti (HIP); (b) Ti-10Nb (HIP); (c) Ti-16Nb (HIP) and (d) Ti-22Nb (HIP)

4.4.3 Tensile properties and RUS measurements

The tensile properties of the CP-Ti (HIP) and Ti-Nb (HIP) alloys are summarized in Fig. 4.4-3. The same trends as for the CP-Ti (1500/4) and Ti-Nb (1500/4) samples with respect to tensile strength vs. Nb content, elongation vs. Nb content and Young's modulus vs. Nb content were observed in the as-HIPed samples. In general, the

as-HIPed samples showed a higher strength and Young's modulus but similar elongation compared with the corresponding CP-Ti (1500/4) and Ti-Nb (1500/4) samples, whereas the elongation of the CP-Ti (HIP) was about 40% higher than that of the CP-Ti (1500/4).

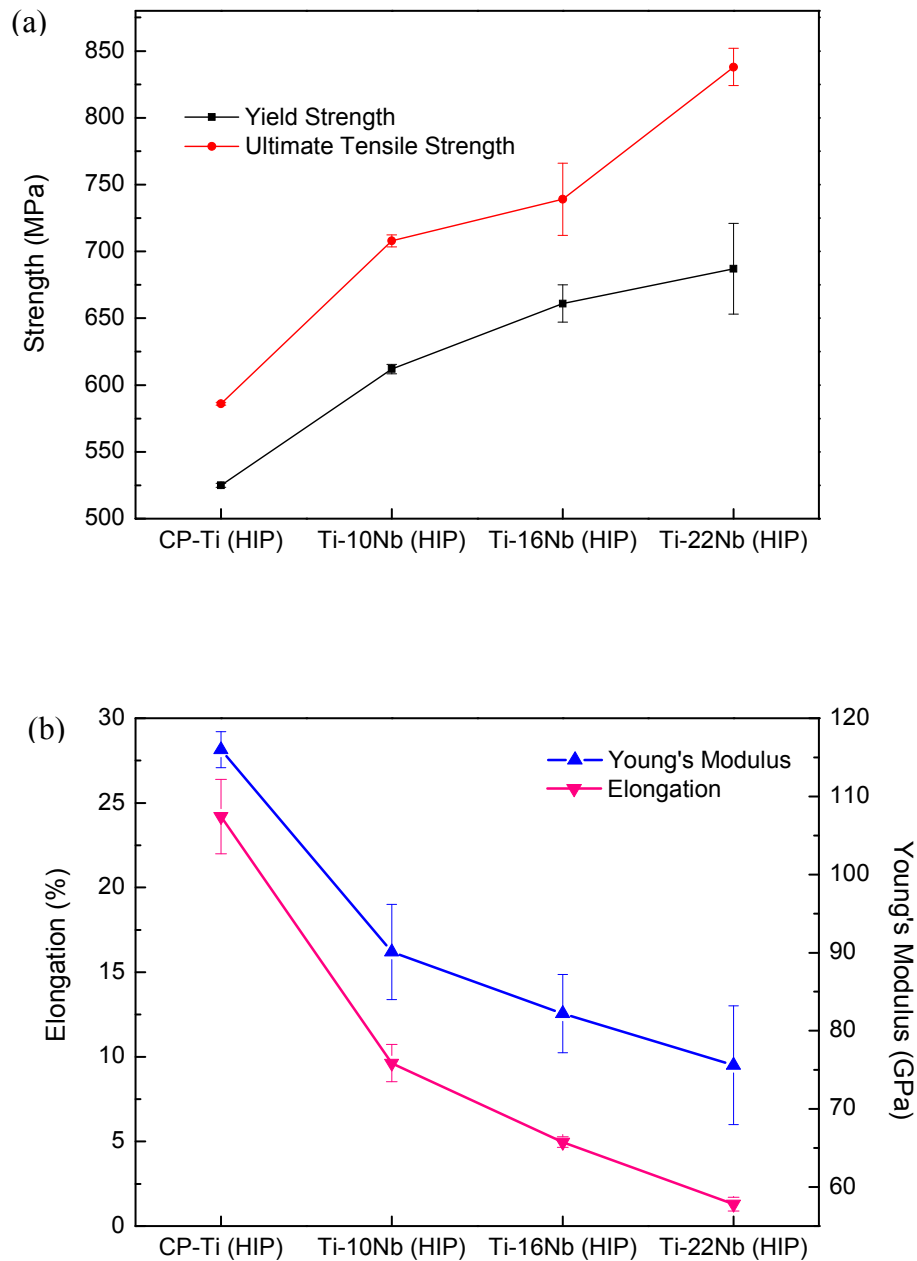


Fig. 4.4-3. Tensile properties of the CP-Ti (HIP) and Ti-Nb (HIP) alloys (a) Yield strength and ultimate tensile strength; (b) Elongation and Young's modulus.

Fig. 4.4-4 illustrates the fracture surface of the Ti-16Nb (HIP) and Ti-22Nb (HIP) samples. The Ti-16Nb (HIP) sample presented a fracture surface with “fine dimples” and some evidence of intergranular fracture. As shown in Fig. 4.4-4b, the particles, which were identified as TiC_x by EDS, were found on the fracture surface. A crack was observed in a TiC_x particle. In Fig. 4.4-4c, the Ti-22Nb (HIP) sample exhibited an intergranular fracture. Fig. 4.4-4d shows the triple point of grain boundaries as marked in Fig. 4.4-4c. The crack was found to propagate along grain boundaries. In addition, the TiC_x particles in Fig. 4.4-4d were observed adjacent to the fracture path. It should be noted that the “coarse dimples” in Ti-Nb (1500/4) alloys were not observed in both Ti-16Nb (HIP) and Ti-22Nb (HIP) alloys.

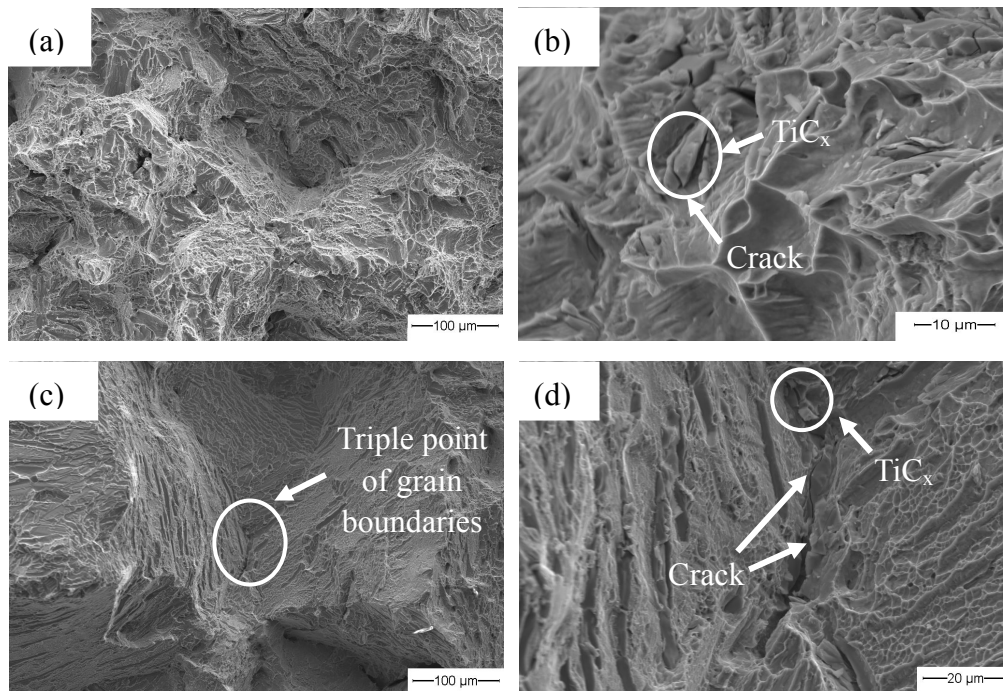


Fig. 4.4-4. The fracture surface of (a, b) Ti-16Nb (HIP), (c, d) Ti-22Nb (HIP), showing brittle fracture in both alloys.

In order to obtain the Young's modulus of the CP-Ti (HIP) and Ti-Nb (HIP) alloys with higher accuracy, the RUS method was applied. Fig. 4.4-5 presents the Young's modulus of the CP-Ti (HIP) and Ti-Nb (HIP) alloys measured by RUS technique, which was comparable to the values obtained from tensile tests.

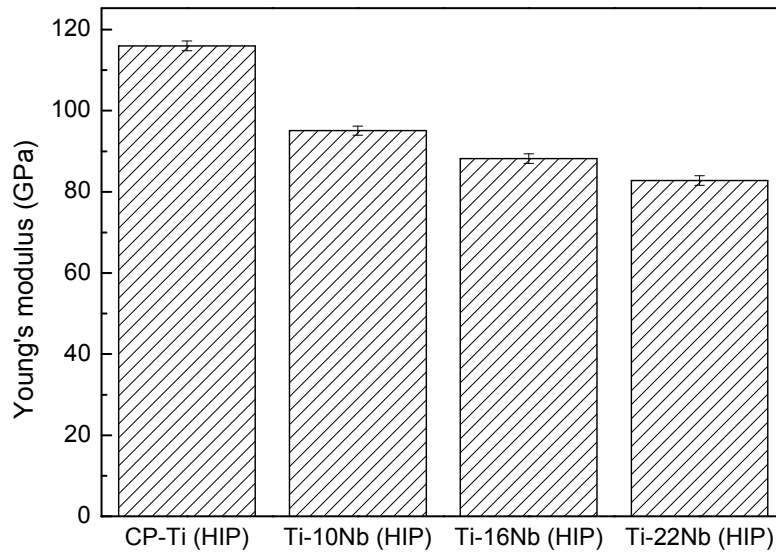


Fig. 4.4-5. Young's modulus of the CP-Ti (HIP) and Ti-Nb (HIP) alloys measured by RUS technique.

4.5 TiC_x precipitates

4.5.1 Carbide area fractions

Titanium carbide particles were observed in the as-sintered Ti-Nb alloys and as-HIPed Ti-Nb alloys as illustrated in Section 4.3 and Section 4.4, respectively. The titanium carbide area fractions in the CP-Ti (1500/4), Ti-Nb (1500/4) alloys and the Ti-22Nb (HIP) alloy are presented in Fig. 4.5-1. The carbide area fractions increased noticeably with increasing Nb content. The carbide area fraction was not changed by the application of a HIP process. It is important to note that the carbide area fraction of the CP-Ti (1500/4) was zero.

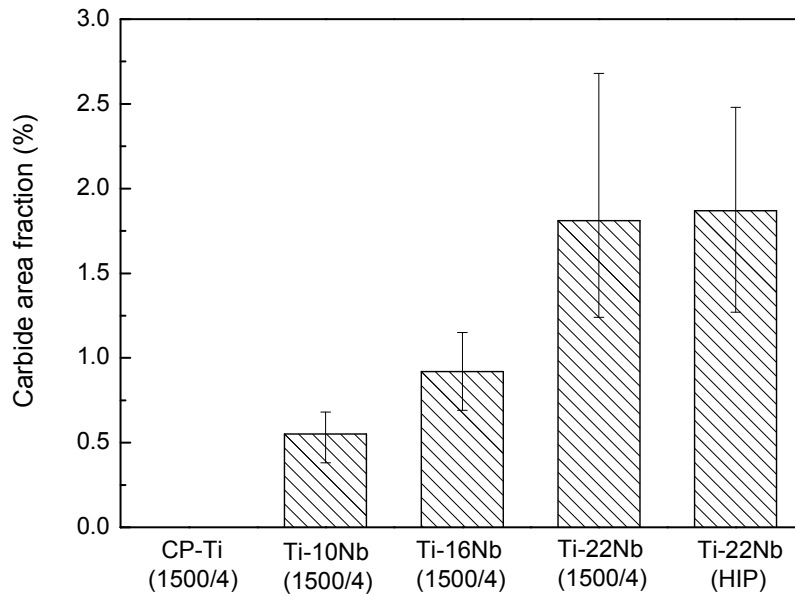


Fig. 4.5-1. Carbide area fraction in the CP-Ti (1500/4), Ti-Nb (1500/4) alloys and the Ti-22Nb (HIP) alloy.

4.5.2 TEM and SAED analyses

In order to investigate the nature of the TiC_x precipitates, the TiC_x precipitates in Ti-22Nb (1500/4) were characterized by SAED (Selected Area Electron Diffraction) in the TEM. Respective bright field TEM micrographs and SAED patterns of Ti-22Nb (1500/4) are presented in Fig. 4.5-2. As shown in Fig. 4.5-2a, the TiC_x precipitate is surrounded by the matrix. Fig. 4.5-2b, c, d and e display the SAED patterns from the TiC_x precipitate. The TiC_x exhibits a face-centered cubic (FCC) structure with a lattice parameter of $a = 4.30 \text{ \AA}$. Between the main diffraction spots of the TiC_x precipitate, extra diffraction maxima with much lower intensity, e.g. $\frac{1}{2}(11\bar{1})$ and $\frac{1}{2}(3\bar{1}3)$, were observed, particularly at the [011] and [112] zone axes as presented in Fig. 4.5-2b and e. According to previous studies [117, 118], the TiC_x precipitate in the present investigation is assumed as $Fd\bar{3}m-Ti_2C$.

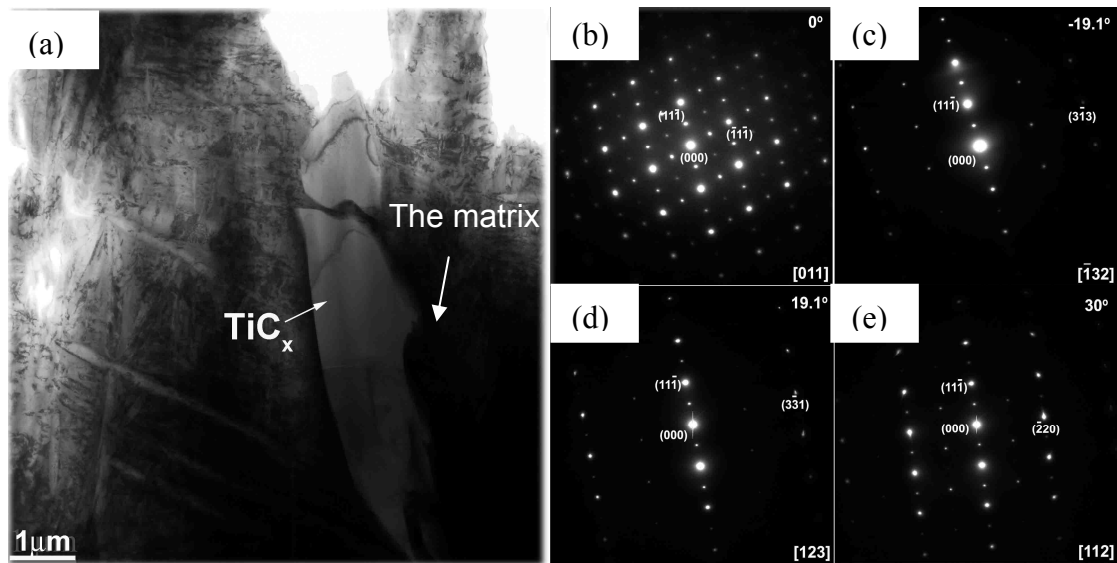


Fig. 4.5-2. TEM micrograph and SAED patterns of the as-sintered Ti-22Nb (a) the bright field image, (b-e) SAED patterns showing TiC_x reflections from (b) $[011]$; (c) $[\bar{1}32]$ from $[011]$; (d) $[123]$ from $[011]$; (e) $[112]$ from $[011]$.

Fig. 4.5-3 presents the SAED patterns from both the TiC_x precipitate and the matrix around it. As obvious from Fig. 4.5-3c, a clear crystallographic relationship between the TiC_x precipitate and its surrounding β -Ti was found. The reflections from hexagonal close-packed (HCP) α -Ti were also observed, although only β -Ti was found around the TiC_x precipitate in Fig. 4.5-3b.

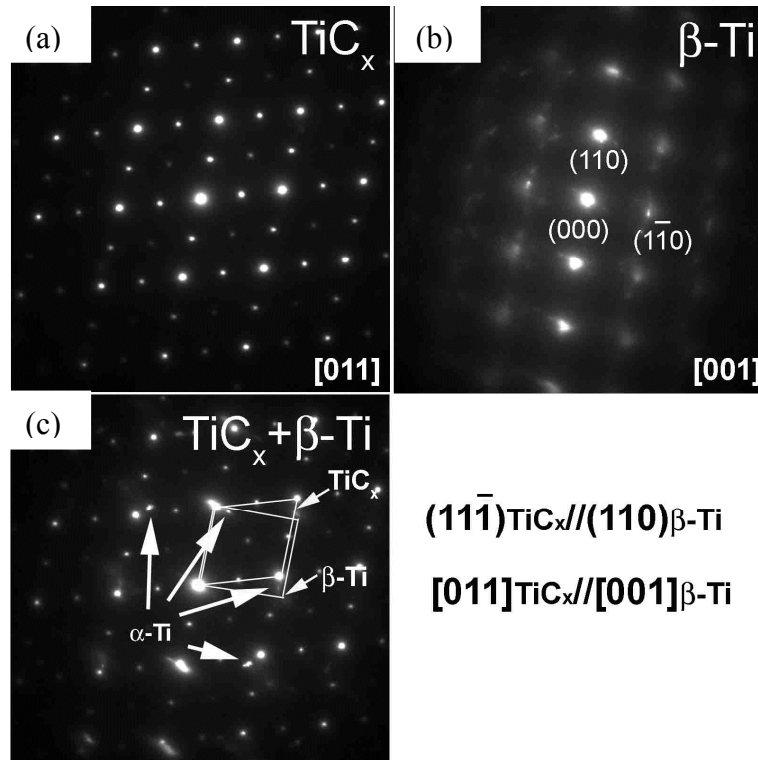


Fig. 4.5-3. SAED patterns of the TiC_x precipitate in Fig. 4.5-2a (a) TiC_x from $[011]$; and its surrounding matrix (b) $\beta\text{-Ti}$ reflections from $[001]$; (c) both TiC_x and $\beta\text{-Ti}$ as well as several additional diffraction spots from $\alpha\text{-Ti}$.

4.5.3 In situ HEXRD analyses

To study the structural evolution of the carbides in the as-sintered Ti-Nb alloys, in situ synchrotron HEXRD measurements for the Ti-22Nb (1500/4) were performed. Fig. 4.5-4 displays the results as evolution of the X-ray profiles during the measurement time within the heating and cooling cycle shown in Fig. 3.5-4. The pyrometric temperature measurements as well as the 15 points (Point A to Point O) (top) are synchronized in time with the HEXRD spectra displayed as intensity map. The grey scale level corresponds to a higher or lower intensity of the respective X-ray peaks of various phases. Observing the development of such a peak over time gives a qualitative hint if the fraction of this phase increases (increasing intensity), decreases (reducing intensity) or dissolves (intensity vanishes).

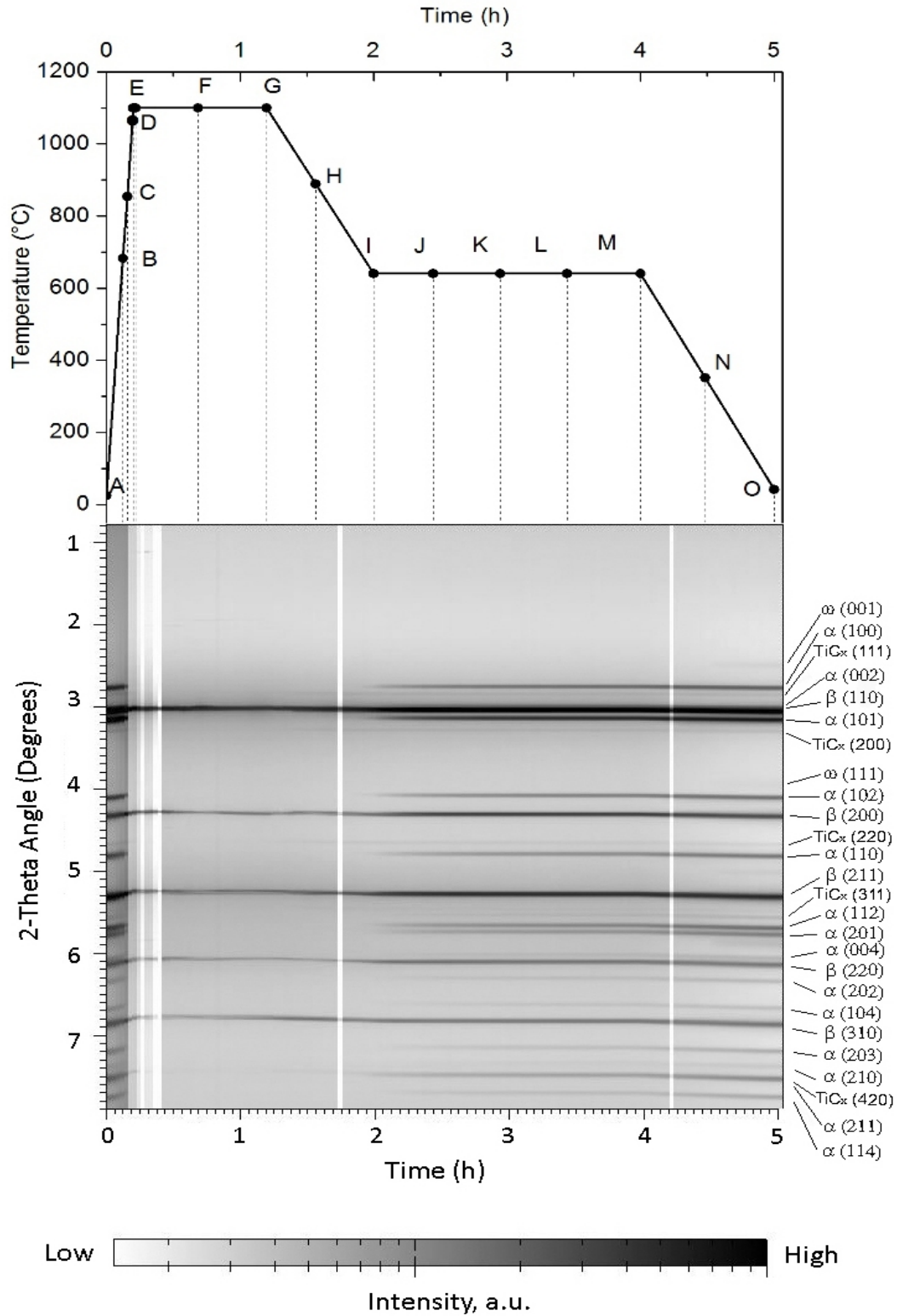


Fig. 4.5-4. Time evolution of X-ray diffraction spectra of the Ti-22Nb (1500/4) alloy. The gray value in the HEXRD spectra corresponds to the diffracted radiation intensity. On the right panel it is mark which angular position corresponds to which Bragg peak of which phase. The 15 points – Point *A* to Point *O* - are presented on the top of the HEXRD spectra.

In order to better display the evolution of various phases intensities, a 3-dimensional graph showing the in situ synchrotron XRD patterns of the main peaks of α , β and TiC_x phases from Point *A* to Point *O* is presented in Fig. 4.5-5. For the sake of presenting more details regarding the evolution of the microstructure in the Ti-22Nb (1500/4) alloy, sections of the Debye-Scherrer rings at selected points of the whole cycle are shown in Fig. 4.5-6.

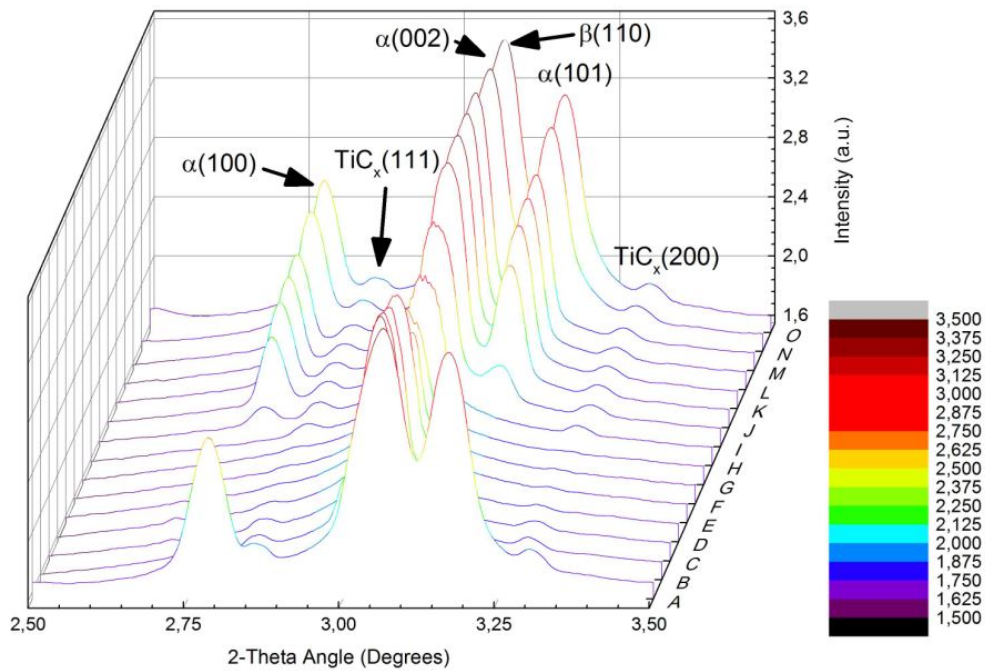


Fig. 4.5-5. The evolution of the intensity of selected peaks of α , β and TiC_x phases from Point *A* to Point *O*.

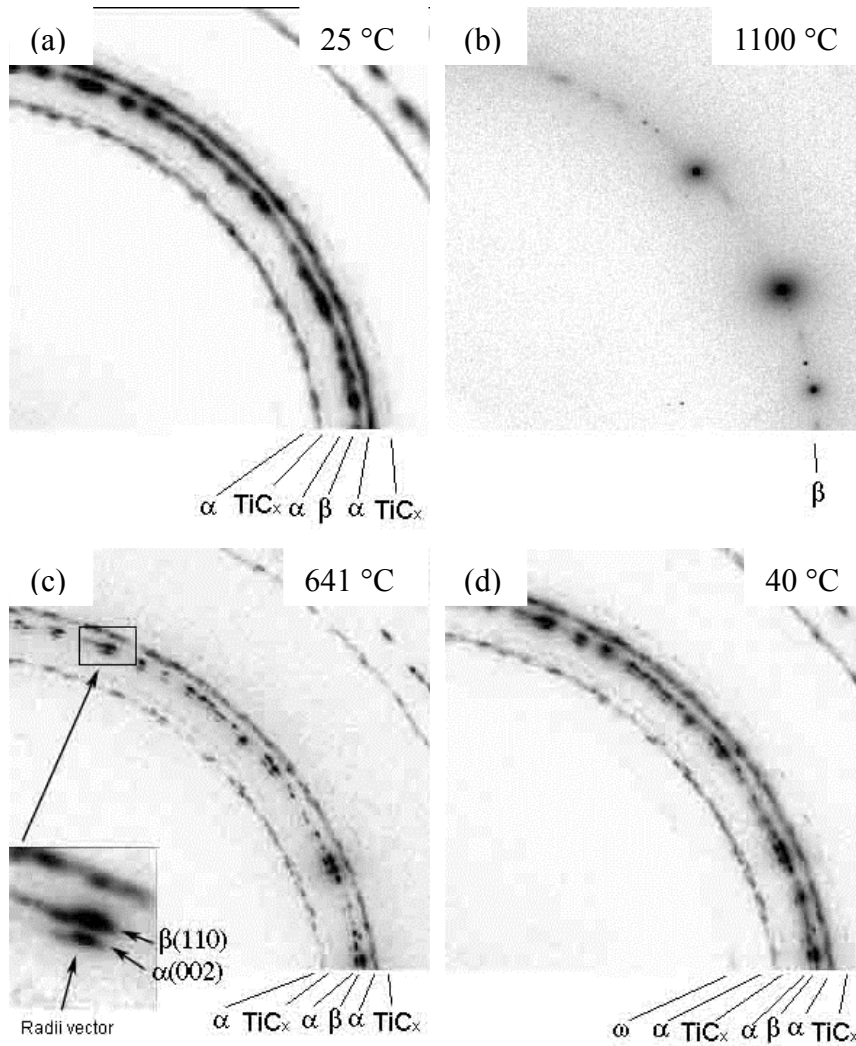


Fig. 4.5-6. Sections of the full Debye-Scherrer rings at selected points of the in situ experiment. The origin of the reciprocal space, i.e. the common ring center, is to the left at the bottom of each figure.

(a) Point *A*; (b) Point *G*; (c) Point *I*; (d) Point *O*.

The original diffraction pattern was recorded at Point *A*. As shown in Fig. 4.5-5 and Fig. 4.5-6a, the Ti-22Nb (1500/4) showed a typical $\alpha+\beta$ pattern with visible TiC_x reflections. The α -phase exhibits a hexagonal close-packed (HCP) crystal structure with lattice parameters of $a = b = 2.951 \text{ \AA}$, $c = 4.683 \text{ \AA}$. The β -phase shows a body-centered cubic (BCC) structure with a lattice parameter of $a = 3.277 \text{ \AA}$. Albeit the TiC_x reflections were observed, the volume fraction of TiC_x particles can hardly be analyzed quantitatively, due to the rather low intensity of TiC_x reflections compared with that of the reflections of α -phase and β -phase. The TiC_x phase presents a

face-centered cubic (FCC) structure with a lattice parameter of $a = 4.300 \text{ \AA}$.

As the temperature increased from Point *A* to Point *E*, the α -phase and TiC_x reflections gradually disappeared (see Fig. 4.5-5). It should be noted that the slight shifting of reflections to the smaller angles was observed in all the phases. At Point *E*, when the 1100 °C annealing started, only the β -phase reflections were visible. From Point *E* to Point *G*, neither α -phase nor TiC_x phase was detected. As shown in Fig. 4.5-6b, there were very few spots on the detector at Point *G*. The lattice parameter of β -phase shifts to $a = 3.315 \text{ \AA}$, which is an increase of approximately 0.04 \AA compared to Point *A*. During the first cooling step (from Point *G* to Point *I*), distinct reflections of the α -phase and TiC_x started to emerge. As shown in Fig. 4.5-6c, there were more spots on (110) Bragg reflections of the β -phase, compared with the reflection pattern in Fig. 4.5-6b. Besides, the $\alpha(002)$ reflection and the $\beta(110)$ reflection were observed to be face-to-face, i.e., they were parallel to each other and lying on the same radii vector. At the final cooling step (from Point *M* to Point *O*), the further growth of the α -phase peak intensities was obvious. At the end of the cycle (Point *O*), the Ti-22Nb (1500/4) alloy exhibited almost the same reflection patterns as the original state (Point *A*). However, trace amounts of ω -phase were observed as shown in Fig. 4.5-5 and Fig. 4.5-6d.

4.6 The as-quenched samples

4.6.1 XRD

The XRD spectrum of Ti-22Nb (HIP+Q) alloy is displayed in Fig. 4.6-1. Compared with the spectrum of Ti-22Nb (HIP) shown in Fig. 4.4-1, one more phase – the orthorhombic α'' martensite was detected in Ti-22Nb (HIP+Q) besides the presence of α and β phases. No peaks of TiC_x particles were observed.

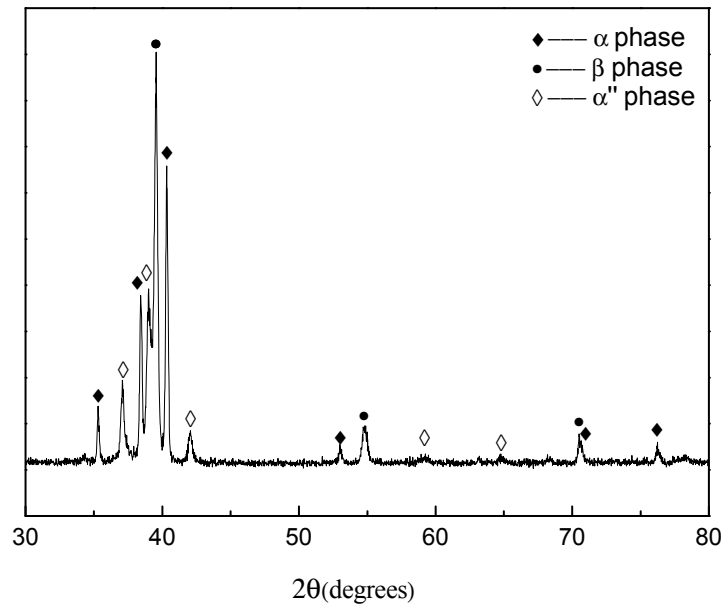


Fig. 4.6-1. XRD results for the Ti-22Nb (HIP+Q).

4.6.2 Optical microscopy and SEM

The annealing and subsequent water quenching were applied to the Ti-22Nb (1500/4) and Ti-22Nb (HIP) at 641 °C (± 3 °C) for 120 h in order to dissolve the TiC_x particles. Fig. 4.6-2 shows the optical micrographs of Ti-22Nb (1500/4+Q) and Ti-22Nb (HIP+Q). Compared with the TiC_x particles in the Ti-22Nb (1500/4) sample shown in Fig. 4.3-31, both as-quenched alloys exhibited a microstructure with much lower carbide area fraction as presented in Fig. 4.6-3.

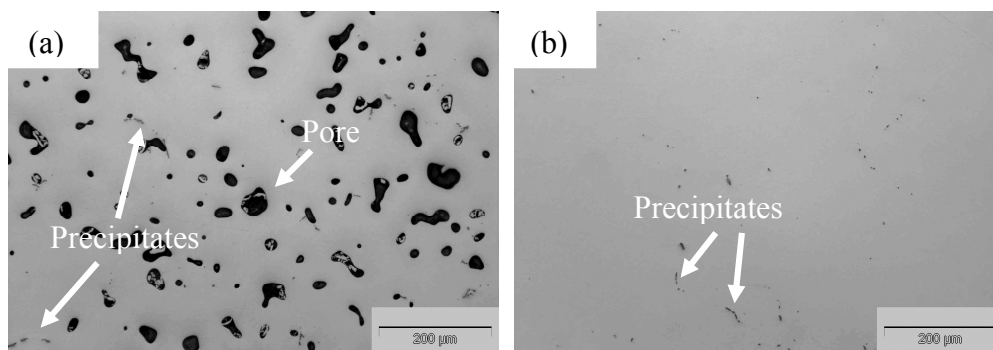


Fig. 4.6-2. Optical microscopy of (a) Ti-22Nb (1500/4+Q) and (b) Ti-22Nb (HIP+Q).

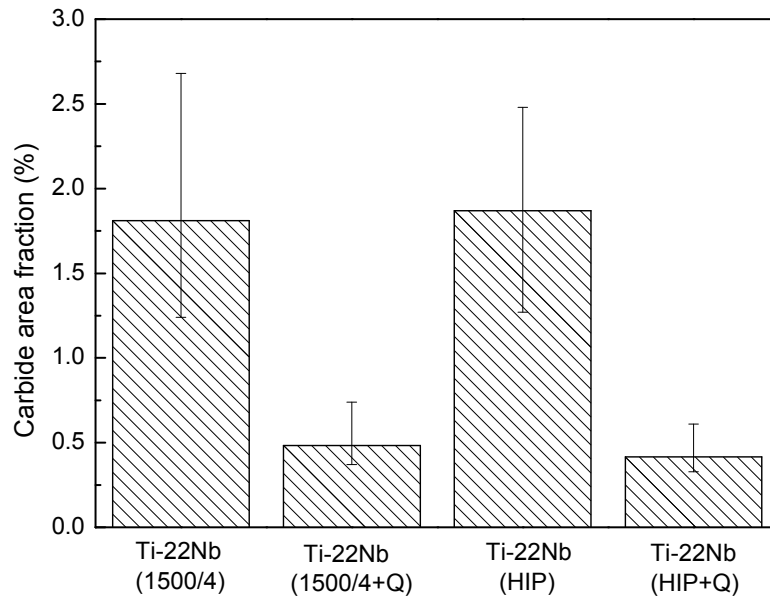


Fig. 4.6-3. Carbide area fractions of the Ti-22Nb (1500/4+Q) and Ti-22Nb (HIP+Q) samples. Those of the Ti-22Nb (1500/4) and Ti-22Nb (HIP) alloys were shown for comparison

A further analysis on the precipitates by SEM and EDS is presented in Fig. 4.6-4 and Table 4.6-1. The precipitates in the Ti-22Nb (1500/4+Q) and Ti-22Nb (HIP+Q) samples were TiC_x particles, which were lying on the grain boundary.

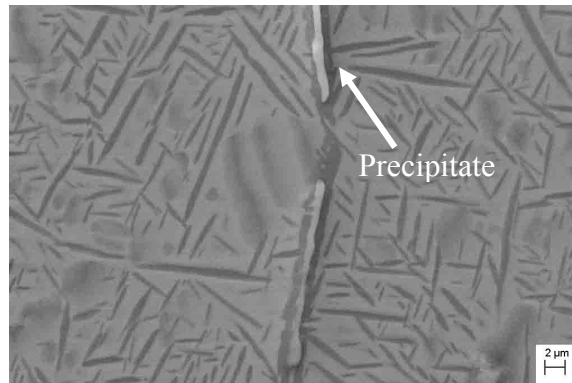


Fig. 4.6-4. SEM micrograph of the TiC_x particles lying on the grain boundary of the Ti-22Nb (1500/4+Q) sample.

Table 4.6-1 EDS analyses of the precipitate in Fig. 4.6-4 (at.%).

C	Nb	Ti
34.28	2.15	63.57

4.6.3 Tensile properties

Fig. 4.6-5 plots the tensile curves of the as-quenched samples as well as the Ti-22Nb (1500/4) and Ti-22Nb (HIP) alloys for comparison. It can be seen that after annealing and subsequent quenching, the elongation increased significantly from less than 2.5 % to 6~11 %, but the tensile strength, especially the yield strength decreased dramatically. The change in Young's modulus was not significant.

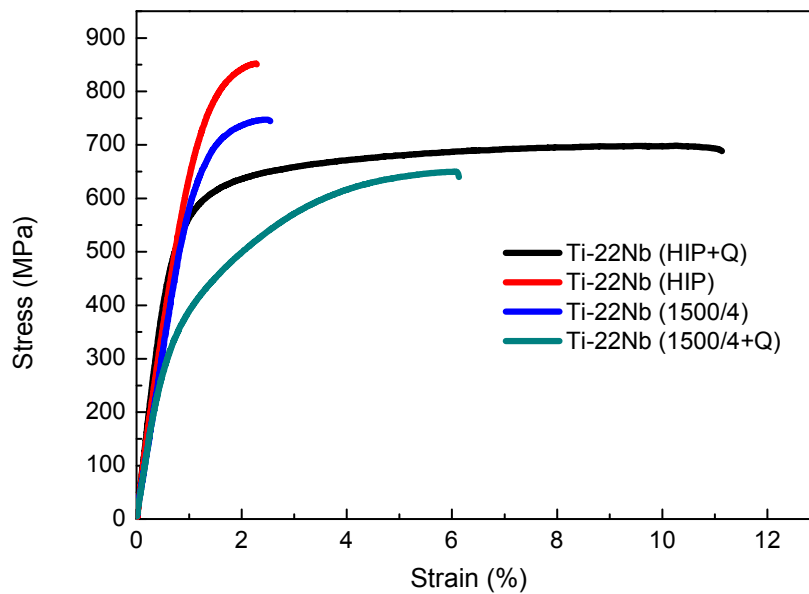


Fig. 4.6-5. Stress-strain curves of tensile tests of the Ti-22Nb (1500/4+Q) and Ti-22Nb (HIP+Q) samples; the curves of the Ti-22Nb (1500/4) and Ti-22Nb (HIP) alloys were plotted for comparison.

Fig. 4.6-6 shows the SEM micrographs of the fracture surface of the as-quenched alloys – Ti-22Nb (1500/4+Q) and Ti-22Nb (HIP+Q) after tensile testing. In Fig. 4.6-6a, the Ti-22Nb (1500/4+Q) sample exhibited a bimodal dimple structure. The size of the “coarse dimples” was comparable to that of the pores shown in Fig. 4.6-2a. In Fig. 4.6-6b taken at a higher magnification, “fine dimples” between the “coarse dimples” were observed, and few TiC_x particles were found in the Ti-22Nb (1500/4+Q) sample. Fig. 4.6-6c shows the fracture surface of the Ti-22Nb (HIP+Q) sample. Besides, few TiC_x particles were also observed. The “fine dimples”

homogeneously distributed on the fracture surface with size less than $10\ \mu\text{m}$ as shown in Fig. 4.6-6d. The appearance of the fracture surface hints to a predominantly ductile fracture.

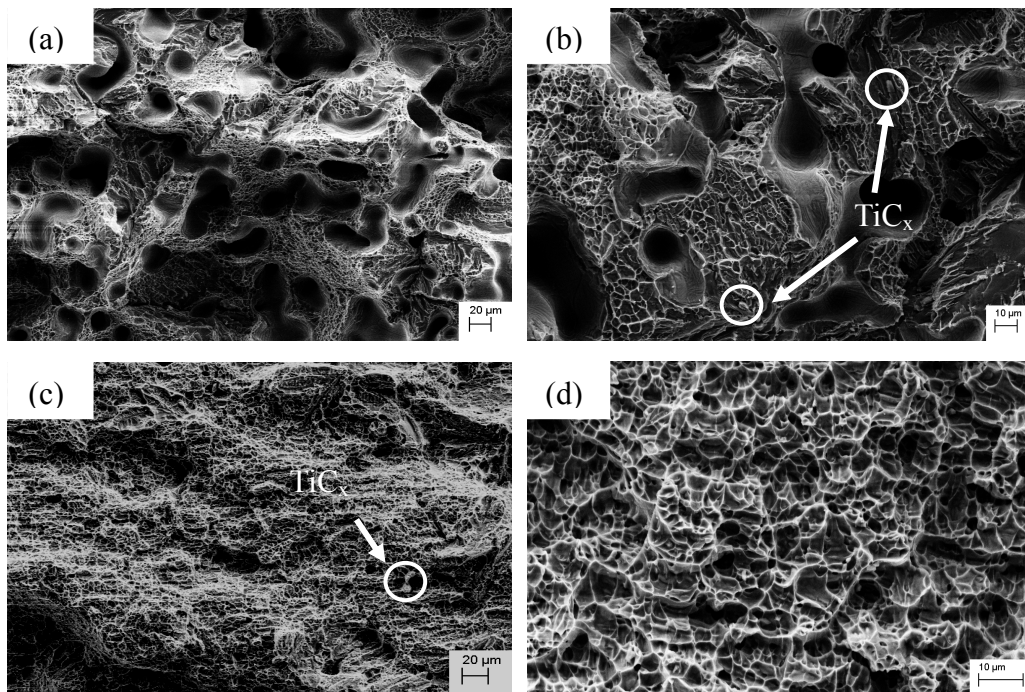


Fig. 4.6-6. The fracture surface of (a, b) Ti-22Nb (1500/4+Q), (c, d) Ti-22Nb (HIP+Q).

4.7 Cell biology assessments

4.7.1 Surface characterization

Before performing the cell adhesion experiments, a CLSM was employed for the topographical surface examinations and roughness measurements. Fig. 4.7-1 presents the 3-D topographic surface images of the BIO-samples – the CP-Ti (MIM-BIO), Ti-22Nb (MIM-BIO) and Ti-22Nb (AM-BIO) samples. The three configurations have different surface structures.

RESULTS

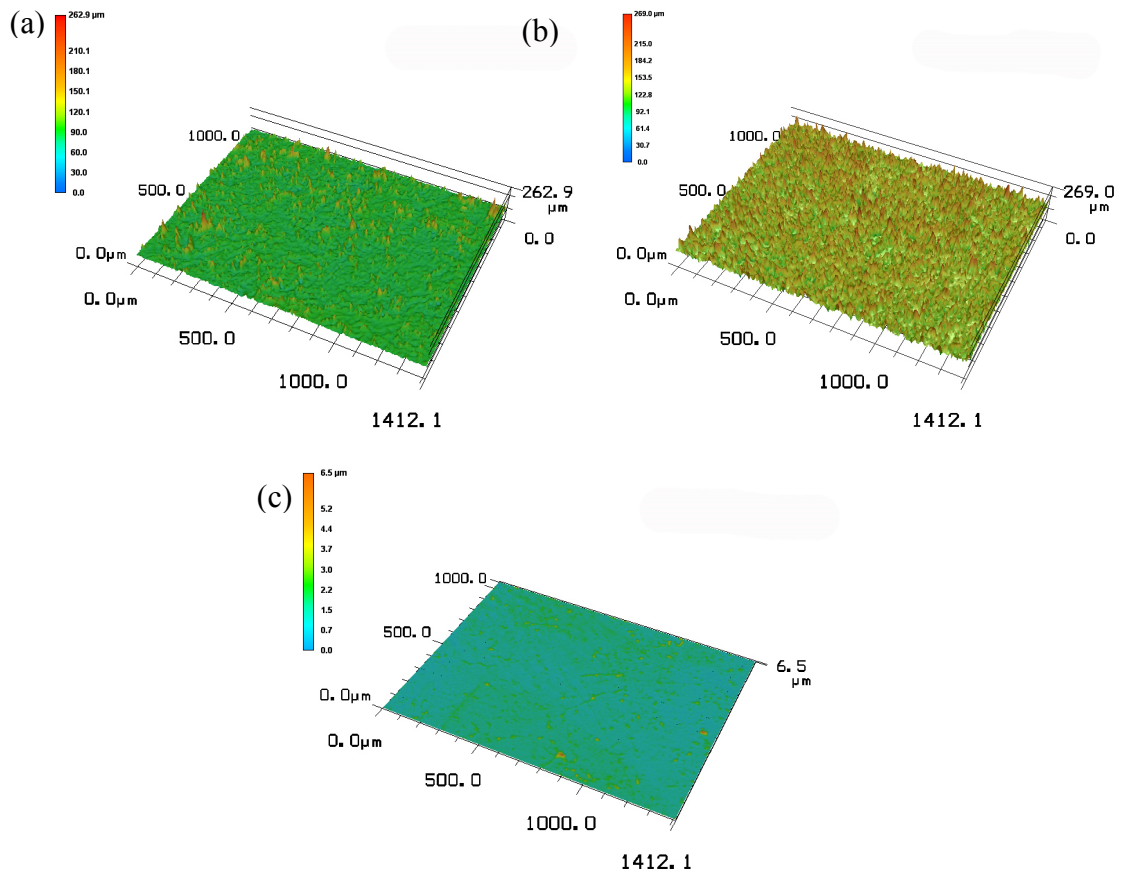


Fig. 4.7-1. Topographic 3-D views of the surfaces (1.41 mm × 1.00 mm) of (a) CP-Ti (MIM-BIO), (b) Ti-22Nb (MIM-BIO) and (c) Ti-22Nb (AM-BIO) samples. The color scale of each profile represents the height of peaks on the surface.

The Ti-22Nb (MIM-BIO) alloy showed higher and more irregular peak dimensions than the other two, whereas, the Ti-22Nb (AM-BIO) alloy exhibited the smoothest surface. Such diversity between them was confirmed by the comparative Ra (average surface roughness) and Rz (average maximum height of the profile) values as shown in Table 4.7-1. The Ti-22Nb (AM-BIO) alloy showed a maximum peak height of about 6.5 μm, however, the profiles of the CP-Ti (MIM-BIO) and Ti-22Nb (MIM-BIO) samples had amplitudes of around 263 μm and 269 μm, respectively.

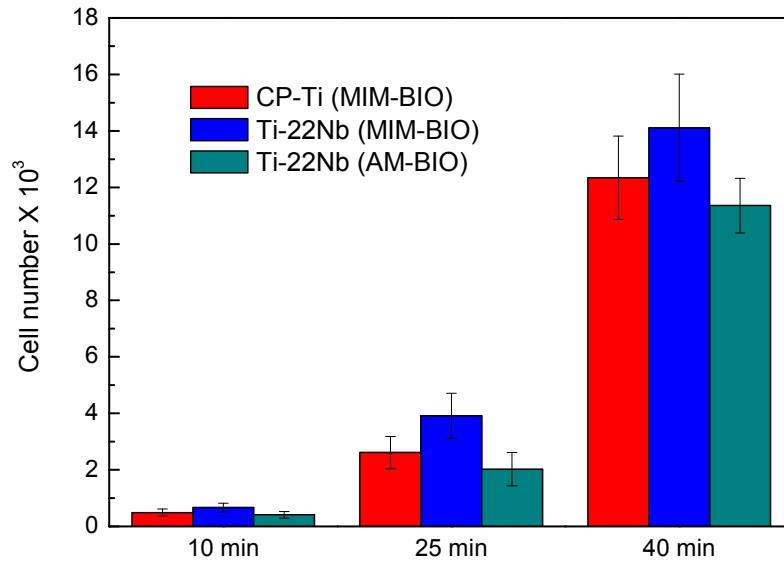
Table 4.7-1 Roughness parameters on the BIO-samples (μm)

	CP-Ti (MIM-BIO)	Ti-22Nb (MIM-BIO)	Ti-22Nb (AM-BIO)
Ra	6.30	15.26	0.30
Rz	262.89	268.96	6.48

4.7.2 Initial cell adhesion

Fig. 4.7-2a shows the cell number on the CP-Ti (MIM-BIO), Ti-22Nb (MIM-BIO) and Ti-22Nb (AM-BIO) samples after initial cell adhesion for 10, 25 and 40 min. Besides, in order to provide a better figure readability, statistical analyses are also presented in Fig. 4.7-2b. The SEM photos of the cells on different samples are presented in Fig. 4.7-3. A significantly enhanced adhesion of cells, i.e., a higher cell number, was observed in all the BIO-samples with longer incubation time. Furthermore, a slight preference of the cells on the materials with higher surface roughness was found. Especially, a significant difference between the cell numbers adhered on the Ti-22Nb (MIM-BIO) and Ti-22Nb (AM-BIO) samples incubated for 40 min could be noticed. Based on the SEM photos in Fig. 4.7-3, cells presented a homogeneous distribution throughout all material surfaces. However, different cell growth behaviors were observed on different samples with various incubation times. As shown in Fig. 4.7-3b, d and f, the HUCPV cells incubated for 10 min on the CP-Ti (MIM-BIO) and Ti-22Nb (MIM-BIO) samples appeared flat, especially around the pores, while, the ones on the Ti-22Nb (AM-BIO) samples were still round. Besides, with increasing incubation time, more HUCPV cells adhered on the surface of various samples was observed, and the cells tended to grow multilayered and cover the whole surface.

(a)



(b)

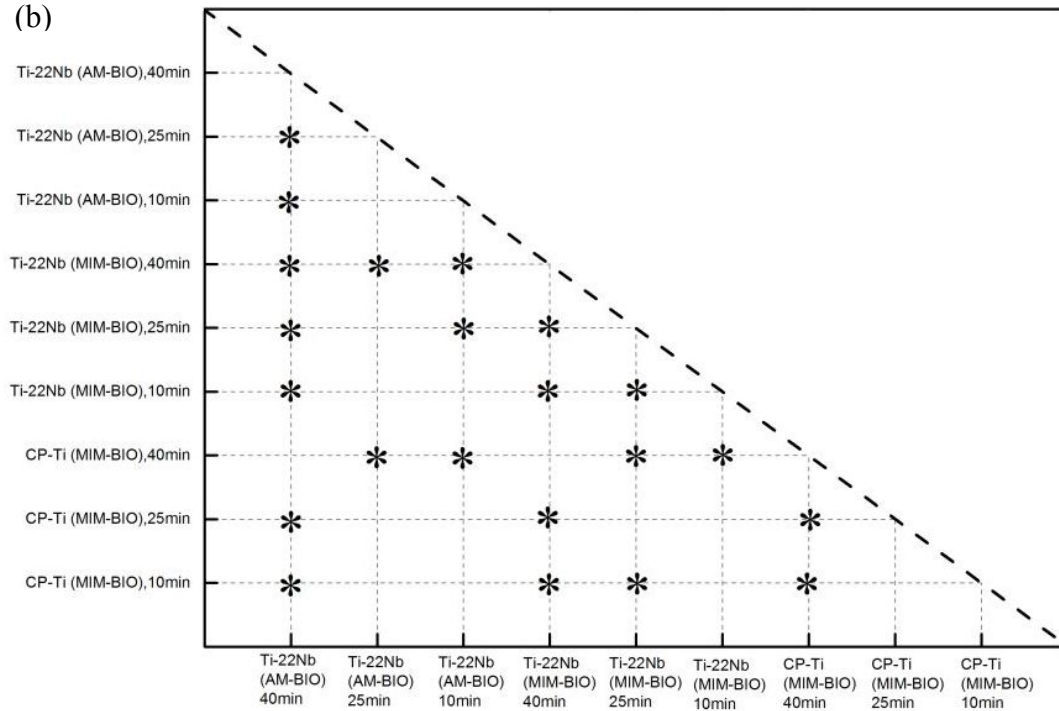
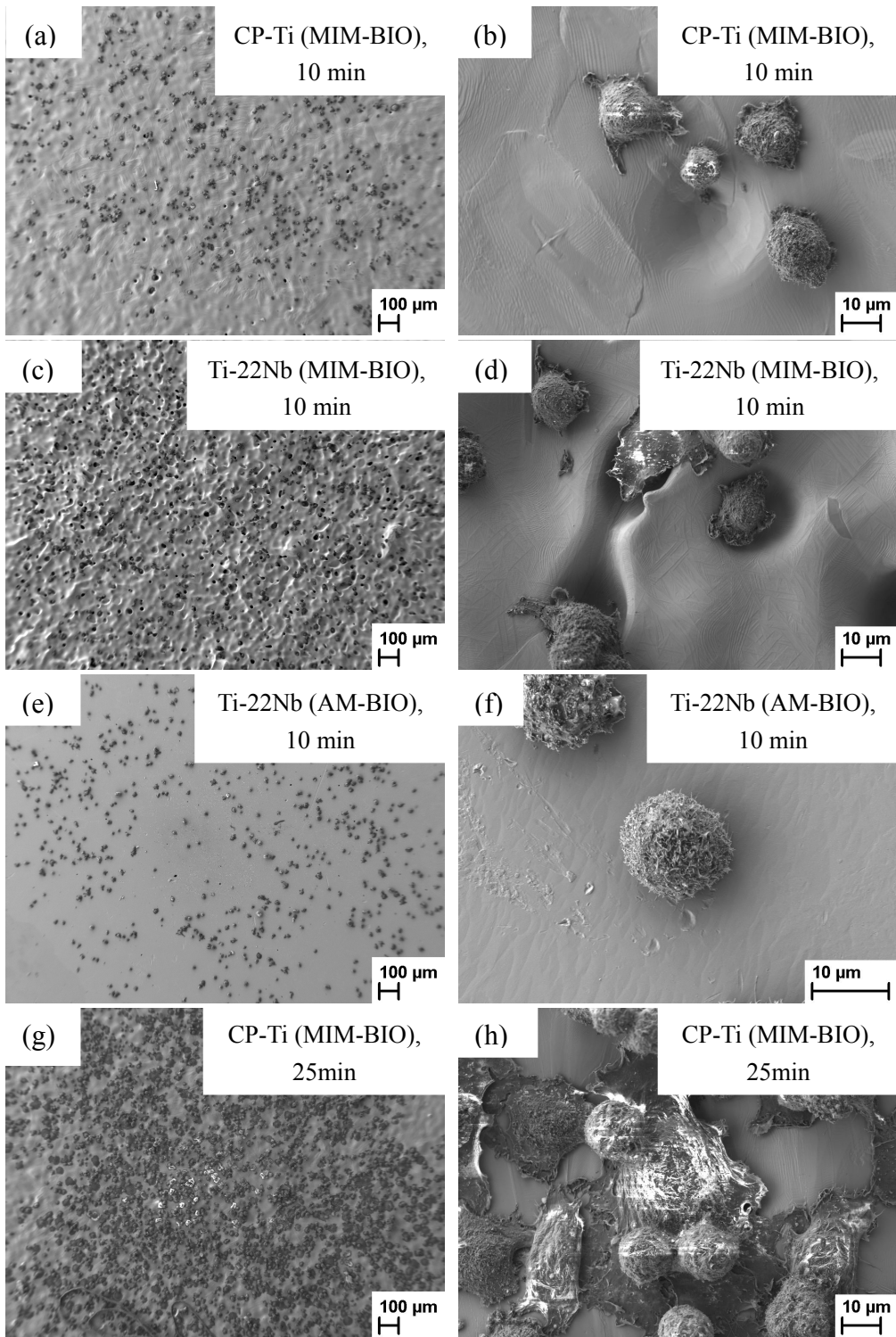
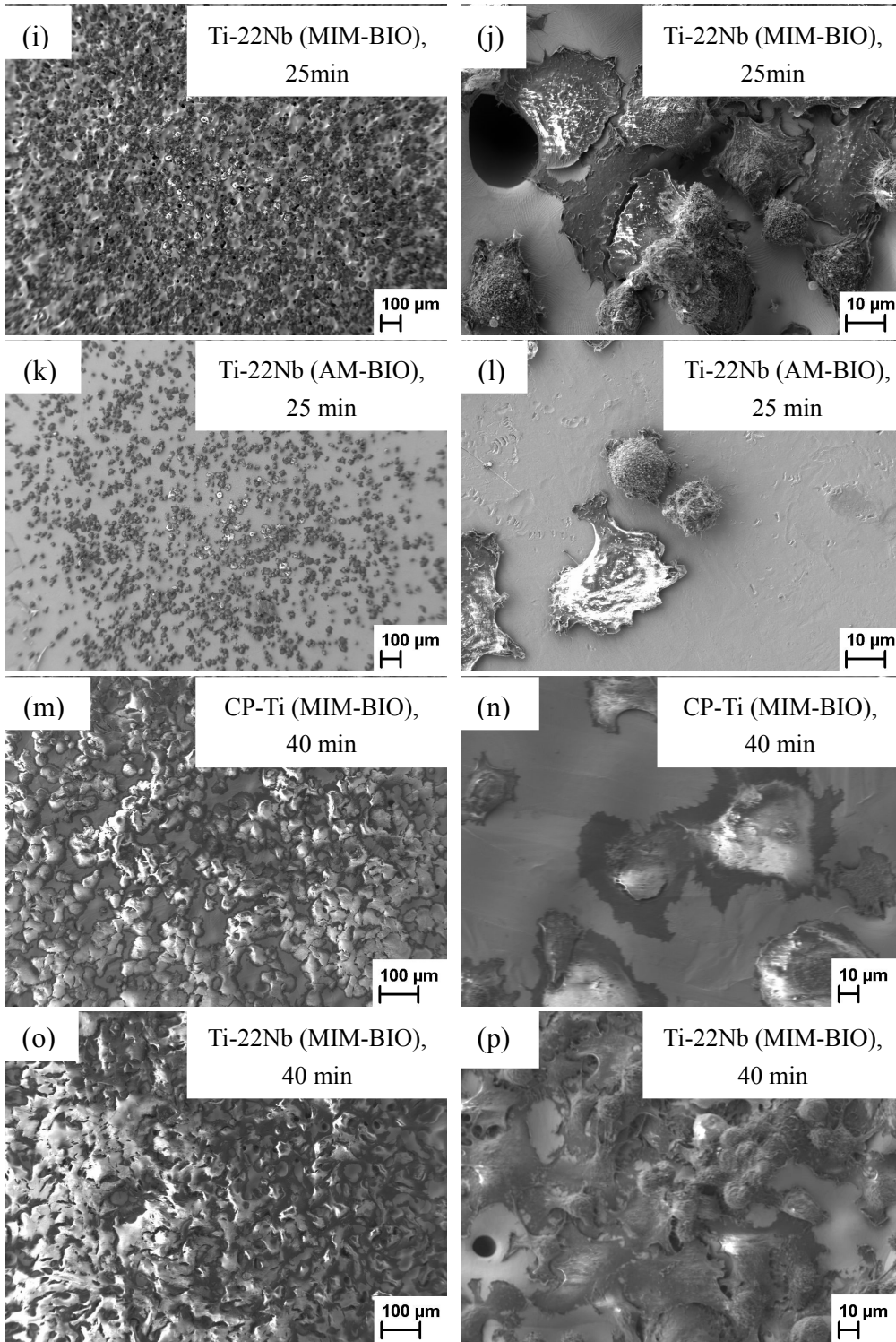


Fig. 4.7-2. (a) Cell number after adhesion on different materials for 10, 25 and 40 min.

(b) *Statistically significant difference ($P \leq 0.05$).



RESULTS



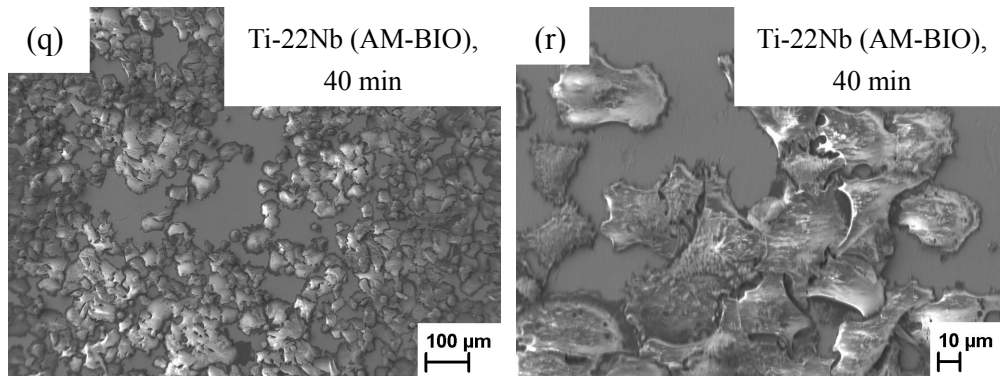


Fig. 4.7-3. SEM photos of HUCPV cells after adhesion on different materials for 10, 25 and 40 min.

4.7.3 Proliferation assays

The proliferation of HUCPV cells was studied after 3 and 5 days (MTT assays). Fig. 4.7-4 shows the results as well as the statistical analyses of the proliferation assays. The MTT absorbance of cells grown on the samples after 5 days is significantly higher than that obtained after 3 days for all the BIO-samples. Albeit the MTT absorbance of the cells on the Ti-22Nb (MIM-BIO) samples was slightly higher than the ones on the CP-Ti (MIM-BIO) and Ti-22Nb (AM-BIO) samples, no real great disparities were observed between the different samples.

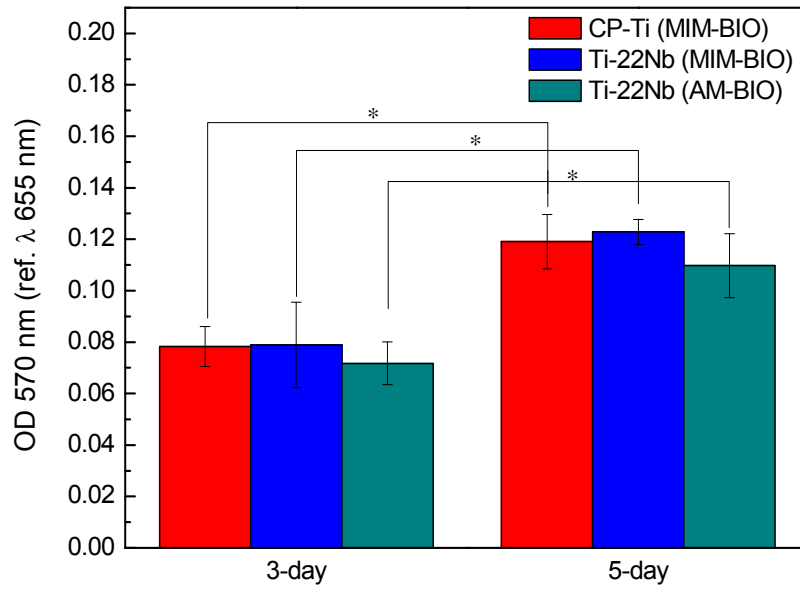


Fig. 4.7-4. MTT measurements of HUCPV cell proliferation assays after adhesion on various materials for 3 and 5 days.

*Statistically significant difference ($P \leq 0.05$).

5. Discussion

5.1 The sintering and homogenization behavior of MIM Ti-Nb alloys

The sintering and homogenization behavior of multicomponent systems have been extensively investigated [119-128]. As illustrated in Section 2.2.4, there are three models – one-phase, two-phase and three-phase binary systems describing the homogenization behavior of various binary powder mixtures during sintering. In this investigation, according to the Ti-Nb binary phase diagram [50] as presented in Fig. 2.1-1, the mixtures of Ti powder and Nb powder should be treated as one-phase binary systems above the β transus temperatures (790.7 °C for Ti-10Nb, 754.6 °C for Ti-16Nb and 721.5 °C for Ti-22Nb) during sintering.

In addition, as reported in literature [75, 129-134], the particle size distribution also has a significant influence on the densification during sintering. In the present work, the diameter of the Ti powder (< 45 μm) is much smaller than that of the HDH Nb powder (< 110 μm) as shown in Fig. 3.1-1a and b. Thus, the MIM Ti-Nb samples after debinding process can be viewed as bimodal powder mixtures. In the present investigation, the particle sizes of the Nb particles are much larger than those of the Ti particles. Moreover, the atomic fractions of Nb are only 5.4 %, 8.9 % and 12.7% in Ti-10Nb, Ti-16Nb and Ti-22Nb alloys, respectively. Thus, in these Ti-Nb alloys, the number density of Nb particles is much lower than that of the Ti particles. Consequently, after debinding, the Ti and Nb powder mixtures can be simplified as the structures – homogeneously dispersed coarse HDH Nb powder embedded in a network of fine Ti powder (see Fig. 4.2-2a).

The CP-Ti (DIL) and Ti-16Nb (DIL) samples show comparable starting temperatures

of the shrinkage as illustrated by Fig. 4.2-4. German [135] stated that the shrinkage of the powder compact results from the change in the interparticle spacing as neck growth takes place which is promoted by bulk transport processes. Consequently, the comparable starting temperatures of the shrinkage of both samples indicate that the neck growth almost took place simultaneously in both samples. According to Fig. 4.2-4, the S and SR of Ti-16Nb (DIL) at 700 °C are 0.18106 % and -0.00279 %/min, respectively, i.e., Ti-16Nb (DIL) is still at the very beginning stage of the sintering shrinkage at 700 °C. Thus, the Ti-16Nb (700/0.03) sample shows a microstructure representative of the initial stage of the sintering process as presented in Fig. 4.2-2a. The Ti-16Nb (DIL) sample exhibits two maximum linear shrinkage rates (SR) at around 940 °C and 1160 °C, respectively; whereas the only maximum SR of the CP-Ti (DIL) sample was observed at around 930 °C. During sintering, the intermediate stage determines the densification of the final compact and shows the highest shrinkage rate among the three stages of the sintering process. As illustrated in Fig. 4.2-2b and Fig. 4.2.2-a, the Ti-16Nb (1100/4) is composed of irregular Nb particles and a porous Ti matrix with a porosity of around 11 %, indicating that the sintering of the Ti-16Nb (1100/4) sample at 1100 °C is in the intermediate stage, and the pore elimination mainly takes place between Ti particles rather than between Ti and Nb particles. Consequently, it is reasonable to conclude that the maximum SR of both the CP-Ti (DIL) and Ti-16Nb (DIL) samples at around 930~940 °C indicates the climax of the intermediate stage of the sintering of Ti particles. At that low temperature, the isolated Nb particles in the Ti-16Nb (DIL) sample hardly contribute to the shrinkage; in contrast, they act as diffusion barriers constraining the shrinkage of the Ti particles in the Ti-16Nb (DIL) sample. Therefore, the maximum SR of the CP-Ti (DIL) sample at about 930 °C is about twice as much as that of the Ti-16Nb (DIL) sample at about 940 °C.

However, the CP-Ti (DIL) and Ti-16Nb (DIL) samples exhibit different sintering behavior when temperature further increases. The decreased SR above 928 °C of the

CP-Ti (DIL) sample suggests the intermediate sintering stage of the Ti particles has ended. The significantly reduced *SR* after 1295 °C is an indication of initiation of the final sintering stage. Further pore elimination in the Ti matrix is more difficult than in the intermediate stage. In contrast, the *SR* of the Ti-16Nb (DIL) sample reduces from 939 °C to 992 °C. With further temperature increase, the *SR* of the Ti-16Nb (DIL) sample increases again, indicating the initiation of apparent diffusion between the Ti matrix and Nb particles. The microstructural evidence of metallurgical bonding between the Nb particles and the matrix is observed in the Ti-16Nb (1100/4) sample as presented in Fig. 4.2-3a. Besides, the detected trace amount of β -phase (see Fig. 4.2-1) in the Ti-16Nb (1100/4) sample is also attributed to the diffusion between the Ti matrix and Nb particles. Cracks and distinct boundaries are still found between the Ti matrix and Nb particles, which may not be attributed to thermal expansion, because the coefficients of thermal expansion of Ti and Nb are very close [136, 137]. The continuous residual pores between Ti particles and Nb particles (e.g. Point *A* in Fig. 4.2-3a) would be eliminated at higher sintering temperatures. As shown in Fig. 4.2-3a, the presence of the crack in Point *D* is probably due to the unbalanced diffusion rate and concomitant formation of Kirkendall type pores. The diffusion coefficient of Nb in β -Ti is four to six orders of magnitude larger than that of Ti in Nb in the temperatures range between 900 °C and 1500 °C [138-142]. Thus, the mass flow between the two types of powder should be mainly from the Nb particles to the surrounding Ti matrix, which leads to pores initiation between the Nb particles and Ti matrix. Above 1156 °C, the *SR* of the Ti-16Nb (DIL) sample gradually decreases, suggesting the end of the intermediate sintering stage. As presented in Fig. 4.2-3, the Ti-16Nb (1300/4) exhibits a microstructure without visible Nb-rich regions, suggesting that the homogenization between the Ti matrix and Nb particles has finished at 1300 °C. As the temperature further increases, the pore elimination process should be only dependent on the diffusion in the Ti-Nb matrix instead of Ti or Nb particles.

Based on the discussion above, the sintering process of the Ti-Nb alloys can be divided into several steps as shown in Fig. 5.1-2:

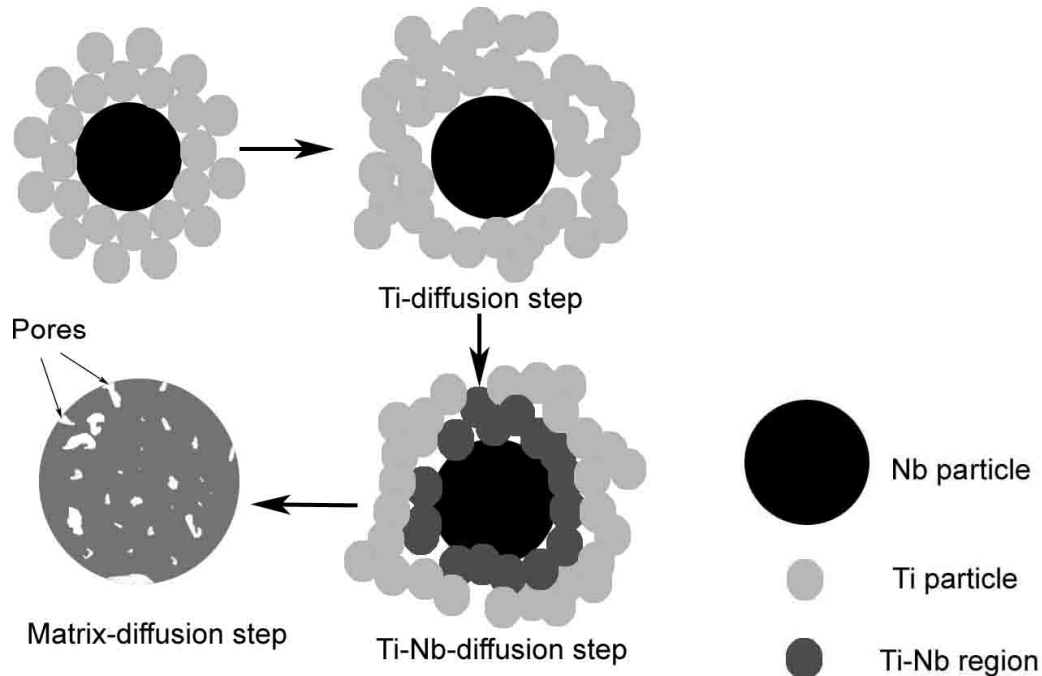


Fig. 5.1-2. Sketches of the densification behavior in the Ti-Nb bimodal particle mixture, showing the three steps during sintering of the Ti-Nb alloys. Pores are visible in all the steps.

- **Ti-diffusion step.** The sintering process starts mainly between the Ti particles at a relatively low temperature. In this step, the pore elimination is attributed to the diffusion between Ti particles instead of that between Ti and Nb particles, due to the significant difference between the diffusion coefficients of them. The bimodal Ti-Nb system can be treated as a metal-inclusion model. The Nb particles act as barriers against the mass flow of the Ti atoms. The shrinkage of the Ti particles is constrained by the full density Nb particle. This leads to a stress that reduces the shrinkage. This step consists of two stages: the initial sintering stage and intermediate stage of Ti particles. When the sintering of the Ti matrix has almost reached the end of the intermediate stage, the diffusion between the Ti matrix and Nb particles becomes notable.

- Ti-Nb-diffusion step. When the temperature increased to a certain range, at which the neck growth between the Ti particles and Nb particles becomes apparent, the homogenization process of the bimodal Ti-Nb mixtures started. At this time, the sintering between the Ti particles was at the intermediate stage. Thus, the shrinkage in this step should result from not only the diffusion between the Ti particles, but also the mass transfer between the Ti matrix and Nb particles. During this step, the diffusion between the Ti matrix and Nb particles is almost unidirectional from Nb to Ti, due to the significant difference between the diffusion coefficient of Nb atoms in β -Ti and Ti atoms in Nb. Such a strong Kirkendall effect may lead to cracks initiation at Ti-Nb boundaries. This step is composed of two sintering stages: the initial stage and intermediate stage between the Ti matrix and Nb particles.
- Matrix-diffusion step. When the homogenization process between the Ti matrix and Nb particles has finished at higher temperatures (e.g., 1300 °C for MIM Ti-16Nb), i.e., the Ti-Nb bimodal structure has transferred into the Ti-Nb matrix, further shrinkage would be achieved by the diffusion of the Ti-Nb matrix. Since no Nb particles or Ti particles have been observed in the Ti-Nb alloys sintered at the temperatures of 1300 °C, 1400 °C and 1500 °C, the sintering of all these alloys was performed in the matrix-diffusion step. It is well known that during sintering when porosity decreases to about 8 %, the cylindrical, interconnected pores will be unstable and tend to collapse into spherical, closed pores, indicating the end of the intermediate stage and the beginning of the final sintering stage [82, 92, 94, 143]. Since the porosity of these alloys was lower than or at least around 8~9 %, they are already at the end of the intermediate stage and the beginning of the final sintering stage of the Ti-Nb matrix after sintering at 1300 °C, 1400 °C and 1500 °C.

5.2 The influence of sintering parameters on porosity and Young's modulus of MIM CP-Ti and Ti-Nb alloys

A clear dependence of the porosity and Young's modulus on the sintering temperature and time has been observed for the CP-Ti and Ti-Nb binary alloys fabricated by MIM process sintered at various temperatures with different sintering times.

5.2.1 The influence of sintering parameters on porosity.

According to the definition proposed by Thümmeler et al. [144], sintering is the thermal treatment for bonding the particles into a coherent solid mass and eliminating pores. Hence, the most directly influenced property of the MIM sample by changing sintering parameters should be porosity. Moreover, porosity is one of the controlling characteristics of the sintered samples. It influences various material properties, especially the mechanical properties and biocompatibility. Since the impurity levels of all the as-sintered samples show comparable values, and the O_{eq} values of them are lower than the critical value as illustrated in Section 4.1, the influence of sintering parameters on the impurity levels will not be discussed.

A reduced porosity with increasing sintering temperature and time for every composition is observed as presented in Fig. 4.3-1. As stated in Section 2.2.4, the pore elimination is attributed to the bulk diffusion. Thus, the temperature – time curve of the sintering process should definitely have a significant influence on the densification according to Fick's law of diffusion. Since all the sintering processes in the present work applied the same thermal debinding, heating rate and cooling rate, they only differ from each other by the sintering temperature and time. With increasing sintering time at a given sintering temperature, the porosity is reduced; while, at a higher sintering temperature, the diffusion coefficient will increase exponentially according to Eq. 2.2-1. Thus, the change of sintering temperature

should have more significant influence on porosity than that of the sintering time. For instance, the porosity of Ti-16Nb (1400/4) is 6.19 %, and that of Ti-16Nb (1500/2) is 6.14 %, while, Ti-16Nb (1400/2) shows a porosity of 7.68%. The similar porosity of both Ti-16Nb (1400/4) and Ti-16Nb (1500/2) samples indicates that the increase of 100 % sintering time (from 2 h to 4 h) and the increase of 6.0 % sintering temperature (from 1673 K to 1773 K) have comparable effect on reducing porosity. In a word, a higher sintering temperature and longer sintering time always lead to a decrease of porosity for every composition in the present investigation, and the porosity is more sensitive to the sintering temperature than the sintering time.

5.2.2 The influence of porosity on elastic modulus of MIM CP-Ti and binary Ti-Nb alloys

As described in Fig. 4.3-5 and Fig. 4.4-5, the Young's modulus of the as-sintered and as-HIPed CP-Ti and Ti-Nb samples determined by the RUS technique showed a clear dependence on the porosity. In order to investigate the relationship between the Young's modulus and porosity, various mathematical theories have been considered.

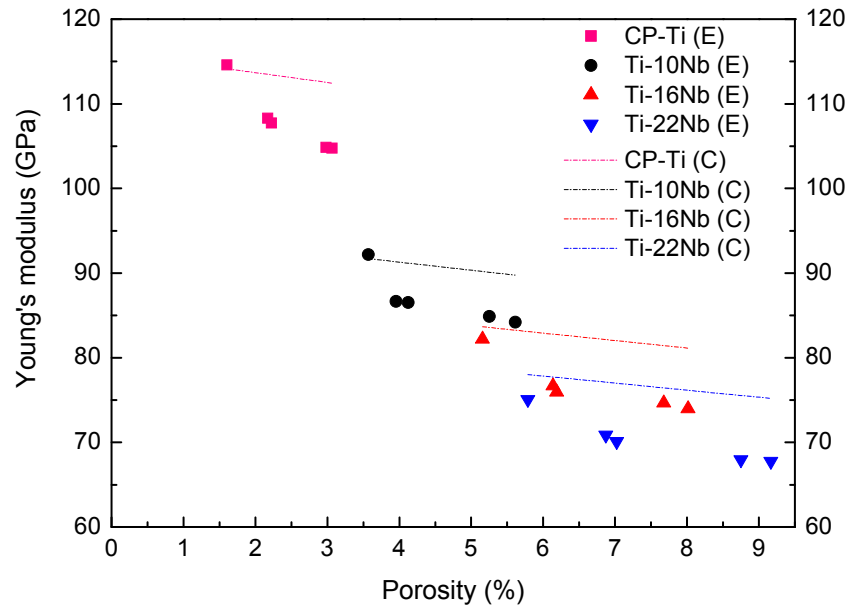


Fig. 5.2-1. Dependence of the Young's modulus of the as-sintered CP-Ti and Ti-Nb samples on porosity. Comparison of experimental Young's modulus (labeled as "composition (E)") and calculated Young's modulus (labeled as "composition (C)") based on Eq. 5.2-1. For each composition, the five points from left to right represent the samples with sintering parameters – 1500/4, 1500/2, 1400/4, 1400/2 and 1300/4, respectively.

Based on the assumption that the porous material consists of a void phase (with zero Young's modulus) and a solid matrix or skeleton phase (with Young's modulus equal to the dense material), Pabst et al. [145] adapted a simple relationship – Eq. 5.2-1 – to describe the dependence of Young's modulus E on porosity P :

$$E = E_0 (1 - P) \quad (5.2-1)$$

where E_0 is the Young's modulus of the full-dense material, which, in the present work, was taken as the Young's modulus of the corresponding as-HIPed sample. Fig. 5.2-1 presents the calculated Young's modulus of the as-sintered samples according to Eq. 5.2-1. Except for CP-Ti (1500/4) and Ti-Nb (1500/4) samples, the theoretical formula yield significantly higher values compared with the experimental results. Such a significant discrepancy probably results from the fact that Eq. 5.2-1 refers to the influence of porosity alone, disregarding the structure differences between sintered

and dense metals. Cobel and Kingery [146] pointed out that it is unwarranted to simply regard the as-sintered samples as such a mixture of voids and dense material, because the as-sintered samples usually exhibit heterogeneous structures, composed of packed grains and bridges of lower density between them, showing different modulus in different parts. That means the density distribution, pore shape and stress concentration near the pores are possible causes of the discrepancy [147]. Therefore, the good accordance between the experimental and calculated Young's modulus of CP-Ti (1500/4) and Ti-Nb (1500/4) samples should be attributed to the fact that these two specimen states already exhibit homogenous structures due to the long sintering time and especially the high sintering temperature. So their internal structure should be most closely reassemble the model proposed by Pabst et al. [145].

The case of heterogeneous structure of as-sintered samples with arbitrary pore shapes has been considered by Buch and Goldschmidt [148]. To obtain the Young's modulus from porosity, they proposed the following relationship:

$$E = E_0 \left[1 - \frac{15(1-\nu_0)P}{(7-5\nu_0) + 2P(4-5\nu_0)} \right] \quad (5.2-2)$$

where ν_0 is Poisson's ratio of the fully-dense samples. The Poisson's ratios of Ti and Ti-Nb based alloys were reported as approximately 0.3 [149, 150]. Thus, in the present case, Poisson's ratios of all the as-HIPed samples were assumed to be a constant, i.e., $\nu_0=0.3$. Fig. 5.2-2 compares experimental results with those obtained from Eq. 5.2-2. Albeit the calculated data of Young's modulus of the as-sintered CP-Ti samples differs slightly from the experimental results, the theoretical data showed excellent agreement with the experimental Young's modulus values of the as-sintered Ti-Nb samples with high porosity, suggesting that the exactness of Eq.5.2-4 is sufficient to predict the Young's modulus of the MIM Ti-Nb samples.

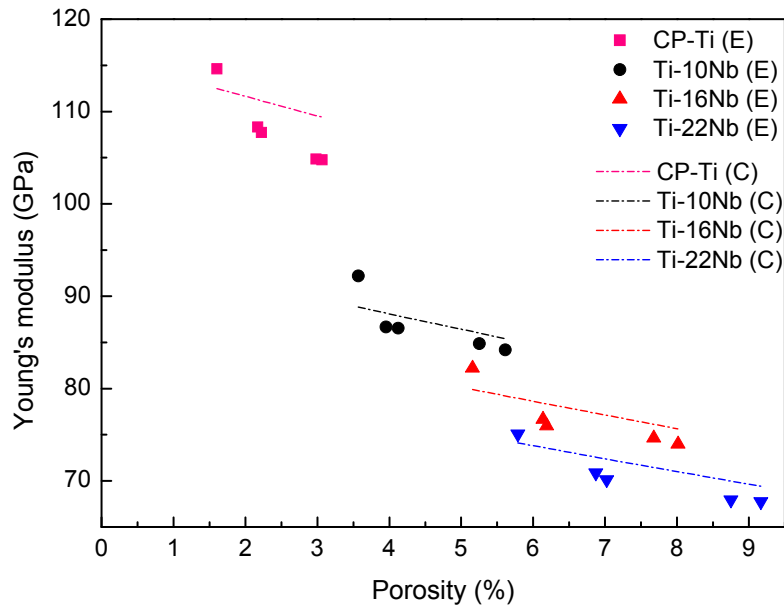


Fig. 5.2-2. Comparison of experimental and calculated data according to Eq. 5.2-2 for the as-sintered CP-Ti and Ti-Nb samples. The experimental and calculated results are labeled as “composition (E)” and “composition (C)”, respectively. For each composition, the five points from left to right represent the samples with sintering parameters – 1500/4, 1500/2, 1400/4, 1400/2 and 1300/4, respectively.

5.3 The influence of Nb content on microstructure and mechanical properties of MIM CP-Ti and Ti-Nb alloys

According to the Fig. 4.3-1, only the samples sintered at 1500 °C for 4h exhibit a porosity of less or at least around 5 %, which is commonly accepted as the limit between open and closed porosity [151]. Consequently, in this section, the discussion regarding the dependence of microstructure and mechanical properties of MIM CP-Ti and Ti-Nb alloys on Nb content mainly focus on the CP-Ti (1500/4) and Ti-Nb (1500/4) alloys. The CP-Ti (HIP) and Ti-Nb (HIP) alloys are also discussed for comparison.

5.3.1 The influence on α / β phase fraction

As revealed by the XRD results shown in Fig. 4.3-2, the CP-Ti (1500/4) and Ti-Nb

(1500/4) alloys consist of α -phase (CP-Ti (1500/4)) and α - and β -phase (Ti-Nb (1500/4)), respectively. With increasing Nb content, the intensity of the primary α peak decreases gradually, indicating that the proportion of α -phase declines as the Nb content increases. Such a dependence of α -phase fraction on Nb content should be attributable to the β -stabilizing effect of Nb on Ti alloys. Nb addition has a marked effect in lowering the β transus temperature of Ti alloys [152-154]. As shown in Fig. 2.1-1, the Ti-Nb binary phase diagram reveals that as the Nb content increases from 10 wt.% over 16 wt.% to 22 wt.%, the β transus temperature decreases from 790.7 °C over 754.6 °C to 721.5 °C, respectively. Whereas, the β transus temperature of pure Ti is 882 °C [35]. The lowered β transus temperature inevitably leads to a higher fraction of β -phase.

5.3.2 The influence on porosity

As presented in Fig. 4.3-1, the porosity increases from about 1.6 % for CP-Ti (1500/4) to around 5.7 % for Ti-22Nb (1500/4). Since the binder volume fractions in the CP-Ti and Ti-Nb samples after metal injection moulding are all 31 vol.%, all these samples should exhibit similar porosity after the debinding process. For the CP-Ti (1500/4), both the fine particle size and high diffusion coefficient contribute to the densification, thus, it is reasonable that CP-Ti (1500/4) exhibit much lower porosity than the Ti-Nb (1500/4) alloys. For the Ti-Nb (1500/4) alloys, the dependence of porosity on Nb content can be illustrated according to the bimodal Ti-Nb powder mixture model and the corresponding sintering behavior discussed in section 5.1. During the Ti-diffusion sintering step, the densification is mainly controlled by the mass transport between the Ti particles. Since the Ti particles during sintering are lying beneath each other, the undissolved Nb particles hinder the shrinkage, i.e., they act as diffusion barriers. Thus, at the end of this step, the Ti-22Nb (1500/4) sample should exhibit the highest porosity, due to its higher Nb powder fraction compared with CP-Ti (1500/4), Ti-10Nb (1500/4) and Ti-16Nb (1500/4) alloys. With increasing temperature, in the

Ti-Nb-diffusion step, the pore elimination results from both Ti-Ti diffusion and Ti-Nb diffusion. In the Ti-Nb binary system, the diffusion coefficients of both Ti and Nb in the alloy fall dramatically with increasing Nb content [138, 152]. Therefore, samples with higher Nb content should show a lower densification rate in this step. At the sintering temperature – 1500 °C, the Ti-Nb alloys should be in the Matrix-diffusion step and become solid solutions. Further pore elimination is controlled by the diffusion in the Ti-Nb matrix. Thus, lower Nb content also leads to a higher relative density. In summary, a higher Nb content resulted in reduced densification rates in all the three steps of the sintering process.

5.3.3 The influence on mechanical properties and fractography

As shown in Fig. 4.3-6, there is an obvious relationship between Nb content and mechanical properties of the CP-Ti (1500/4) and Ti-Nb (1500/4) alloys. The CP-Ti (1500/4) and Ti-Nb (1500/4) samples present different fracture behaviours as shown in Fig. 4.3-7. The honeycomb structure of the fracture surface of the CP-Ti (1500/4) is a typical feature of a ductile failure, which means that the Ti powder bonding was metallurgically sound. The fracture surfaces of the Ti-Nb (1500/4) exhibit bimodal structures. The “coarse dimples” have similar sizes as the pores in the Ti-Nb (1500/4) alloys, but they are not observed on the fracture surfaces of the Ti-Nb (HIP) alloys (see Fig. 4.4-4). Consequently, such “coarse dimples” should correlate with the pores in the Ti-Nb (1500/4) alloys. The formation of “fine dimples” indicates the ductile deformation of the material between the pores. The presence of TiC_x particles on the fracture surfaces may lead to the low ductility of the Ti-Nb (1500/4) samples, which is confirmed by the observation of cracks cutting through TiC_x particles (Fig. 4.3-8).

The effect of Nb addition in Ti alloys on Young’s modulus has been extensively reported [31, 53, 155, 156]. As discussed in section 5.3.1, Nb has a strong β -stabilizing effect on Ti alloys. So the decrease of Young’s modulus with a higher

amount of Nb addition in the as-HIPed alloys is expected.

A strength-enhancement effect of Nb in Ti alloys has been reported in previous works [54, 157]. From an investigation which analyzed the influence of Nb addition on the tensile strength and elongation of arc-melted Ti-Nb binary alloys [25], it is known that the tensile strength slightly increases from around 700 MPa to 750 MPa with Nb content increasing from 14 wt.% to 22 wt.%, but the elongation decreases from around 11 % to 9 %. However, in the present work, the differences in both tensile strength and elongation between the Ti-Nb (1500/4) binary alloys were much larger. This suggests that the mechanical properties of the Ti-Nb (1500/4) binary alloys have not been affected by the presence of Nb alone but by additional factors.

Besides the influence of the Nb content, porosity has also played an appreciable role in determining the Young's modulus of the as-sintered samples. That higher porosity results in reduced Young's modulus has already been discussed in Section 5.2.2. As a result, even though the Ti-10Nb (1500/4), Ti-16Nb (1500/4) and Ti-22Nb (1500/4) alloys are $\alpha+\beta$ alloys, the specimens investigated here could exhibit a comparable or even lower Young's modulus than some β -Ti alloys, such as Ti-12Mo-6Zr-2Fe and Ti-13Nb-13Zr with lower porosity [2]. Under monotonic tensile loading, the pores reduce the effective cross-section for load bearing and act as stress concentration sites, leading to strength and ductility decrease [151]. The CP-Ti (1500/4) samples exhibit higher tensile strength than the CP-Ti samples produced by Sidambe et al. [16] showing comparable O_{eq} as the former. Such a difference should result from the lower porosity of the CP-Ti (1500/4) samples. The negative effect of porosity on tensile strength explains the lower tensile strength of the CP-Ti (1500/4) and Ti-Nb (1500/4) samples compared to the CP-Ti (HIP) and Ti-Nb (HIP) samples. The elongation of the CP-Ti (HIP) exhibits an 40 % increase compared to the CP-Ti (1500/4), which is in basic agreement with Bourcier et al. [158] that even a porosity less than 5 % in CP-Ti can lead to a significant decrease of ductility. However, there is almost no influence of

porosity on the ductility of the Ti-16Nb (1500/4) and Ti-22Nb (1500/4) samples, because they show comparable low elongation as the Ti-16Nb (HIP) and Ti-22Nb (HIP) samples. The reason lies probably in the deterioration of the ductility caused by the TiC_x precipitates, being stronger than the effect of porosity.

It has been shown that TiC_x particles can increase the strength of Ti and its alloys through precipitation strengthening [103, 105, 106, 159, 160]. In the present investigation, the yield strength increased by 10.19 % from Ti-16Nb (1500/4) with a carbide area fraction of around 0.92 % to Ti-22Nb (1500/4) with a carbide area fraction of about 1.81 %, while, the increase of yield strength from the arc-melted Ti-16Nb to arc-melted Ti-22Nb without TiC_x particles was only 6.06 % [25]. Such a different behaviour suggests that the TiC_x particles make a significant contribution to the tensile strength of the Ti-Nb (1500/4) alloys. In addition, it should be noted that the tensile strength of the Ti-22Nb (1500/4) is close to that of the arc-melted Ti-22Nb [25], although the former has a higher degree of porosity, indicating that the positive contribution of the TiC_x precipitation has compensated for the negative influence of the porosity. The influence of TiC_x particles on Young's modulus is not clear yet and will be addressed in further investigation.

In both Ti-Nb (1500/4) and Ti-Nb (HIP) alloys, TiC_x particles are readily visible on the fracture surfaces as presented in Fig. 4.3-7 and Fig. 4.4-4. Cracks are found to cut through the TiC_x particles, showing the brittle nature of TiC_x . On grain boundary triple points, TiC_x particles are observed lying on the fracture path along the grain boundaries, indicating that the TiC_x precipitates are the easy spots and paths for crack initiation and propagation. Such behaviour has also been reported in TiC-reinforced Ti-based composites [107, 161]. As shown in Fig. 4.3-8, in the Ti-16Nb (1500/4) and Ti-22Nb (1500/4) alloys, crack initiation and propagation are observed around the TiC_x particles on the longitudinal sections of the fractured Ti-16Nb (1500/4) and Ti-22Nb (1500/4) tensile specimens, indicating the negative effect of the TiC_x

precipitates on fracture resistance. In summary, the poor ductility of Ti-16Nb (1500/4), Ti-22Nb (1500/4), Ti-16Nb (HIP) and Ti-22Nb (HIP) is thus attributed to the large amount of carbides.

The poor ductility is definitely a drawback of MIM Ti-Nb alloys investigated here for biomedical applications. Therefore, methods to control the TiC_x precipitation in the MIM Ti-Nb alloys were investigated. A combination of annealing and subsequent quenching was applied in order to dissolve the TiC_x particles into the matrix.

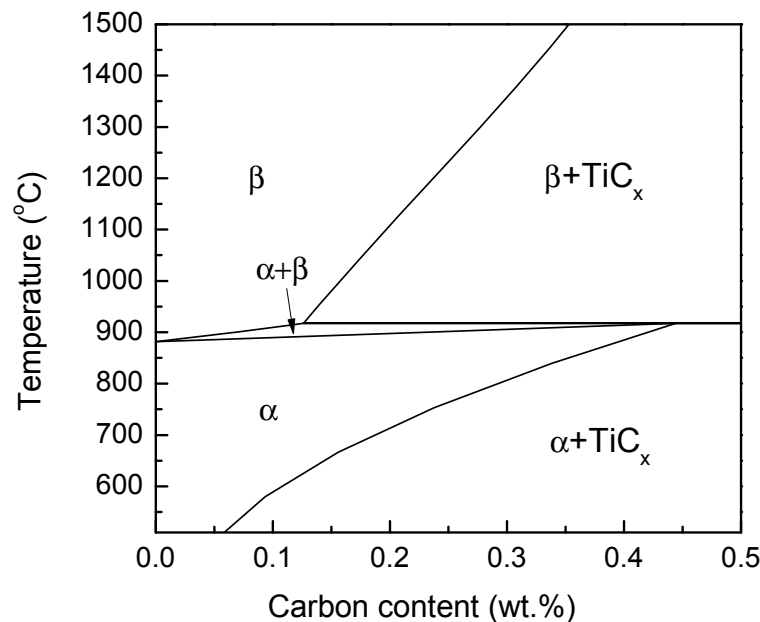


Fig. 5.3-1. The calculated binary phase diagram of Ti-C according to the thermodynamic data of Frisk [162].

The solubility of carbon in α -Ti and β -Ti could be predicted with the underlying CALPHAD (CALculation of PHase Diagram) approach. The thermodynamic parameters of the C-Ti system reported by Frisk [162] were applied for the calculation. The calculation was conducted as part of a cooperation by Dr. Keke Chang in RWTH Aachen University.

The calculated Ti-C binary phase diagram is presented in Fig. 5.3-1. There is a

maximum of the carbon solubility of 0.44 % at 917.8 °C in the α -phase, and another maximum of carbon solubility of 0.40 % at 913.9 °C in $\alpha+\beta$ field. Therefore, a dissolution of the TiC_x particles into the matrix at one of the temperatures with the maximum carbon solubility should be possible in the binary Ti-C system. The Ti-22Nb (1500/4) and Ti-22Nb (HIP) samples were annealed and quenched. The reasons for the choice of the specific temperatures and times of the annealing and quenching process will be discussed in Section 5.4.1. As presented in Fig. 4.6-2 and Fig. 4.6-3, the amount of TiC_x particles is significantly reduced after annealing and quenching. Consequently, the annealing and quenching process is effective to minimize the TiC_x precipitation in MIM Ti-Nb alloys. The α'' martensite is found after quenching as shown in Fig. 4.6-1. It has been reported that rapid cooling from high temperatures leads to α'' martensite forming in Ti-Nb alloys with a Nb content higher than 10.5 wt.% [163, 164]. The α'' martensite is transformed from the β -phase [165-167]. The presence of α'' martensite usually exhibits deleterious effects on the tensile strengths of Ti-Nb-based alloys [168, 169], since martensite reorientation occurs at low stress levels due to the internal stress concentrations [170]. Thus, it is probable that the α'' martensite formation plays role in lowering the tensile strength of the Ti-22Nb (1500/4+Q) and Ti-22Nb (HIP+Q) samples compared with that of the Ti-22Nb (1500/4) and Ti-22Nb (HIP) samples as plotted in Fig. 4.6-5. This effect cannot clearly be distinguished from the effect of the reduced amount of TiC_x particles after quenching which should also contribute to a decrease in tensile strength. It is important to note that the as quenched samples still exhibit much higher strength than that of human bones (18~80 MPa) [171, 172]. So they are still promising candidates as implant materials from the strength point of view.

Although the as-quenched samples show lower tensile strength than the Ti-22Nb (1500/4) and Ti-22Nb (HIP) samples, the elongation has been significantly improved after annealing and quenching. α'' martensite sometimes results in slightly higher elongation [49], and the lower amount of TiC_x particles also contributes to the

remarkable ductility-enhancement. The predominantly ductile fracture surfaces of the Ti-22Nb (1500/4+Q) and Ti-22Nb (HIP+Q) samples indicate that such low amounts of TiC_x particles cannot lead to rapid crack propagation in the ductile Ti-Nb matrix.

Consequently, such an annealing and quenching process has been proved to be an efficient way to reduce the amount of TiC_x precipitates, leading to a significant increase on ductility.

5.4 The TiC_x precipitation in MIM Ti-Nb alloys

It is well known that both Ti and Nb show strong carbide forming effects [173, 174]. However, the carbide particles in the MIM Ti-Nb samples are found to be TiC_x instead of NbC_x (see Table 4.3-2). TiC_x exhibit formation energies ranging from -150 to -195 kJ/mol [175], whereas, the formation energy of NbC_x is only -70 to -100 kJ/mol [176-179]. Such a difference in the formation energy of TiC_x and NbC_x explains that the former is more stable, leading to the preferentially precipitation of TiC_x particles in the MIM Ti-Nb alloys.

TiC_x in Ti, Ti alloys and Ti matrix composites (TMCs) has been extensively investigated, owing to its strong effects of precipitation hardening [103, 104, 106, 108] as well as oxygen getter [105]. In most cases, TiC_x particles were either directly introduced into the Ti-based alloys and composites using powder metallurgy [107], or indirectly formed by reactions between Ti and carbon or carbon-rich compounds, such as graphite [117, 180], diamond [181] and carbonyl iron powders [182]. In MIM Ti alloys, the carbon content of the final products is influenced by several factors, such as residual binder, impurity levels of powders and parameters of debinding and sintering processes. For instance, the TiC_x precipitation in the Ti-12Mo alloy produced by powder injection moulding is attributed to the extremely high carbon content (>0.3 wt.%) in the alloy, resulting from the residual binder [160].

In the present investigation, all the pre-sintered, as-sintered, as-HIPed and as-quenched samples show comparable carbon levels (see Fig. 4.1-1), which are found to be lower than the carbon solubility in α -Ti and β -Ti according to the Ti-C binary phase diagram as shown in Fig. 5.3-1. However, as presented in Fig. 4.3-3, Fig. 4.3-4, Fig. 4.4-2 and Fig. 4.6-2, the TiC_x precipitates are observed in all the as-sintered, as-HIPed and as-quenched Ti-Nb alloys, but not in the as-sintered and as-HIPed CP-Ti specimens. Such a difference between the MIM Ti-Nb samples and MIM CP-Ti samples leads to the assumption that the Nb content is probably responsible for the unexpected precipitation of TiC_x particles.

In order to investigate the relationship between Nb content and the precipitation of the carbide particles, the pseudo-binary Ti-C phase diagrams of Ti-10Nb-C, Ti-16Nb-C and Ti-22Nb-C have been calculated using the Thermo-Calc software as shown in Fig. 5.4-1. The solubility of carbon in both α -phase and β -phase could be predicted with the underlying CALPHAD (CALculation of PHase Diagram) approach. The thermodynamic parameters of the C-Nb-Ti system reported by Lee et al. [183] were applied for the calculation. These calculations were also performed by our cooperator – Dr. Keke Chang in RWTH Aachen University [184].

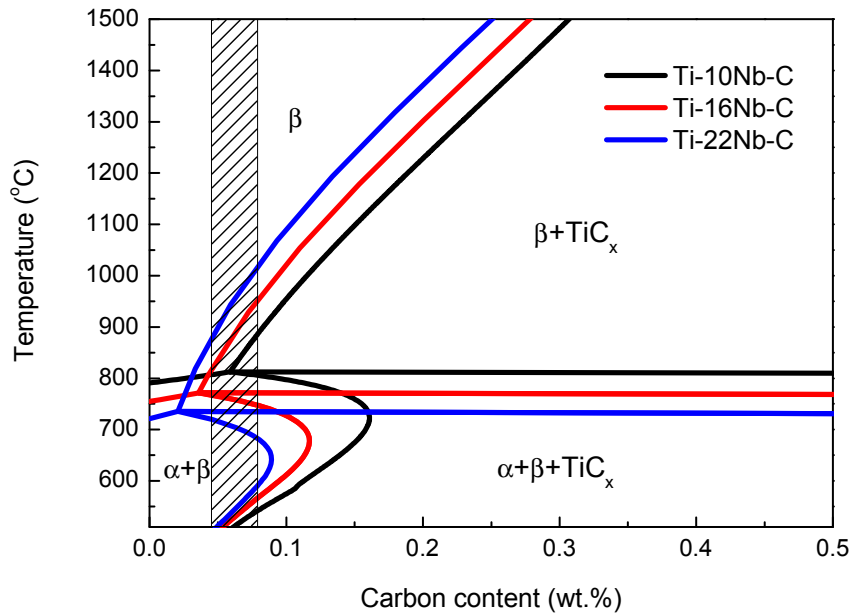


Fig. 5.4-1. The pseudo binary Ti-C phase diagrams of Ti-10Nb-C, Ti-16Nb-C and Ti-22Nb-C predicted using Thermo-Calc software. The shadow area shows the carbon contents of all the MIM samples in the present investigation.

After comparing the Ti-C binary phase diagram (see Fig. 5.3-1) with the pseudo-binary phase diagrams, an obvious decrease of carbon solubility with increasing Nb content is found. Consequently, considering that the carbon contents of all the as-sintered, as-HIPed and as-quenched samples are ranging between 0.05 wt.% and 0.07 wt.%, it is reasonable that the TiC_x precipitates are formed in the MIM Ti-Nb samples.

As discussed in Section 5.1, the diffusion between Ti and Nb particles in MIM Ti-Nb samples is not apparent until the Ti-Nb-diffusion step at relative high temperature. The diffusion coefficients of carbon in both α -Ti and β -Ti [185] are significantly higher than that in Nb [186]. Thus, the non-presence of TiC_x particles in the pre-sintered Ti-16Nb (700/0.03) and Ti-16Nb (1100/4) samples should be attributed to the fact that before forming Ti-Nb matrix at elevated temperature, the carbon atoms mainly dissolve in the Ti matrix. At higher temperatures, the diffusion from Nb

particles into the Ti matrix leads to the formation of a Ti-Nb matrix. According to the pseudo binary phase diagrams of Ti-10Nb-C, Ti-16Nb-C and Ti-22Nb-C in Fig. 5.4-1, the carbon solubilities in the matrix of Ti-10Nb, Ti-16Nb and Ti-22Nb are always higher than the carbon contents of the samples at the sintering temperatures – 1300 °C, 1400 °C and 1500 °C. Therefore, the TiC_x particles only precipitated during the cooling step, and thus did not influence the homogenization and sintering behavior at the heating and holding steps.

According to the pseudo-binary phase diagrams, the precipitation mechanism of TiC_x particles can be illustrated. For instance, in the Ti-10Nb (1500/4), Ti-16Nb (1500/4) and Ti-22Nb (1500/4) samples, at the sintering temperature of 1500 °C, the carbon solubility levels in the Ti-Nb matrix are 0.307 wt.%, 0.278 wt.% and 0.251 wt.%, respectively. Since the total carbon contents in these Ti-Nb (1500/4) binary alloys were about 0.05~0.07 wt.%, after sintering at 1500 °C for 4 h, all the carbon should be in solid solution as interstitial atoms and thus no titanium carbides should form. During the cooling step, with decreasing temperature, the solubility of carbon in Ti-10Nb and Ti-22Nb decreases, reaching a minimum of 0.051 wt.% at 812 °C for Ti-10Nb, 0.036 wt.% at 718 °C for Ti-16Nb and 0.021 wt.% at 735 °C for Ti-22Nb. At lower temperatures, the solubility of carbon increases to 0.161 wt.% at 723 °C for Ti-10Nb, 0.117 wt.% at 678 °C for Ti-16Nb and 0.089 wt.% at 641 °C for Ti-22Nb. However, as the temperature further decreases, the solubility of carbon decreases with decreasing temperature. Thus, the precipitation of carbides would start below 1000 °C in all the as-sintered, as-HIPed and as-quenched samples and no grain growth inhibition effect by titanium carbides in the Ti-Nb (1500/4) alloys can be expected, resulting in grain sizes greater than 100 μm for all (see Table 4.3-1).

In order to verify the calculated pseudo binary phase diagrams, in situ synchrotron HEXRD experiments have been performed. The applied temperature cycle is illustrated in Fig. 5.4-2 showing the two holding temperatures in the pseudo-binary

Ti-22Nb-C phase diagram. At the first holding temperature – 1100 °C, the carbon solubility in the matrix is approximately 1.0 wt.%, thus the carbides should fully dissolve at that temperature. While, the second holding temperature – 641 °C is the maximum point of carbon solubility in the lower temperature range in the $\alpha+\beta$ phase field with 0.089 wt.%. Consequently, if the calculated pseudo-binary Ti-22Nb-C phase diagram is reasonable, the carbide should fully dissolve at 1100 °C, and then precipitate during first cooling step. At the holding temperature of 641 °C, a re-dissolution of carbides should be observed. At the end of the subsequent second cooling step, the amount of carbides should be the same as the amount at the beginning of the experiment.

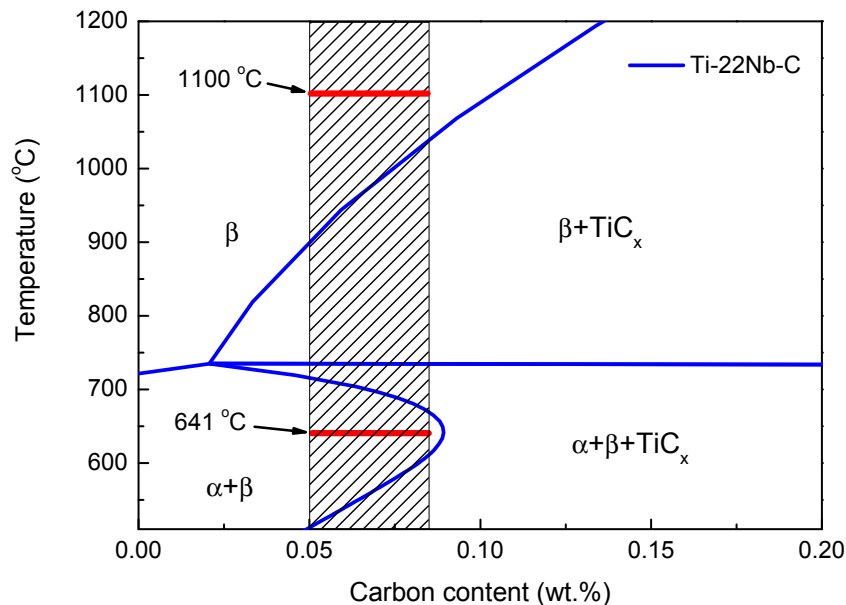


Fig. 5.4-2. The pseudo-binary Ti-22Nb-C phase diagram showing the two holding temperatures – 1100 °C and 641 °C – in the in situ HEXRD experiment. The shadow area shows the carbon contents of all the MIM samples in the present investigation.

From the in situ HEXRD one can not only determine the presence of different phases but also the time evolution of the intensities of a particular phase. The intensity of reflections is related to the volume fraction of the phases [187]. Fig. 5.4-3 shows the time evolution of relative intensities of X-ray reflections of the TiC_x phase in the Ti-22Nb (1500/4) alloy during the whole temperature cycle. According to Fig. 4.5-4,

the relative intensities of TiC_x reflections at Point X – RI_X – are calculated by using:

$$RI_X = \frac{I_X}{I_A} \times 100\% \quad (5.4-1)$$

where I_X is the TiC_x reflection intensity at Point X and I_A is the TiC_x reflection intensity at the initial point – Point A .

As shown in Fig. 5.4-3, during the heating step (from Point A to Point E), the relative intensities of the TiC_x reflections rapidly decrease from 100% to 0, indicating the fast dissolution of TiC_x particles. At 1100 °C, the relative intensities of the TiC_x reflections were always zero, suggesting that all the TiC_x particles had dissolved into the matrix. During the first cooling step from Point G to Point H , the relative intensities of the TiC_x reflections increased with decreasing temperature, showing the initial precipitation of TiC_x particles. From Point H to Point I the increase of the relative intensities of TiC_x reflections is slower probably caused by the beginning of the dissolution of TiC_x particles as predicted by the pseudo-binary Ti-22Nb-C phase diagram. During the annealing at 641 °C (from Point I to Point M), the relative intensities of the TiC_x reflections decrease from about 80% to 60%, which is an indication of the dissolution of TiC_x particles. At the final cooling step (from Point M to Point O), the relative intensities of TiC_x reflections gradually increase again to almost 100%, suggesting that the amount of carbide at the final point – Point O is almost the same as that at the initial point – Point A .

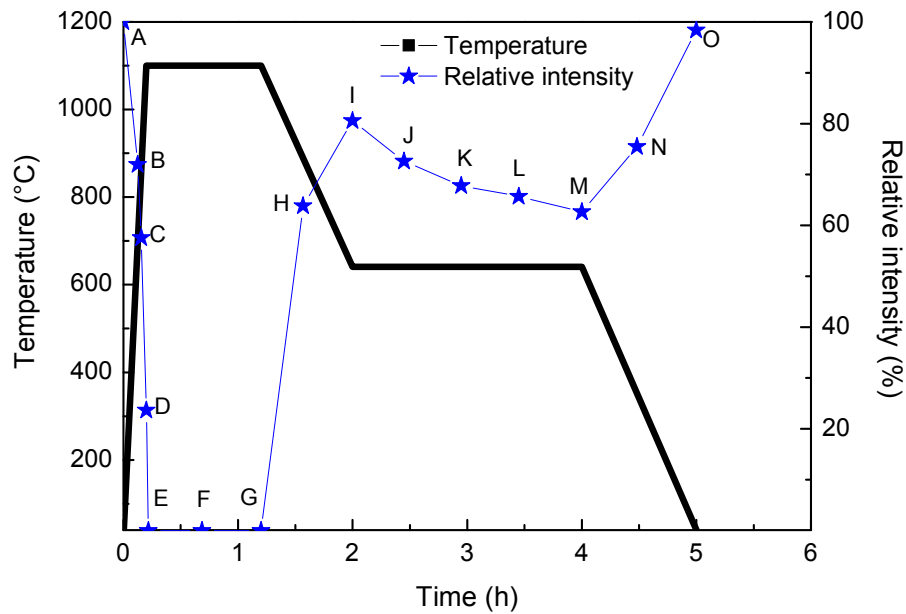


Fig. 5.4-3. Variation of the relative intensities of TiC_x reflections in Ti-22Nb (1500/4) with temperature and time.

The dissolution of TiC_x particles during the second holding time at 641 °C (from Point *I* to Point *M*) is in agreement with the prediction of the pseudo-binary phase diagram of Ti-22Nb-C.

In order to estimate the theoretical time for carbide dissolution at 641 °C, different models are applied based on various assumptions.

Using a diffusion-controlled model, the diffusion of C and Ti atoms leads to the dissolution of TiC_x particles into the matrix. Minkwitz et al. [185] pointed out that in α -Ti as well as in β -Ti, the diffusion coefficient of C atoms is at least three orders of magnitude higher than that of Ti atoms. Besides, the diffusion coefficient of C atoms is also found to be three to four orders of magnitude higher than that of Ti atoms in the TiC_x phase [188-190]. Thus, it is reasonable to assume that the dissolution of TiC_x particles results from the diffusion of C atoms rather than that of Ti atoms.

The diffusion of carbon atoms from the TiC_x particles to the matrix should follow Fick's second law:

$$\frac{\partial c}{\partial t} = D \frac{\partial^2 c}{\partial x^2} \quad (5.4-2)$$

where c is the concentration of carbon, t is time, D is the diffusion coefficient of carbon and x is the position. Because of the small volume fraction and fine scale of carbide relative to the matrix, a 3-dimensional model is used to describe the dissolution behavior of TiC_x particles. For the isotropic dissolution of a spherical TiC_x particle with carbon concentration of c_p and original radius of r_0 into an infinite surrounding matrix with carbon concentration of c_0 , the change in carbon concentration with time can be described as:

$$\frac{\partial c}{\partial t} = \frac{D}{r^2} \frac{\partial}{\partial r} \left(r^2 \frac{\partial c}{\partial r} \right) \quad (5.4-3)$$

where r is the radius of the TiC_x particle at time t . Besides, Eq. 5.4-3 should fulfill the boundary conditions:

$$c(r = r_0, t = 0) = c_0 \quad (5.4-4)$$

$$c(r, t) = c_i \quad (5.4-5)$$

where c_i is the carbon concentration on the boundary of the TiC_x particle at time t . Fig. 5.4-4 presents the schematic profile of the carbon concentration near a TiC_x particle according to the model.

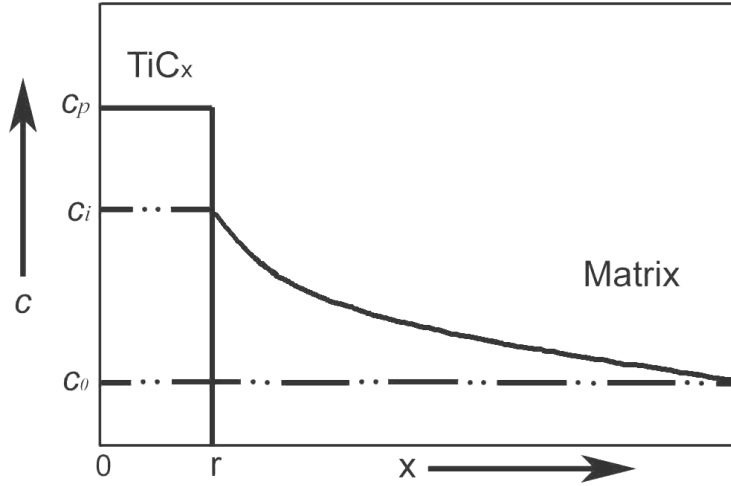


Fig. 5.4-4. Schematic carbon concentration profile near a TiC_x precipitate during diffusion-controlled dissolution

At a constant temperature, the diffusion-controlled dissolution of spherical particles leads to the following expression [191]:

$$\frac{dr}{dt} = -\frac{k}{2} \left(\frac{D}{r} + \sqrt{\frac{D}{\pi t}} \right) \quad (5.4-6)$$

where k is Boltzmann's constant. Due to the complex form of this equation, it is not possible to solve it analytically. As stated by Bjørneklett et al. [192], Eq. 5.4-6 can be simplified as:

$$r^2 = r_0^2 - kDt \quad (5.4-7)$$

Based on Eq. 5.4-7, Cai et al. [193] proposed that for such a 3-dimensional spherical model, the relationship between time, temperature, and residual volume fraction of the spherical particle could be given by:

$$\ln \left(1 - V_r^{\frac{2}{3}} \right) = \ln \left(\frac{\eta}{r_0^2} \right) + \ln D - \frac{Q}{kT} + \ln t \quad (5.4-8)$$

where V_r is the residual volume fraction of the particle at temperature T after dissolving for time t , η is a constant related to the carbon concentrations in the particle (c_p) and the matrix (c_0), and Q is the activation energy. In the present work, the residual volume fraction V_r of the TiC_x particles can be calculated according to the relative intensity of the TiC_x reflections from Point I to Point M , which can be given

as:

$$V_{rx} = \frac{RI_x}{RI_I} \quad (5.4-9)$$

where V_{rx} is the residual volume fraction at Point X ($X=J, K, L$ or M), RI_x and RI_I are the relative intensities of the TiC_x reflections at Point X and Point I , respectively. Since the temperature was always 641 °C during the annealing, Eq. 5.4-8 takes the form:

$$\ln\left(1 - V_r^{\frac{2}{3}}\right) = \ln t + A \quad (5.4-10)$$

where A is a constant.

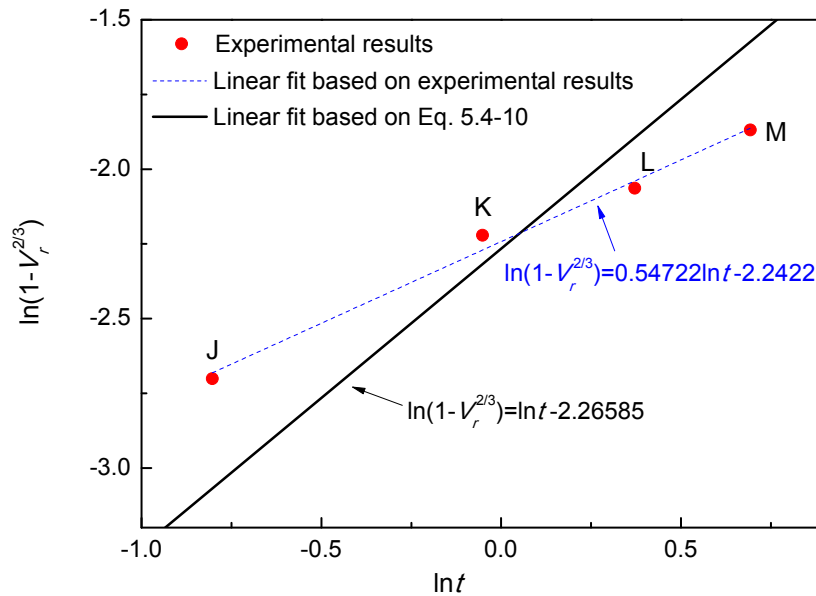


Fig. 5.4-5. The relationship between the residual volume fraction V_r of the TiC_x particles (at Point J , Point K , Point L and Point M) and the diffusion time t . The blue dash line represents a linear fit based on the experimental results, whereas, the black solid line is the linear fit based on Eq. 5.4-10.

Concerning the dissolution process of the TiC_x particles from Point J to Point M , the value of A can be directly obtained from the intercept of the linear fit to Eq. 5.4-10 as presented in Fig. 5.4-5. However, the slope of one predicted by Eq. 5.4-10 is not in good accordance with the experimental data. A linear fit to the experimental points

results in a slope of approximately 0.5 as shown in Fig. 5.4-5. This difference indicates that there are other effects influencing the TiC_x dissolution, besides diffusion of carbon into the matrix.

According to Eq. 5.4-10, when using $A=-2.26585$ the theoretical time for complete dissolution at 641 °C, i.e., V_r is 0, can be calculated as 9.64 h. However, the Ti-22Nb (1500/4+Q) and Ti-22Nb (HIP+Q) samples which were annealed at 641 °C for 120 h still have TiC_x particles as presented in Fig. 4.6-2. Such a difference suggests that the dissolution of TiC_x particles in the Ti-Nb matrix is probably controlled by some other effects than bulk diffusion of carbon away from the dissolving carbide. It is possible to have an interface process which proceeds slower than the diffusion-controlled dissolution. Zhang et al. [180] noticed two to three orders of magnitude longer dissolution time of the TiC_x particles in Ti compared to estimates based on a diffusion-controlled model. The so called uniform atomic detachment, i.e., the debonding of TiC_x into Ti and C atoms, was found to be one possible reason for the slower dissolution rates. Thus, also in the present study the dissolution rate of the TiC_x particles is probably not controlled by the diffusion of carbon atoms, but by the debonding of TiC_x . That is, the uniform atomic detachments of TiC_x might play a significant role in the dissolution of the TiC_x particles.

The HEXRD spectra shown in Fig. 4.5-4 provided the information concerning the evolution of volume fractions of various phases during the whole solution treatment cycle. Whereas, the Debye-Scherrer rings revealed the details about the evolution of lattice parameter, crystallographic relationship and grain size during the whole cycle. Generally speaking, the morphology of the Debye-Scherrer rings depends on grain shape and grain size with respect to beam size and the dimensions of the illuminated volume. A spiky pattern is related to the reflections of relatively few large grains, whereas, a continuous smooth ring reveals a much higher number of and therefore much smaller grains.

At Point *A*, the α -phase shows the same lattice parameter as α -Ti, but the lattice parameter of the β -phase is about 0.03 Å smaller than that of pure β -Ti, because the Nb atoms, which have smaller atomic radius than Ti [194, 195], are mainly enriched in the β -phase owing to the strong β -stabilizing effect of Nb. The lattice parameter of the TiC_x phase is exactly the same as the value obtained from the SAED results shown in Fig. 4.5-2. The change of lattice parameter of the β -phase from Point *A* to Point *G* results from the lattice expansion at high temperatures. The few spots of the β -phase shown in Fig. 4.5-6 indicate that the alloy has completely transformed to coarse β -grains after the annealing at 1100 °C. From Point *G* to Point *I*, more spots of $\beta(110)$ suggests a smaller grain size. The face to face reflections of $-\alpha(002)$ and $\beta(110)$ – presented in Fig. 4.5-6c give evidence that α -phase forms from the β -phase and the new formed α -lamellae obey the crystallographic relationship of $\alpha(0001) // \beta(110)$ in the $\alpha+\beta$ lamellar structures with respect to the parent β -grain. As shown in Fig. 4.5-4 and Fig. 4.5-6d, ω -phase is only found at the end of the whole solution treatment cycle, which might be transformed from the β -phase. Since the ω -phase was not observed in all the as-sintered, as-HIPed and as-quenched samples in the present investigation, it is not further discussed in this work.

5.5 Biocompatibility of MIM Ti-Nb alloy

Compared with Ti-6Al-4V, Ti-Nb alloys exhibit better biocompatibility [1]. The Ti-Nb alloys fabricated by traditional processes, e.g., arc-melting technique, have been extensively investigated via both *in vitro* [51, 196] and *in vivo* [52, 197] tests, and no cytotoxic or allergenic effects have ever been found concerning these alloys. However, albeit the MIM CP-Ti has been found to be highly biocompatible [198], the cytocompatibility of the MIM Ti-Nb alloys has not been examined. Since MIM products usually show a chemical composition close to raw materials, it should not affect cytocompatibility. However, some other features such as surface topography of

the implant material could also have an impact on the biological response [198]. The surface topography influences the rate at which bone is formed next to the surface [199]. Besides, Ti-based implants with rougher surfaces exhibit increased pullout strength *in vivo* [200]. The osteoblast-like cells have been found to be preferable to attach to the CP-Ti with rougher surfaces [201]. Thus, the Ti-22Nb (MIM-BIO) samples in as produced form seem particularly suitable for cell growth, owing to the relatively higher roughness than the CP-Ti (MIM-BIO) and Ti-22Nb (AM-BIO).

In the initial cell adhesion experiments, a slight preference of cell adhesion on materials with higher surface roughness is observed, but very few great disparities between different samples are found as illustrated in Fig. 4.7-2. However, the cell spreading has been significantly improved by the MIM process (see Fig. 4.7-3), which probably results from the higher roughness of the CP-Ti (MIM-BIO) and Ti-22Nb (MIM-BIO) samples than that of the Ti-22Nb (AM-BIO) alloy. Cell adhesion is poor on the Ti-22Nb (AM-BIO) samples, however, it is found to be preferable around pores on the rough surfaces of the CP-Ti (MIM-BIO) and Ti-22Nb (MIM-BIO) samples rather than the smooth regions of the surfaces. After incubation for 40 min, the HUCPV cells on all the samples appear flat and multilayered, which is a sign of direct surface adhesion. The proliferation assays show an increasing MTT absorbance of cells with longer incubation time, which also indicates the non-cytotoxic nature of the various samples.

Therefore, it is concluded that the MIM process improves the cytocompatibility of the Ti-22Nb alloy, and the Ti-22Nb (MIM-BIO) samples appear to be ideally suited to favor bone cell adhesion when used in an as-MIM surface condition.

6. Conclusions

In the present work, a series of Ti-Nb alloys with high strength, low Young's modulus and high biocompatibility have been successfully fabricated via the MIM process. The shape of the MIM CP-Ti and Ti-Nb samples has been well preserved from the green state to the as-sintered state.

This work aims at the understanding of the sintering behavior of MIM Ti-Nb binary alloys, the influence of sintering parameters and Nb content on microstructure and mechanical properties of MIM Ti-Nb binary alloys, the carbide precipitation and the biocompatibility of MIM Ti-Nb binary alloys. The results and analyses obtained from these investigations lead to the following conclusions:

- 1) Owing to the different diffusion properties of Ti and Nb powders, the sintering process of the MIM Ti-Nb alloys fabricated by blended powders consists of three main steps – Ti-diffusion step, Ti-Nb-diffusion step and Matrix-diffusion step. At low temperatures, mainly the diffusion between Ti particles contributes to the pore elimination. With increasing temperature, the diffusion between Ti and Nb powders becomes observable, leading to apparent homogenization and further densification. At the Matrix-diffusion step, the homogenization has finished, and the final densification is only dependent on the diffusion of the Ti-Nb matrix. High sintering temperature and long time may be favorable, so as to minimize the porosity of final products.
- 2) With increasing sintering temperatures and sintering time, the MIM CP-Ti and Ti-Nb samples exhibit lower porosity. Among all the sintering procedures tested, only the sintering parameters – 1500 °C/4 h – are found to be effective to produce CP-Ti and Ti-Nb samples with porosity below or at least around 5 %.

- 3) The Young's modulus of MIM CP-Ti and Ti-Nb samples decreased with decreasing sintering temperature and time. The model, which assumes that the porous material consists of a void phase (with zero Young's modulus) and a solid matrix or skeleton phase, is only in accordance with the Young's modulus of samples sintered at 1500 °C for 4 h, but it predicts too high values for the other sintering conditions. If the heterogeneous structure of as-sintered samples with arbitrary pore shapes is taken into account, a satisfactory prediction for the as-sintered Ti-Nb samples, especially the ones with high porosity, is possible. Therefore, besides the porosity, the pore shape and distribution might also have a significant influence on determining Young's modulus of MIM Ti-Nb samples.

- 4) The increase of Nb content leads to a higher amount of β -phase and higher porosity in the CP-Ti (1500/4) and Ti-Nb (1500/4) samples, mainly resulting from the strong β -stabilizing effect and the low diffusion coefficient of Nb, respectively.

- 5) The Nb content, porosity and amount of titanium carbides are the main factors to influence the mechanical properties of the CP-Ti (1500/4) and Ti-Nb (1500/4) samples. The higher Nb content and higher porosity result in a lower Young's modulus. The increase of strength with increasing Nb content correlated not only with the higher Nb content, but also the higher amount of carbide precipitates. Such a combined effect over-compensates the negative influence of porosity on the strength in the as-sintered Ti-Nb alloys. The low ductility of the MIM Ti-16Nb and Ti-22Nb samples is mainly attributed to the carbide precipitates as revealed by the fractography.

- 6) The ductility of both Ti-22Nb (1500/4) and Ti-22Nb (HIP) samples has been successfully enhanced removing carbides through annealing and quenching. Consequently, by suitable heat treatment procedures the carbide precipitation can

be controlled and the elongation of the MIM Ti-Nb alloys can be significantly improved. Albeit a significant reduced tensile strength is observed in the as-quenched samples, they still show enough strength for implant applications.

- 7) The increased precipitation of titanium carbides in the MIM Ti-Nb samples is attributed to the decrease of carbon solubility in the matrix with increasing Nb content which was in accordance with thermodynamic calculations using the CALPHAD method. HEXRD measurements have confirmed the rightness of the calculated pseudo-binary phase diagrams. The dissolution of titanium carbide in the MIM Ti-Nb samples was probably not controlled by the diffusion of carbon atoms, but the debonding of TiC_x at the carbide matrix interface.
- 8) From the biological point of view, the MIM Ti-Nb samples exhibit better or at least comparable biocompatibility than the MIM CP-Ti and arc-melted Ti-Nb samples, which have been known to be highly biocompatible. The MIM Ti-Nb samples seem to be preferable for cell spreading, probably owing to the higher surface roughness. Thus, MIM technique is promising to produce Ti alloys, e.g. Ti-Nb alloys, for implant application.

In summary, the results presented in this study demonstrate the feasibility to fabricate biocompatible MIM Ti-Nb parts with sound mechanical properties. As a consequence, the application of MIM Ti-Nb alloys as biomedical materials should be taken into consideration by scientists and doctors.

Appendix 1 – Abbreviations of various samples

Materials	Sample name	Processings		Classification
		Sinter processing	Final processing	
CP-Ti (MIM)	CP-Ti (1300/4)	1300 °C for 4 h		As-sintered
	CP-Ti (1400/2)	1400 °C for 2 h		As-sintered
	CP-Ti (1400/4)	1400 °C for 4 h		As-sintered
	CP-Ti (1500/2)	1500 °C for 2 h		As-sintered
	CP-Ti (1500/4)	1500 °C for 4 h		As-sintered
	CP-Ti (HIP)	1500 °C for 4 h	HIP	As-HIPed
	CP-Ti (MIM-BIO)	1500 °C for 4 h		BIO-sample
Ti-10Nb (MIM)	Ti-10Nb (1300/4)	1300 °C for 4 h		As-sintered
	Ti-10Nb (1400/2)	1400 °C for 2 h		As-sintered
	Ti-10Nb (1400/4)	1400 °C for 4 h		As-sintered
	Ti-10Nb (1500/2)	1500 °C for 2 h		As-sintered
	Ti-10Nb (1500/4)	1500 °C for 4 h		As-sintered
	Ti-10Nb (HIP)	1500 °C for 4 h	HIP	As-HIPed
Ti-16Nb (MIM)	Ti-16Nb (700/0.03)	700 °C for 2 min		Pre-sintered
	Ti-16Nb (1100/4)	1100 °C for 4 h		Pre-sintered
	Ti-16Nb (1300/4)	1300 °C for 4 h		As-sintered
	Ti-16Nb (1400/2)	1400 °C for 2 h		As-sintered
	Ti-16Nb (1400/4)	1400 °C for 4 h		As-sintered
	Ti-16Nb (1500/2)	1500 °C for 2 h		As-sintered
	Ti-16Nb (1500/4)	1500 °C for 4 h		As-sintered
	Ti-16Nb (HIP)	1500 °C for 4 h	HIP	As-HIPed
Ti-22Nb (MIM)	Ti-22Nb (1300/4)	1300 °C for 4 h		As-sintered
	Ti-22Nb (1400/2)	1400 °C for 2 h		As-sintered
	Ti-22Nb (1400/4)	1400 °C for 4 h		As-sintered
	Ti-22Nb (1500/2)	1500 °C for 2 h		As-sintered
	Ti-22Nb (1500/4)	1500 °C for 4 h		As-sintered
	Ti-22Nb (HIP)	1500 °C for 4 h	HIP	As-HIPed
	Ti-22Nb (1500/4+Q)	1500 °C for 4 h	Quenching from 641 °C	As-quenched
	Ti-22Nb (HIP+Q)	1500 °C for 4 h	HIP + quenching from 641 °C	As-quenched
Ti-22Nb (Argon arc-melted)	Ti-22Nb (MIM-BIO)	1500 °C for 4 h		BIO-sample
	Ti-22Nb (AM-BIO)	1500 °C for 4 h		BIO-sample

Appendix 2 – Properties of different samples

Sample name	Young's modulus by RUS (GPa)	Porosity (%)
CP-Ti (1300/4)	104.8	3.07
CP-Ti (1400/2)	104.9	2.98
CP-Ti (1400/4)	107.7	2.22
CP-Ti (1500/2)	108.3	2.17
CP-Ti (1500/4)	114.6	1.60
CP-Ti (HIP)	116.0	0
Ti-10Nb (1300/4)	84.2	5.61
Ti-10Nb (1400/2)	84.9	5.25
Ti-10Nb (1400/4)	86.5	4.13
Ti-10Nb (1500/2)	86.7	3.95
Ti-10Nb (1500/4)	92.2	3.57
Ti-10Nb (HIP)	95.1	0
Ti-16Nb (1300/4)	74.0	8.02
Ti-16Nb (1400/2)	74.7	7.68
Ti-16Nb (1400/4)	76.0	6.19
Ti-16Nb (1500/2)	76.7	6.14
Ti-16Nb (1500/4)	82.2	5.16
Ti-16Nb (HIP)	88.2	0
Ti-22Nb (1300/4)	67.8	9.17
Ti-22Nb (1400/2)	68.0	8.75
Ti-22Nb (1400/4)	70.1	7.02
Ti-22Nb (1500/2)	70.9	6.87
Ti-22Nb (1500/4)	75.0	5.79
Ti-22Nb (HIP)	82.8	0

References

- [1] Long M, Rack HJ. Titanium alloys in total joint replacement - materials science perspective. *Biomaterials* 1998;19:1621.
- [2] Geetha M, A. K. Singh, Asokamani R, A. K. Gogia. Ti based biomaterials, the ultimate choice for orthopaedic implants - A review. *Progress in Materials Science* 2009;54:397.
- [3] Niinomi M, Nakai M, Hieda J. Development of new metallic alloys for biomedical applications. *Acta Biomaterialia* 2012;8:3888.
- [4] Semlitsch M. Titanium alloys for hip joint replacements. *Clinical Materials* 1987;2:1.
- [5] Ebel T, Ferri OM, Limberg W, Oehring M, Pyczak F, Schimansky F-P. Metal injection moulding of titanium and titanium-aluminides. *Key Engineering Materials* 2012;520:153.
- [6] German RM. *Powder Injection Molding*. New York: Metal Powder Industries Federation, 1990.
- [7] German RM. Titanium powder injection moulding: A review of the current status of materials, processing, properties and applications. *Powder Injection Moulding International* 2009;3:21.
- [8] German RM. Status of metal powder injection molding of titanium. *International Journal of Powder Metallurgy* 2010;46:11.
- [9] Ebel T. Titanium and titanium alloy for medical applications: opportunities and challenges. *Powder Injection Moulding International* 2008;2:21.
- [10] Whittaker D. Developments in the powder injection moulding of titanium. *Powder Injection Moulding International* 2007;1:27.
- [11] Whittaker D. MIM at Euro PM2011: Biomedical applications for metal injection moulding. *Powder Injection Moulding International* 2011;5:50.
- [12] J. A. Sago, M. W. Broadley, Eckert JK. Metal injection molding of alloys for implantable medical devices. *International Journal of Powder Metallurgy* 2012;48:41.
- [13] Fores FH. Advances in titanium metal injection molding. *Powder Metallurgy and Metal Ceramics* 2007;45:303.
- [14] ASTM. *Standard Specification for Metal Injection Molded Unalloyed Titanium Components for Surgical Implant Applications*. ASTM F2989-13. United States: ASTM International, 2013.
- [15] Ebel T. Titanium MIM at Euro PM 2012: Commercial considerations, materials, processing and applications. *Powder Injection Moulding International* 2012;6:29.
- [16] Sidambe AT, Figueroa IA, Hamilton HGC, Todd I. Metal injection moulding of CP-Ti components for biomedical applications. *Journal of Materials Processing Technology* 2012;212:1591.
- [17] Itoh Y, Miura H, Uematsu T, Sato K, Niinomi M, Ozawa T. The commercial potential of MIM titanium alloy. *Metal Powder Report* 2009;64:17.
- [18] A. T. Sidambe, I. A. Figueroa, H. Hamilton, Todd I. Metal injection moulding of Ti-64 components using a water soluble binder. *Powder Injection Moulding*

International 2010;4:56.

- [19] Ferri OM, Ebel T, Bormann R. Influence of surface quality and porosity on fatigue behaviour of Ti-6Al-4V components processed by MIM. *Materials Science and Engineering: A* 2010;527:1800.
- [20] G. C. Obasi, O. M. Ferri, T. Ebel, Bormann R. Influence of processing parameters on mechanical properties of Ti-6Al-4V alloy fabricated by MIM. *Materials Science and Engineering: A* 2010;527:3929.
- [21] Matsuno H, Yokoyama A, Watari F, Uo M, Kawasaki T. Biocompatibility and osteogenesis of refractory metal implants, titanium, hafnium, niobium, tantalum and rhenium. *Biomaterials* 2001;22:1253.
- [22] Wei Q, Wang L, Fu Y, Qin J, Lu W, Zhang D. Influence of oxygen content on microstructure and mechanical properties of Ti-Nb-Ta-Zr alloy. *Materials & Design* 2011;32:2934.
- [23] Sumner DR, Turner TM, Igloria R, Urban RM, Galante JO. Functional adaptation and ingrowth of bone vary as a function of hip implant stiffness. *Journal of Biomechanics* 1998;31:909.
- [24] Huiskes R, Weinans H, Van Rietbergen B. The relationship between stress shielding and bone resorption around total hip stems and the effects of flexible materials. *Clinical orthopaedics and related research* 1992;274:124.
- [25] Hon Y-H, Wang J-Y, Pan Y-N. Composition / Phase structure and properties of titanium-niobium alloys. *Materials Transactions* 2003;44:2384.
- [26] Niinomi M. Recent metallic materials for biomedical applications. *Metallurgical and Materials Transactions A* 2002;33A:477.
- [27] Wang KK, Gustavson LJ, Dumbleton JH. Microstructure and properties of a new beta titanium alloy, Ti-12Mo-6Zr-2Fe, developed for surgical implants. *Medical applications of titanium and its alloys*. West Conshohocken, PA: ASTM STP 1272, ASTM International, 1996. p. 76.
- [28] Mareci D, Chelariu R, Gordin D-M, Ungureanu G, Gloriant T. Comparative corrosion study of Ti-Ta alloys for dental applications. *Acta Biomaterialia* 2009;5:3625.
- [29] Zhou YL, Niinomi M, Akahori T. Dynamic Young's modulus and mechanical properties of Ti-Hf alloys. *Materials Transactions* 2004;45:1549.
- [30] Elias LM, Schneider SG, Schneider S, Silva HM, Malvisi F. Microstructural and mechanical characterization of biomedical Ti-Nb-Zr(-Ta) alloys. *Materials Science and Engineering: A* 2006;432:108.
- [31] Tane M, Nakano T, Kuramoto S, Hara M, Niinomi M, Takesue N, Yano T, Nakajima H. Low Young's modulus in Ti-Nb-Ta-Zr-O alloys: Cold working and oxygen effects. *Acta Materialia* 2011;59:6975.
- [32] Martins DQ, Osório WR, Souza MEP, Caram R, Garcia A. Effects of Zr content on microstructure and corrosion resistance of Ti-30Nb-Zr casting alloys for biomedical applications. *Electrochimica Acta* 2008;53:2809.
- [33] Taddei EB, Henriques VAR, Silva CRM, Cairo CAA. Production of new titanium alloy for orthopedic implants. *Materials Science and Engineering: C* 2004;24:683.

- [34] Housley KL. The History of Titanium. Hartford, CT: Metal Management Aerospace, Inc., 2007.
- [35] Lütjering G, Williams JC. Titanium. Berlin: Springer-Verlag Berlin Heidelberg, 2003.
- [36] Leyens C, Peters M. Titanium and Titanium alloys. Cologne: WILEY-VCH Verlag GmbH & Co. KGaA, Weinheim, 2003.
- [37] Zitter H, Plenk H. The electrochemical behavior of metallic implant materials as an indicator of their biocompatibility. *Journal of Biomedical Materials Research* 1987;21:881.
- [38] Assad M, Lemieux N, Rivard CH, Yahia LH. Comparative in vitro biocompatibility of nickel-titanium, pure nickel, pure titanium, and stainless steel: genotoxicity and atomic absorption evaluation. *Bio-Medical Materials and Engineering* 1999;9:1.
- [39] Bertrand E, Gloriant T, Gordin DM, Vasilescu E, Drob P, Vasilescu C, Drob SI. Synthesis and characterisation of a new superelastic Ti-25Ta-25Nb biomedical alloy. *J. Mech. Behav. Biomed. Mater.* 2010;3:559.
- [40] Williams DF. Implants in dental and maxillofacial surgery. *Biomaterials* 1981;2:133.
- [41] Laing P. Clinical experience with prosthetic materials; historical perspectives, current problems and future directions. *ASTM-STP* 1979;684:199.
- [42] Niinomi M. Mechanical properties of biomedical titanium alloys. *Materials Science and Engineering: A* 1998;243:231.
- [43] Sidambe AT, Choong WL, Hamilton HGC, Todd I. Correlation of metal injection moulded Ti6Al4V yield strength with resonance frequency (PCRT) measurements. *Materials Science and Engineering: A* 2013;568:220.
- [44] Niinomi M. Recent research and development in titanium alloys for biomedical applications and healthcare goods. *Science and Technology of Advanced Materials* 2003;4:445.
- [45] Abdel-Hady M, Hinoshita K, Morinaga M. General approach to phase stability and elastic properties of beta-type Ti-alloys using electronic parameters. *Scripta Materialia* 2006;55:477.
- [46] Banerjee R, Nag S, Fraser HL. A novel combinatorial approach to the development of beta titanium alloys for orthopaedic implants. *Materials Science and Engineering: C* 2005;25:282.
- [47] He G, Hagiwara M. Ti alloy design strategy for biomedical applications. *Materials Science and Engineering: C* 2006;26:14.
- [48] Kuroda D, Niinomi M, Morinaga M, Kato Y, Yashiro T. Design and mechanical properties of new beta type titanium alloys for implant materials. *Materials Science and Engineering: A* 1998;243:244.
- [49] Ramarolahy A, Castany P, Prima F, Laheurte P, Péron I, Gloriant T. Microstructure and mechanical behavior of superelastic Ti-24Nb-0.5O and Ti-24Nb-0.5N biomedical alloys. *Journal of the Mechanical Behavior of Biomedical Materials* 2012;9:83.

- [50]Murray J. The Nb-Ti (Niobium-Titanium) system. *Bulletin of Alloy Phase Diagrams* 1981;2:55.
- [51]Donato TAG, de Almeida LH, Nogueira RA, Niemeyer TC, Grandini CR, Caram R, Schneider SG, Santos Jr AR. Cytotoxicity study of some Ti alloys used as biomaterial. *Materials Science and Engineering: C* 2009;29:1365.
- [52]Miura K, Yamada N, Hanada S, Jung T-K, Itoi E. The bone tissue compatibility of a new Ti-Nb-Sn alloy with a low Young's modulus. *Acta Biomaterialia* 2011;7:2320.
- [53]Hanada S, Ozaki T, Takahashi E, Watanabe S, Yoshimi K, Abumiya T. Composition dependence of Young's modulus in beta titanium binary alloys. In: Chandra T, Torralba JM, Sakai T, editors. *Thermec'2003, Pts 1-5*, vol. 426-4. 2003. p.3103.
- [54]Xu LJ, Chen YY, Liu ZG, Kong FT. The microstructure and properties of Ti-Mo-Nb alloys for biomedical application. *Journal of Alloys and Compounds* 2008;453:320.
- [55]Zhang LC, Klemm D, Eckert J, Hao YL, Sercombe TB. Manufacture by selective laser melting and mechanical behavior of a biomedical Ti-24Nb-4Zr-8Sn alloy. *Scripta Materialia* 2011;65:21.
- [56]Watanabe I, Wataha JC, Lockwood PE, Shimizu H, Cai Z, Okabe T. Cytotoxicity of commercial and novel binary titanium alloys with and without a surface-reaction layer. *Journal of Oral Rehabilitation* 2004;31:185.
- [57]Abdel-Hady Gepreel M, Niinomi M. Biocompatibility of Ti-alloys for long-term implantation. *Journal of the Mechanical Behavior of Biomedical Materials* 2013;20:407.
- [58]Uzumaki ET, Lambert CS, Santos Jr AR, Zavaglia CAC. Surface properties and cell behaviour of diamond-like carbon coatings produced by plasma immersion. *Thin Solid Films* 2006;515:293.
- [59]Cremasco A, Messias AD, Esposito AR, Duek EAdR, Caram R. Effects of alloying elements on the cytotoxic response of titanium alloys. *Materials Science and Engineering: C* 2011;31:833.
- [60]Lu JX, Flautre B, Anselme K, Hardouin P, Gallur A, Descamps M, Thierry B. Role of interconnections in porous bioceramics on bone recolonization in vitro and in vivo. *Journal of Materials Science: Materials in Medicine* 1999;10:111.
- [61]Alvarez K, Nakajima H. *Metallic Scaffolds for Bone Regeneration*. *Materials* 2009;2:790.
- [62]Deligianni DD, Katsala N, Ladas S, Sotiropoulou D, Amedee J, Missirlis YF. Effect of surface roughness of the titanium alloy Ti-6Al-4V on human bone marrow cell response and on protein adsorption. *Biomaterials* 2001;22:1241.
- [63]German RM, Bose A. *Injection molding of metals and ceramics*. Princeton, New Jersey: Metal Powder Industries Federation, 1997.
- [64]Thian ES, Loh NH, Khor KA, Tor SB. Effects of debinding parameters on powder injection molded Ti-6Al-4V/HA composite parts. *Advanced Powder Technology* 2001;12:361.
- [65]Loh NH, Tor SB, Khor KA. Production of metal matrix composite part by powder

- injection molding. *Journal of Materials Processing Technology* 2001;108:398.
- [66]Liu ZY, Loh NH, Tor SB, Khor KA, Murakoshi Y, Maeda R. Binder system for micropowder injection molding. *Materials Letters* 2001;48:31.
- [67]Bilovol VV, Kowalski L, Duszczyk J, Katgerman L. The effect of constitutive description of PIM feedstock viscosity in numerical analysis of the powder injection moulding process. *Journal of Materials Processing Technology* 2006;178:194.
- [68]Liu ZY, Loh NH, Tor SB, Khor KA. Characterization of powder injection molding feedstock. *Materials Characterization* 2002;49:313.
- [69]Huang B, Liang S, Qu X. The rheology of metal injection molding. *Journal of Materials Processing Technology* 2003;137:132.
- [70]Li Y, Li L, Khalil KA. Effect of powder loading on metal injection molding stainless steels. *Journal of Materials Processing Technology* 2007;183:432.
- [71]Edirisinghe MJ, Evans JRG. Review: Fabrication of engineering ceramics by injection moulding. I. Materials selection. *International Journal of High Technology Ceramics* 1986;2:1.
- [72]Edirisinghe MJ, Evans JRG. Properties of ceramic injection moulding formulations. *Journal of Materials Science* 1987;22:269.
- [73]Li Y, Jiang F, Zhao L, Huang B. Critical thickness in binder removal process for injection molded compacts. *Materials Science and Engineering: A* 2003;362:292.
- [74]Zhang J-G, Edirisinghe MJ, Evans JR. A catalogue of ceramic injection moulding defects and their causes. *Industrial Ceramics* 1989;9:72.
- [75]Pan J, Le H, Kucherenko S, Yeomans JA. A model for the sintering of spherical particles of different sizes by solid state diffusion. *Acta Materialia* 1998;46:4671.
- [76]Walker RF. Mechanism of Material Transport During Sintering. *Journal of the American Ceramic Society* 1955;38:187.
- [77]Herring C. Diffusional viscosity of a polycrystalline solid. *Journal of Applied Physics* 1950;21:437.
- [78]Herring C. Effect of change of scale on sintering phenomena. *Journal of Applied Physics* 1950;21:301.
- [79]German RM, Lathrop JF. Simulation of spherical powder sintering by surface diffusion. *Journal of Materials Science* 1978;13:921.
- [80]German RM, Munir ZA. Surface Area Reduction During Isothermal Sintering. *Journal of the American Ceramic Society* 1976;59:379.
- [81]German RM. *Sintering Theory and Practice*. New York: John Wiley & Sons, 1996.
- [82]Hsueh CH, Evans AG, Coble RL. Micostructure development during final intermediate stage sintering. 1. Pore gran-boundary separation. *Acta Metallurgica* 1982;30:1269.
- [83]Vityaz PA, Nasybulin AK. Homogenization in Sintering and Its Influence on Mechanical Properties of Fe-Cr-C and Fe-Ni-C Steels. *Powder Metallurgy* 1985;28:166.
- [84]Bolzoni L, Esteban PG, Ruiz-Navas EM, Gordo E. Mechanical behaviour of pressed and sintered titanium alloys obtained from prealloyed and blended elemental

- powders. *Journal of the Mechanical Behavior of Biomedical Materials* 2012;14:29.
- [85] Tardiff G. Sintering behavior of submicron tungsten-thoria powder blends. *International journal of powder metallurgy* 1969;5:29.
- [86] Brand K, Schatt W. Solid State Sintering of Heterogeneous Systems With Unlimited Mutual Solubility of Components. *Neue Hutte(Germany)* 1991;36:321.
- [87] Levin L, Stern A, Dirnfeld S. Homogenisation during sintering in a system with limited solubility of components. *Z. Metallkunde* 1980;71:621.
- [88] Heckel R, Lanam R, Tanzilli R. Techniques for the study of homogenization in compacts of blended powders *Advanced experimental techniques in powder metallurgy: based on a symposium: Drexel Univ., Philadelphia, 1970. p.139.*
- [89] Smith DW, Hehemann RF. Kinetics of alloy formation in sintered tungsten-rhenium powder compacts *Trans. Met. Soc. AIME* 1966;236:506.
- [90] Wei W, Liu Y, Zhou K, Huang B. Effect of Fe addition on sintering behaviour of titanium powder. *Powder Metallurgy* 2003;46:246.
- [91] Wei W, Liu Y, Tang H, Chen L, Zhou K. Sintering behavior and microstructure evolution of blended elemental Ti-Fe alloys. *Rare metal materials and engineering* 2004;33:1143.
- [92] Spears MA, Evans AG. Microstructure development during final intermediate stage sintering - 2. Grain and pore coarsening. *Acta Metallurgica* 1982;30:1281.
- [93] Markworth AJ. On the volume-diffusion-controlled final-stage densification of a porous solid. *Scripta Metallurgica* 1972;6:957.
- [94] Coble R. Sintering crystalline solids. I. Intermediate and final state diffusion models. *Journal of Applied Physics* 1961;32:787.
- [95] Arzt E, Ashby MF, Easterling KE. Practical applications of hot isostatic Pressing diagrams: Four case studies. *Metallurgical Transactions A* 1983;14:211.
- [96] Govindarajan RM, Aravas N. Deformation processing of metal powders: Part II-Hot isostatic pressing. *International Journal of Mechanical Sciences* 1994;36:359.
- [97] Atkinson HV, Davies S. Fundamental aspects of hot isostatic pressing: An overview. *Metallurgical and Materials Transactions A* 2000;31:2981.
- [98] Sago JA, Broadley MW, Eckert JK. Metal injection molding of alloys for implantable medical devices. *International Journal of Powder Metallurgy* 2012;48:41.
- [99] Williams B. Powder injection moulding in the medical and dental sectors. *Powder Injection Moulding International* 2007;1:12.
- [100] Ebel T. Titanium and titanium alloys for medical applications: opportunities and challenges. *Powder Injection Moulding International* 2008;2:21.
- [101] Sidambe AT, Figueroa IA, Hamilton H, Todd I. Metal injection moulding of Ti-64 components using a water soluble binder. *Powder Injection Moulding International* 2010;4:56.
- [102] Baril E, Lefebvre L, Thomas Y. Interstitial elements in titanium powder metallurgy: sources and control. *Powder Metallurgy* 2011;54:183.
- [103] Ma FC, Lu WJ, Qin JN, Zhang D. Strengthening mechanisms of carbon element in in situ TiC/Ti-1100 composites. *Journal of Materials Science* 2006;41:5395.

- [104] Choe H, Abkowitz S, Abkowitz SM, Dunand DC. Mechanical properties of Ti-W alloys reinforced with TiC particles. *Materials Science and Engineering: A* 2008;485:703.
- [105] Chen ZQ, Hu D, Loretto MH, Wu X. Effect of carbon additions on microstructure and mechanical properties of Ti-15-3. *Materials Science and Technology* 2004;20:343.
- [106] Li YG, Blenkinsop PA, Loretto MH, Rugg D, Voice W. Effect of carbon and oxygen on microstructure and mechanical properties of Ti-25V-15Cr-2Al (wt.%) alloys. *Acta Materialia* 1999;47:2889.
- [107] Kim Y-J, Chung H, Kang S-JL. Processing and mechanical properties of Ti-6Al-4V/TiC in situ composite fabricated by gas-solid reaction. *Materials Science and Engineering: A* 2002;333:343.
- [108] Yanbin L, Yong L, Huiping T, Bin W, Bin L. Fabrication and mechanical properties of in situ TiC/Ti metal matrix composites. *Journal of Alloys and Compounds* 2011;509:3592.
- [109] Obasi GC, Ferri OM, Ebel T, Bormann R. Influence of processing parameters on mechanical properties of Ti-6Al-4V alloy fabricated by MIM. *Materials Science and Engineering: A* 2010;527:3929.
- [110] Bidaux J-E, Closuit C, Rodriguez-Arbaizar M, Zufferey D, Carreno-Morelli E. Metal injection moulding of low modulus Ti-Nb alloys for biomedical applications. *European Powder Metallurgy Conference*, vol. 1. Basel, Switzerland, 2012. p.199.
- [111] Santos DR, Pereira MS, Cairo CAA, Graça MLA, Henriques VAR. Isochronal sintering of the blended elemental Ti-35Nb alloy. *Materials Science and Engineering: A* 2008;472:193.
- [112] Ebel T, Blawert C, Willumeit R, Luthringer BJC, Ferri OM, Feyerabend F. Ti-6Al-4V-0.5B—A Modified Alloy for Implants Produced by Metal Injection Molding. *Advanced Engineering Materials* 2011;13:B440.
- [113] Wennerberg A, Ohlsson R, Rosén BG, Andersson B. Characterizing three-dimensional topography of engineering and biomaterial surfaces by confocal laser scanning and stylus techniques. *Medical Engineering & Physics* 1996;18:548.
- [114] Yan L, Hui L, Xianda S, Jianghong L, Shuili Y. Confocal laser scanning microscope analysis of organic-inorganic microporous membranes. *Desalination* 2007;217:203.
- [115] Luthringer BJC, Ali F, Akaichi H, Feyerabend F, Ebel T, Willumeit R. Production, characterisation, and cytocompatibility of porous titanium-based particulate scaffolds. *Journal of Materials Science: Materials in Medicine* 2013;24:2337.
- [116] Sarugaser R, Lickorish D, Baksh D, Hosseini MM, Davies JE. Human Umbilical Cord Perivascular (HUCPV) Cells: A Source of Mesenchymal Progenitors. *STEM CELLS* 2005;23:220.
- [117] Sekimoto W, Tsuda H, Mori S. Effects of Chromium and Nitrogen Contents on Microstructural Changes in TiC Particles in (alpha plus beta)- and beta-Titanium Matrix Composites. *Materials Transactions* 2012;53:1405.

- [118] Konitzer DG, Loretto MH. Microstructural assessment of Ti6Al4V-TiC metal-matrix composite. *Acta Metallurgica* 1989;37:397.
- [119] Taruta S, Kawashima K, Kitajima K, Takusagawa N, Okada K, Otsuka N. Influence of Zirconia Addition on the Sintering Behavior of Bimodal Size Distributed Alumina Powder Mixtures. *Journal of the Ceramic Society of Japan* 1994;102:139.
- [120] Leber S, Hehemann RF. Homogenization kinetics of a sintered columbium alloy. *Trans. AIME* 1964;230:100.
- [121] Coble RL. Initial Sintering of Alumina and Hematite. *Journal of the American Ceramic Society* 1958;41:55.
- [122] Zhang H, German RM. Homogenization and microstructure effects on the properties of injection molded Fe-2Ni steel. *Metallurgical Transactions A* 1992;23:377.
- [123] Narasimhan KS. Sintering of powder mixtures and the growth of ferrous powder metallurgy. *Materials Chemistry and Physics* 2001;67:56.
- [124] Georgeault D, Dran J, Cizeron G. Sintering behaviour of (Ni+Cr) powder systems and elaboration of the corresponding alloys. *Annales des Chimie, France* 1983;8:203.
- [125] Sauer C. Sintering and Homogenization Behavior of Copper-Based Alloys. *Metallwissenschaft und technik* 1991;45:1123.
- [126] Shaw N, Honeycombe R. Some Factors Influencing the Sintering Behaviour of Austenitic Stainless Steel Powders. *Powder Metallurgy* 1977;20:191.
- [127] Kaysser W, Huppmann W, Petzow G. Analysis of dimensional changes during sintering of Fe-Cu. *Powder Metallurgy* 1980;23:86.
- [128] Klinger L, Rabkin E. Sintering of spherical particles of two immiscible phases controlled by surface and interphase boundary diffusion. *Acta Materialia* 2013;61:2607.
- [129] Lame O, Bellet D, Michiel MD, Bouvard D. In situ microtomography investigation of metal powder compacts during sintering. *Nuclear Instruments and Methods in Physics Research Section B: Beam Interactions with Materials and Atoms* 2003;200:287.
- [130] Coble RL. Effects of Particle-Size Distribution in Initial-Stage Sintering. *Journal of the American Ceramic Society* 1973;56:461.
- [131] German RM. Prediction of sintered density for bimodal powder mixtures. *Metallurgical Transactions A* 1992;23:1455.
- [132] Lange FF. Sinterability of Agglomerated Powders. *Journal of the American Ceramic Society* 1984;67:83.
- [133] Messing GL, Onoda GY. Inhomogeneity-Packing Density Relations in Binary hwders. *Journal of the American Ceramic Society* 1978;61:1.
- [134] Petersson A, Ågren J. Sintering shrinkage of WC-Co materials with different compositions. *International Journal of Refractory Metals and Hard Materials* 2005;23:258.
- [135] German RM. *Powder metallurgy science*. Princeton: Metal powder industries federation, 1984.

- [136] Hidnert P. Thermal expansion of titanium. Research Paper RP1520 J. Res. Nat. Bur. of Std 1943;30:101.
- [137] Edwards JW, Speiser R, Johnston HL. High Temperature Structure and Thermal Expansion of Some Metals as Determined by X-Ray Diffraction Data. I. Platinum, Tantalum, Niobium, and Molybdenum. Journal of Applied Physics 1951;22:424.
- [138] Liu Y, Pan T, Zhang L, Yu D, Ge Y. Kinetic modeling of diffusion mobilities in bcc Ti-Nb alloys. Journal of Alloys and Compounds 2009;476:429.
- [139] Askill J, Gibbs GB. Tracer Diffusion in β -Titanium. physica status solidi (b) 1965;11:557.
- [140] Gibbs GB, Graham D, Tomlin DH. Diffusion in titanium and titanium-niobium alloys. Philos. Mag. 1963;8:1269.
- [141] Pontau AE, Lazarus D. Diffusion of titanium and niobium in bcc Ti-Nb alloys. Physical Review B 1979;19:4027.
- [142] Neumann G, Tuijn C. Chapter 4 Self-Diffusion and Impurity Diffusion in Group IV Metals. Pergamon Materials Series, vol. Volume 14. Pergamon, 2008. p.149.
- [143] Rao WR, Jatkar AD, Tendolka.Gs. Contribution of grain boundary diffusion during intermediate stage sintering of copper. International Journal of Powder Metallurgy 1970;6:65.
- [144] Thümmel F, Thomma W. The sintering process. Metallurgical Reviews 1967;12:69.
- [145] Pabst W, Gregorová E, Tichá G. Elasticity of porous ceramics—A critical study of modulus–porosity relations. Journal of the European Ceramic Society 2006;26:1085.
- [146] Coble RL, Kingery WD. Effect of Porosity on Physical Properties of Sintered Alumina. Journal of the American Ceramic Society 1956;39:377.
- [147] Ke TS. Experimental evidence of the viscous behavior of grain boundaries in metals. Physical Review 1947;71:533.
- [148] Buch A, Goldschmidt S. Influence of porosity on elastic moduli of sintered materials. Materials Science and Engineering 1970;5:111.
- [149] Lambert P, Ankem S, Wyatt Z, Ferlin KM, Fisher J. Finite element analysis and cellular studies on advanced, controlled porous structures with subsurface continuity in bio-implantable titanium alloys. Journal of Biomedical Materials Research Part A 2014;102:225.
- [150] Gabriel SB, Nunes CA, Soares GdA. Production, Microstructural Characterization and Mechanical Properties of As-Cast Ti-10Mo-xNb Alloys. Artificial Organs 2008;32:299.
- [151] O. M. Ferri, T. Ebel, Bormann R. Influence of surface quality and porosity on fatigue behaviour of Ti-6Al-4V components processed by MIM. Materials Science and Engineering: A 2010;527:1800.
- [152] Zhang Y, Liu H, Jin Z. Thermodynamic assessment of the Nb-Ti system. Calphad 2001;25:305.

- [153] Raabe D, Sander B, Friák M, Ma D, Neugebauer J. Theory-guided bottom-up design of β -titanium alloys as biomaterials based on first principles calculations: Theory and experiments. *Acta Materialia* 2007;55:4475.
- [154] Zhao J, Notis MR. Phase transformation kinetics and the assessment of equilibrium and metastable states
Journal of Phase Equilibria 1993;14:303.
- [155] Xu L-j, Xiao S-l, Tian J, Chen Y-y, Huang Y-d. Microstructure and dry wear properties of Ti-Nb alloys for dental prostheses. *Transactions of Nonferrous Metals Society of China* 2009;19, Supplement 3:s639.
- [156] Ozaki T, Matsumoto H, Watanabe S, Hanada S. Beta Ti alloys with low Young's modulus. *Materials Transactions* 2004;45:2776.
- [157] He G, Eckert J, Dai QL, Sui ML, Löser W, Hagiwara M, Ma E. Nanostructured Ti-based multi-component alloys with potential for biomedical applications. *Biomaterials* 2003;24:5115.
- [158] Bourcier RJ, Koss DA, Smelser RE, Richmond O. The influence of porosity on the deformation and fracture of alloys. *Acta Metall.* 1986;34:2443.
- [159] Wang HW, Qi JQ, Zou CM, Zhu DD, Wei ZJ. High-temperature tensile strengths of in situ synthesized TiC/Ti-alloy composites. *Materials Science and Engineering: A* 2012;545:209.
- [160] Takekawa J, Sakurai N. Effect of the processing conditions on density, strength and microstructure of Ti-12 Mo alloy fabricated by PIM process. *Journal of the Japan Society of Powder and Powder Metallurgy(Japan)* 1999;46:877.
- [161] da Silva AAM, dos Santos JF, Strohaecker TR. Microstructural and mechanical characterisation of a Ti6Al4V/TiC/10p composite processed by the BE-CHIP method. *Composites Science and Technology* 2005;65:1749.
- [162] Frisk K. A revised thermodynamic description of the Ti-C system. *Calphad* 2003;27:367.
- [163] Martins DQ, Souza MEP, Souza SA, Andrade DC, Freire CMA, Caram R. Solute segregation and its influence on the microstructure and electrochemical behavior of Ti-Nb-Zr alloys. *Journal of Alloys and Compounds* 2009;478:111.
- [164] Souza SA, Manicardi RB, Ferrandini PL, Afonso CRM, Ramirez AJ, Caram R. Effect of the addition of Ta on microstructure and properties of Ti-Nb alloys. *Journal of Alloys and Compounds* 2010;504:330.
- [165] Kim HY, Ikehara Y, Kim JI, Hosoda H, Miyazaki S. Martensitic transformation, shape memory effect and superelasticity of Ti-Nb binary alloys. *Acta Materialia* 2006;54:2419.
- [166] Ahmed T, Rack HJ. Martensitic transformations in Ti-(16–26 at%) Nb alloys. *Journal of Materials Science* 1996;31:4267.
- [167] Josephine Prabha A, Raju S, Jeyaganesh B, Rai AK, Behera M, Vijayalakshmi M, Paneerselvam G, Johnson I. Thermodynamics of $\alpha'' \rightarrow \beta$ phase transformation and heat capacity measurements in Ti - 15 at% Nb alloy. *Physica B: Condensed Matter* 2011;406:4200.

- [168] Hao YL, Yang R, Niinomi M, Kuroda D, Zhou YL, Fukunaga K, Suzuki A. Young's modulus and mechanical properties of Ti-29Nb-13Ta-4.6Zr in relation to α " martensite. *Metallurgical and Materials Transactions A* 2002;33:3137.
- [169] Hao YL, Yang R, Niinomi M, Kuroda D, Zhou YL, Fukunaga K, Suzuki A. Aging response of the Young's modulus and mechanical properties of Ti-29Nb-13Ta-4.6Zr for biomedical applications. *Metallurgical and Materials Transactions A* 2003;34:1007.
- [170] Elmay W, Prima F, Gloriant T, Bolle B, Zhong Y, Patoor E, Laheurte P. Effects of thermomechanical process on the microstructure and mechanical properties of a fully martensitic titanium-based biomedical alloy. *Journal of the Mechanical Behavior of Biomedical Materials* 2013;18:47.
- [171] Kar A, Raja KS, Misra M. Electrodeposition of hydroxyapatite onto nanotubular TiO₂ for implant applications. *Surface and Coatings Technology* 2006;201:3723.
- [172] Currey J. Differences in the tensile strength of bone of different histological types. *Journal of anatomy* 1959;93:87.
- [173] Aksoy M, Yilmaz O, Korkut MH. The effect of strong carbide-forming elements on the adhesive wear resistance of ferritic stainless steel. *Wear* 2001;249:639.
- [174] Aksoy M, Kuzucu V, Korkut MH. The influence of strong carbide-forming elements and homogenization on the wear resistance of ferritic stainless steel. *Wear* 1997;211:265.
- [175] Eibler R. New aspects of the energetics of ordered Ti₂C and Ti₂N. *Journal of Physics: Condensed Matter* 2007;19:22.
- [176] Ramqvist L, Hamrin K, Johansson G, Gelius U, Nordling C. VC, NbC and TaC with varying carbon content studied by ESCA. *Journal of Physics and Chemistry of Solids* 1970;31:2669.
- [177] Singh DJ, Klein BM. Electronic structure, lattice stability, and superconductivity of CrC. *Physical Review B* 1992;46:14969.
- [178] Jhi S-H, Louie SG, Cohen ML, Ihm J. Vacancy Hardening and Softening in Transition Metal Carbides and Nitrides. *Physical Review Letters* 2001;86:3348.
- [179] Pickett WE, Klein BM, Zeller R. Electronic structure of the carbon vacancy in NbC. *Physical Review B* 1986;34:2517.
- [180] Zhang SZ, Li MM, Yang R. Mechanism and kinetics of carbide dissolution in near α Ti-5.6Al-4.8Sn-2Zr-1Mo-0.35Si-0.7Nd titanium alloy. *Materials Characterization* 2011;62:1151.
- [181] De Barros MI, Rats D, Vandenbulcke L, Farges G. Influence of internal diffusion barriers on carbon diffusion in pure titanium and Ti-6Al-4V during diamond deposition. *Diamond and Related Materials* 1999;8:1022.
- [182] Chen B-Y, Hwang K-S. Sintered Ti-Fe alloys with in situ synthesized TiC dispersoids. *Materials Science and Engineering: A* 2012;541:88.
- [183] Lee B-J. Thermodynamic assessment of the Fe-Nb-Ti-C-N system. *Metallurgical and Materials Transactions A* 2001;32A:2423.

- [184] Zhao D, Chang K, Ebel T, Qian M, Willumeit R, Yan M, Pyczak F. Microstructure and mechanical behavior of metal injection molded Ti-Nb binary alloys as biomedical material. *Journal of the Mechanical Behavior of Biomedical Materials* 2013;28:171.
- [185] Herzig C, Minkwitz C. Diffusion of ^{14}C in single and polycrystalline α -titanium. *Defect and Diffusion Forum*, vol. 143: Trans Tech Publ, 1997. p.61.
- [186] Carlson ON, Schmidt FA, Uz M. Thermotransport of carbon in niobium. *Journal of the Less Common Metals* 1981;79:97.
- [187] Shuleshova O, Holland-Moritz D, Löser W, Voss A, Hartmann H, Hecht U, Witusiewicz VT, Herlach DM, Büchner B. In situ observations of solidification processes in γ -TiAl alloys by synchrotron radiation. *Acta Materialia* 2010;58:2408.
- [188] Koyama K, Hashimoto Y, Omori S. Diffusion of carbon in TiC. *Transactions of the Japan Institute of Metals* 1975;16:211.
- [189] Sarian S. Diffusion of ^{44}Ti in TiC_x . *Journal of Applied Physics* 1969;40:3515.
- [190] Vanloo FJJ, Bastin GF. On the diffusion of carbon in titanium carbide. *Metallurgical Transactions a-Physical Metallurgy and Materials Science* 1989;20:403.
- [191] Whelan M. On the kinetics of precipitate dissolution. *Metal Science* 1969;3:95.
- [192] Bjørneklett BI, Grong Ø, Myhr OR, Kluken AO. Additivity and isokinetic behaviour in relation to particle dissolution. *Acta Materialia* 1998;46:6257.
- [193] Cai D, Zhang W, Liu W, Yao M. Dissolution kinetics of δ phase in Inconel 718 alloy. *The Chinese Journal of Nonferrous Metals* 2006;16:1349.
- [194] Yu Q, Wang Z, Liu X, Wang G. Effect of microcontent Nb in solution on the strength of low carbon steels. *Materials Science and Engineering: A* 2004;379:384.
- [195] Saillard M, Develey G, Beclé C, Moreau JM, Paccard D. The structure of TiZn_{16} . *Acta Crystallographica Section B* 1981;37:224.
- [196] Wang X, Chen Y, Xu L, Liu Z, Woo K-D. Effects of Sn content on the microstructure, mechanical properties and biocompatibility of Ti-Nb-Sn/hydroxyapatite biocomposites synthesized by powder metallurgy. *Materials & Design* 2013;49:511.
- [197] Yu S, Yu Z, Wang G, Han J, Ma X, Dargusch MS. Biocompatibility and osteoconduction of active porous calcium-phosphate films on a novel Ti-3Zr-2Sn-3Mo-25Nb biomedical alloy. *Colloids and Surfaces B: Biointerfaces* 2011;85:103.
- [198] Demangel C, Auzène D, Vayssade M, Duval J-L, Vigneron P, Nagel M-D, Puipe J-C. Cytocompatibility of titanium metal injection molding with various anodic oxidation post-treatments. *Materials Science and Engineering: C* 2012;32:1919.
- [199] Larsson C, Thomsen P, Aronsson BO, Rodahl M, Lausmaa J, Kasemo B, Ericson LE. Bone response to surface-modified titanium implants: studies on the early tissue response to machined and electropolished implants with different oxide thicknesses. *Biomaterials* 1996;17:605.
- [200] Lossdörfer S, Schwartz Z, Wang L, Lohmann CH, Turner JD, Wieland M,

Cochran DL, Boyan BD. Microrough implant surface topographies increase osteogenesis by reducing osteoclast formation and activity. *Journal of Biomedical Materials Research Part A* 2004;70A:361.

[201] Bowers KT, Keller JC, Randolph BA, Wick DG, Michaels CM. Optimization of surface micromorphology for enhanced osteoblast responses in vitro. *The International journal of oral & maxillofacial implants* 1992;7:302.

Acknowledgements

This research was funded by Helmholtz-CSC Fellowship Programme. I would like to express my deep gratitude to my supervisors – Prof. Dr. Florian Pyczak, Prof. Dr. Regine Willumeit and Dr. Thomas Ebel, for providing me the opportunity to study in Helmholtz-Zentrum Geesthacht and giving me the optimum working conditions. Their guidance, patience and encouragement have been a source of inspiration throughout my three years' work as a PhD student. I am also very grateful to Prof. Dr. Bernd Viehweger for being the chairman for my thesis defense and examination.

I would like to thank my collaborators around the world – Prof. Dr. Ma Qian (University of Queensland), Prof. Dr. Yong Liu (Central South University), Dr. Ming Yan (University of Queensland) and Dr. Keke Chang (RWTH Aachen), owing to their selfless assistance and valuable advice on my research.

I am greatly thankful for the technical and scientific support of all colleagues in the groups – Powder technology, Metal Physics and Structural Research on Macromolecules – at Helmholtz-Zentrum Geesthacht.

Last but not least, my family and my friends always stand firmly behind me. Without them, I could hardly accomplish my work. I love them so much.